Adsorption Science & Technology

Adsorption in Air Pollution Control

Lead Guest Editor: Shien Hui
Guest Editors: Liang Wang and Norbert Miskolczi

Adsorption in Air Pollution Control

Adsorption Science & Technology

Adsorption in Air Pollution Control

Lead Guest Editor: Shien Hui
Guest Editors: Liang Wang and Norbert Miskolczi

Contents

Hindawi
Adsorption Science & Technology
Volume 2022, Article ID 9415595, 11 pages
https://doi.org/10.1155/2022/9415595

Research Article

Economic TEHES-Tube Material Evaluation by Absorbability Index under O-S-Dimensions for Minimizing Global Warming and Air Pollution by Exploring Dominance Theory: Green Management Initiative

M. Prabhu,[1] **Sri Yogi Kottala**,[2] **A. Anbazhagan**,[3] **and Anoop Kumar Sahu**[4]

[1]*Department of Business Administration, College of Administration and Economics, Lebanese French University, Erbil, Kurdistan, Iraq*
[2]*SVKM's Narsee Monjee Institute of Management Studies (Jadcherla Campus), Hyderabad, India*
[3]*Department of Management Studies, PSV College of Arts and Science, Puducherry, India*
[4]*Department of Mechanical Engineering, School of Studies in Engineering and Technology, Guru Ghasidas Vishwavidyalaya, Bilaspur, Chhattisgarh, India*

Correspondence should be addressed to M. Prabhu; bordauprabhu@lfu.edu.krd

Received 19 May 2021; Accepted 27 December 2021; Published 31 January 2022

Academic Editor: Shien Hui

It is investigated that the Global Warming and Air Pollution (GWAP) issues are highly prioritized around the world. There is a high magnitude of contaminated hot heat (CHH) from hot fluids such as contaminated water, oils, and mixed oils; toxic oils increase the GWAP ON emission. Such GWAP can be controlled by applying the methods-techniques for optimizing the energy processes, evaluating the high energy absorption material among available materials and technological advancement in energy flow devices, optimizing design of energy systems and low heat emission strategy, etc. It is observed that nowadays, Thermal Energy Heat Exchanger Systems (TEHESs) are utilized in many industries for transferring the energy between two mineral or contaminated liquids, separated by walls. It is found that TEHESs are constructed by tube materials, might be contributed to control the GWAP if TEHESs are fabricated with composite material, and have a high absorbability index. The evaluation of the Energy Absorbability Index (EAI) of TEHES composite tube materials provides the two innovative solutions to TEHES designers such as choose the economic/cost TEHESs and initiate to green management (reducing minimizing the GWAP). On literature survey, a few research documents are found by authors, which focused on mathematical modelling of either O- (objective-) or S- (subjective-) dimensions of composite TEHES tube material evaluation models for computing EAI. It is also probed that those models are simulated by single or nondynamic material evaluation methods. Therefore, it is summarized that there are no still research document pertaining to integrated/mixed mathematical modelling of O-S- (objective-subjective-) dimensions of composite TEHES tube materials with dominance theory for computing EAI of composite TEHES tube materials. Said research gaps are respected as major research defies (help to minimize the GWAP or green management). To fulfil the said research defies, the authors developed and proposed the TEHES-O-S-composite tube material evaluation model by conducting literature and real industrial survey, consisting of seven TEHES-O and four TEHES-S tube material dimensions. The O-dimensions are framed by available O-rating/data, while S-dimension is framed S-rating. The TFNs (triangular fuzzy numbers) are used by a team of experts for assigning the appropriateness ratings vs. four TEHES-S composite tube material dimension, and priority weights are assigned vs. entire TEHES-O-S tube material dimensions. After data modelling of the TEHES-O-S-composite tube material evaluation model, defuzzification is carried out to normalize O-S-data. Later, the authors' implemented integrated optimization technique "crisp VIKOR combined FMF technique" to evaluate the EAI of composite TEHES tube materials. As the reliability of results is an enormous concern, dominance theory is applied by conducting the comparative analysis among evaluated results and delivering the accurate and reliable results. The evaluated beast composite TEHES tube materials based on EAI linked to green management and economic concern of material. The research can be used by TEHES designers to minimize the GWAP across the universe.

1. Introduction and Literature Review

It is seen that Energy Management (EM) always contributed to protect the universe from GWAP. Green management is respected as EM or clean environmental initiative, which focused on high energy resource utilization by many conduits such as energy loss projection by devices, high toxic energy absorption, and eco-friendly technology applications to save energy, reuse of energy, etc. Economic is dealing with cost analysis. TEHESs are found as a sizzling device in the context of EM. It is found that EM contributed to reduce the GWAP around the universe. TEHESs are used to transfer the heat from boiling fluid to gas (vapour), water, air, and other fluids (toxic or nontoxic in nature). During heat transfer in case of toxic hot fluids, the hot heat burns the environmental toxic particles, consequently emphasizing the GWAP. Therefore, to control or decrease GWAP, the TEHESs must be fabricated of well suit composite material and should have the strong EAI, so that heat transfer might occur without losing of CHH towards environment. TEHESs must be framed with the materials, which encompass the best, rich, and high EAI, and can address the green management cum economic aspects. Energy Absorbability (EA) is defined as a measure of the degree to which materials are capable to absorb of heat/energy. EA of TEHES is defined as a capability of alloys or composites or proposed materials to absorb the heat/energy without emission of contaminated or noncontaminated CHH to environment during the circulation of fluids across TEHESs. EAI is defined as a measurement of overall performance of TEHESs against multiple energy protection, green management imitative indicators/measures. It is probed by scientists via empirical surveys as well as recent research documents that high EAI of TEHES materials extremely impact the performance of TEHESs; therefore, said materials aid TEHESs to produce the high energy transition between two separated toxic fluids without losing CHH to environments, indirectly helping to increase the green management and minimize the future GWAP vice versa.

It is investigated that millions of industries are the user of TEHESs. Every day millions of tons of toxic CHH emits from TEHESs, which causes the GWAP. The existed CHH is also mixed with earth, environmental nanoparticles, and burns it to be released to the universe. Therefore, such as daily phenomenon cannot be entirely controlled, however can be minimized. As we universally know, the evaluation of high EAI of composite materials for fabricating the TEHESs plays the significant function in the area of EM. The TEHES tube material evaluation against high EAI requires the O-S (objective-subjective) dimension analysis simultaneously to become the potential device for reducing the GWAP. The dimensions that can be measured is called a set of objective (O) dimensions. The dimensions that are vague in nature and cannot be measured are called a set of subjective (S) dimensions. In the recent research search, the authors found that a few research documents existed, which dealt with mathematical modelling of individual O-ph (objective) or S-ph (subjective) dimension models. Determined models are simulated by single or non-Morden material evaluation methods. Therefore, the authors ascertained that there are no still research document focused on mixed mathematical modelling of O-S- (objective-subjective-) dimension model with an integrated approach with dominance theory in the context of evaluating the EAI of composite TEHES tube material to control and minimize GWAP. To fulfil these research challenges, in the presented research work, the authors focused on right evaluation and selection of high EAI-TEHES tube material from available range of material alternatives, which aids TEHESs to minimize GWAP [1, 2].

In order to establish the O-S- (objective-subjective-) dimension model for assessing EAI of composite TEHES tube materials, the authors conducted the literature survey are revealed here.

The appropriate evaluation of high-EAI TEHES tube materials is a crucial task for the designers and operators [3–5]. Today, it is necessary to measure the EAI of TEHESs, which make TEHESs for attaining the nexus goal effectually and effectively. For the same, it is necessary to be alerted about various alternatives and criteria, satisfying the EAI of TEHES tube materials so that the best material can be used for fabricating the TEHESs. The criteria should analyze the performance of diverse TEHES tube materials vs. EAI and should evaluate fit TEHES tube material under EAI concerns [3]. Today, a large quantity of TEHES tube materials for designing TEHES with diverse properties is available, and hence, it is significant to adopt appropriately among available [6, 7]. The TEHES tube material evaluation under EAI issue is respected as a complicated and time-consuming task, and their selection will grace the several benefits such as help to attain the nexus goal [6, 8]. TEHES tube material evaluation greatly interlinked the EA characteristics as said by [5, 9]. It is articulated that integration of potential technologies, heat absorbability of materials, etc., implicated by the practitioners into conventional working systems and the process of TEHESs, which reinforced the efficacy of conventional engineering systems and processes [8, 10]. Today, material selection under EAI concern is becoming enormous dilemmas entailing the economic, social, and commercial aspects [7, 11].

Christian et al., [12] examined the mechanical, optical, and physical properties of Thermally Modified Timber (TMT) with its impact on high heat flow. Dang et al., [13] constructed a regularized solution of the source energy data prediction by using the interpolation and the truncated Fourier series method. [14] investigated the different effectiveness of heat and mass exchangers by using NTU correlation numerical models. The authors found that the effectiveness of heat and mass exchangers depends upon the evaluation and selection of conductive materials. Loganathan, A. and Ilangkumaran, M. [15] said that heat sink extensive material evaluation criteria must be formed for enhancing the reliability and life of modern heat devices. Thermal management devices are audited to verify the material evaluation model. Reeju P. [16] proposed new physical mechanisms for accurate material property predictions of materials to be used for heat generators. Uttamm and Mrinmoy [17] articulated that the performance and reliability of material's parameters that provide the higher

operational efficiency for heat exchangers are examined by using the MCDM-NBO approach. Many physical dimensions are examined under investigation. [18] conducted the numerical analysis over the design evaluation of solar tower receiver under different parameters. The authors ascertained that material evaluation helps the solar tower receiver generate the high energy. It is determined that an appropriate selection of elevated TEHES tube materials is important for gracing the nexus goal, i.e., Air Pollution to Global Warming Zhengyi and Zheng [19]; Tripathi et al., [20]; Wang and Liu [21]; Aroon [22]; Wang [23], Girish et al., [24]. Systematic TEHES tube material selection processes require integration of optimization techniques and evaluation of life cycle behaviour of materials [11, 25]. Multidimension integral and decision-making models encompass mathematical tools and can be utilized to evaluate and compare distinguish alternatives for supporting decision making under complex alternatives. After conducting a literature review, the authors proposed the TEHES material evaluation O-S dimension based model with the defuzzification-based crisp VIKOR-FMF-dominance theory approach to fulfil aforesaid research defies.

2. Fuzzy Set towards Mathematical Framing of S-Dimensions of TEHES Tube Materials Assessing EAI

The fuzzy set theory was introduced by Zadeh [26] to contract with the problems linking to vagueness and imprecise information. Triangular fuzzy numbers (TFNs) as presented by [27] is used in the presented research work for grasping ratings and weights of O-S dimensions of composite TEHES tube materials. In the last decade, fuzzy logic has been successfully implicated in numerous practical applications. The fuzzy set theory works by way of engrossing numerical entities in engineering applications. Fuzzy sets assist in data handling and can be effectively engaged during system data processing [28]. The decision support model or frameworks are required to solve the issue of inserting fuzzy information into a system. Fuzzy evidently reach towards an acceptable range of solution after integrating series of extended operations. Fuzzy is considered as a mathematical modelling language by the researchers to approximate situations underlying conflicting criteria. The presented work utilized the arithmetic operations of triangular fuzzy numbers based on extension principle [29, 30].

Definition 1 (see Zadeh [26]). Fuzzy number. If a fuzzy set A on the universe R of real numbers satisfies the following conditions, we call it a fuzzy number.

(1) A is a convex fuzzy set

(2) There is only one x_0 that satisfies $f_A(x_0) = 1$

(3) $f_A(x)$ is continuous in an interval

Based on the extension principle, we can derive the arithmetic of fuzzy numbers as shown in ([30], Kaufmann and Gupta; 1991, [29]). Definition triangular fuzzy number: let $\tilde{B} = (a, b, c)$, $a < b < c$, be a fuzzy set on $R = (-\infty, \infty)$. It is called a triangular fuzzy number if its membership function is

$$\mu_{\tilde{B}}(x) = \begin{cases} \dfrac{x-a}{b-a}, \text{if } a \le x \le b, \\ \dfrac{c-x}{c-b}, \text{if } b \le x \le c, \\ 0, \quad \text{otherwise.} \end{cases} \tag{1}$$

Obviously, we can treat the triangular fuzzy number $\tilde{B} = (a, b, c)$ as the trapezoid (a, b, b, c).

$$\tilde{a} \oplus \tilde{b} = (a_1, a_2, a_3) \oplus (b_1, b_2, b_3) = (a_1 + b_1, a_2 + b_2, a_3 + b_3),$$

$$\tilde{a} - \tilde{b} = (a_1, a_2, a_{3\sim}) - (b_1, b_2, b_3) = (a_1 - b_4, a_2 - b_3, a_3 - b_2),$$

$$\begin{aligned} \tilde{a} \otimes \tilde{b} &= (a_1, a_2, a_3) \otimes (b_1, b_2, b_3) = \tilde{a} \otimes \tilde{b} \\ &= (a_1 \times b_1, a_2 \times b_2, a_3 \times b_3), \end{aligned}$$

$$\frac{\tilde{a}}{\tilde{b}} \frac{(a_1, a_2, a_3)}{(b_1, b_2, b_3)} = \left(\frac{a_1}{b_3}, \frac{a_2}{b_2}, \frac{a_3}{b_1}\right). \tag{2}$$

3. Dominance Theory towards Evaluation of EAI of TEHES Tube Materials under O-S-Dimensions

It is probed that each decision pertaining to reduce emission of CHH and contaminated matters fruitfully participate in controlling the GWAP and green management. The decision must be reliable. In worrying about such as matter, (Sahu et al., 2019) introduced the dominance theory. The motivation of authors to explore the dominance theory in the presented research work is to serve the defuzzification-based robust simulation-integrated technique (VIKOR-FMF) in solving the TEHES-O-S tube material evaluation model for assessing EAI of composite TEHES tube materials. The dominance theory instructed the authors to suggest the results with conducting the comparative analysis as the reliability of results is a concern.

Let $E = \{e_1, e_2, \cdots, e_q\}$ be the set of decision-makers in the group decision-making process. $A = \{A_1, A_2, \cdots, A_m\}$ be the set of alternatives, and $C = \{C_1, C_2, \cdots, C_n\}$ be the set of criteria attributes. Then, the TFN-aggregated fuzzy rating of alternatives with respect to each criterion can be defined as

$$\tilde{\tilde{x}}_{ijk} = \left(a_{ij}, b_{ij}, c_{ij}\right), \tag{3}$$

where

$$a_{ij} = \frac{1}{K} \sum_{k=1}^{K} a_{ijk}, \tag{4}$$

Table 1: Developed and proposed TEHES-O-S-composite tube material evaluation model for assessing EAI and controlling the GWAP.

Model	Nature of characteristics	Characteristics	Symbols	Units
Energy Absorbability Index (EAI)	Objective (O-dimensions)	Yield strength on contaminated hot heat transfer	Yschht	N/m^2
		Ultimate tensile strength on contaminated hot heat transfer	Utschht	N/m^2
		Tube material elongation on contaminated hot heat transfer	% Eht	%
		Hardness tendency on contaminated hot heat transfer	Htchht	BHN
		Cost	C	INR/kg
		Corrosion rate reduction on contaminated hot heat transfer	Crrchht	%
		Wear rate on contaminated hot heat transfer	Wrchht	m^3/m
	Subjective (S-dimensions)	Tube material molecular excitement for heat absorbability	Tmmeha	Unit less
		Contaminated hot heat reduction to environment	Chhre	Unit less
		Contaminated hot heat transfer efficiency	Chhte	Unit less
		Contaminated hot heat transfer effectiveness	Chhtes	Unit less

Table 2: TEHES-O-S-tube material dimensions.

Composite TEHES tube material evaluation	TEHES-O-S-ph tube material evaluation dimensions assessing HOI										
	O-ph-data							S-ph-data			
	Yschht	Utschht	% Eht	Htchht	C	Crrchht	Wrchht	Tmmeha	Chhre	Chhte	Chhtes
J4	382	728	48	98	112	0.16	2.75	*F*-variable	*F*-variable	*F*-variable	*F*-variable
JSLAUS	420	790	58	97	210	0.31	2.63	*F*-variable	*F*-variable	*F*-variable	*F*-variable
J204Cu	415	795	55	96	120	0.05	2.5	*F*-variable	*F*-variable	*F*-variable	*F*-variable
409 M	270	455	32	78	184	0.4	4	*F*-variable	*F*-variable	*F*-variable	*F*-variable
J-304	256	610	60	86	89	0.01	2.59	*F*-variable	*F*-variable	*F*-variable	*F*-variable

$$b_{ij} = \frac{1}{K}\sum_{k=1}^{K} b_{ijk}, \tag{5}$$

$$c_{ij} = \frac{1}{K}\sum_{k=1}^{K} c_{ijk}. \tag{6}$$

Then, the aggregated fuzzy weight of each criterion can be defined as

$$\tilde{\tilde{w}}_j = \left(w_{j1}, w_{j2}, w_{j3}\right), \tag{7}$$

where

$$w_{j1} = \frac{1}{K}\sum_{k=1}^{K} w_{kj1}, \tag{8}$$

$$w_{j2} = \frac{1}{K}\sum_{k=1}^{K} w_{kj2}, \tag{9}$$

$$w_{j3} = \frac{1}{K}\sum_{k=1}^{K} w_{kj3}. \tag{10}$$

3.1. Defuzzification. The defuzzification is the technique, which is employed to convert the TFN fuzzy elements into the crisp value for evaluating and comparing the alternatives. [31] described the three main approaches as the max criteria, mean of maximum, and the centre of area.

Table 3: The scale for assigning ratings for O-dimensions and weights for O-S-ph-dimensions.

Linguistic	Rating variables	Weights variables	Rating/weights
Very poor	VP	ML	(0, 0, 3)
Poor	P	M	(0, 3, 5)
Fair	F	MH	(2, 5, 8)
Good	G	H	(5, 7, 10)
Very good	VG	VH	(7, 10, 10)

The center of gravity method to convert the triangular fuzzy set $(A, B; C)$ into the measured or crisp value form [31]:

$$\frac{A + 4B + C}{6}. \tag{11}$$

3.2. VIKOR-Technique-1. VIKOR stands for VIseKriterijumska Optimizacija I Kompromisno Resenje. The technique ranks the alternatives and determines the solution named compromise that is the closest to the ideal. VIKOR as presented by [27], is used in the presented research work for defining the appropriate high EAI of composite TEHES tube material alternatives, which can help for controlling the GWAP. VIKOR considers the expert's preference to review the dimensions of composite TEHES tube materials [32]. The VIKOR was recently developed as a one of multidimension integral and decision making of the complex system, which

Table 4: Fuzzy variable ratings vs. TEHES-S-ph tube material dimensions for assessing EAI.

Composite TEHES tube material evaluation	S-dimensions	Expert 1	Expert 2	Expert 3	Expert 4	Expert 5	Expert 6	Expert 7	Expert 8	Expert 9	Expert 10	Aggregated fuzzy ratings
J4	Tmmeha	G	G	G	G	G	G	G	VP	VP	VP	(2.00, 2.80, 5.80)
	Chhre	VG	VG	VG	VG	VG	VG	VG	VP	VP	VP	(2.80, 5.80, 7.00)
	Chhte	VP	VP	VP	VP	VP	VP	VP	F	F	F	(1.20, 3.00, 6.00)
	Chhtes	VP	VP	VP	VP	VP	VP	VP	G	G	G	(1.90, 4.20, 6.10)
JSLAUS	Tmmeha	F	F	F	F	F	F	F	VG	VG	VG	(3.10, 5.50, 7.60)
	Chhre	VG	VG	VG	VG	VG	VP	VP	VP	VP	VP	(1.90, 3.90, 5.90)
	Chhte	VP	VP	VP	VP	VP	F	F	VP	VP	VP	(1.50, 3.90, 6.30)
	Chhtes	VP	VP	VP	VP	VP	G	G	F	F	F	(2.60, 4.90, 7.70)
J204Cu	Tmmeha	F	F	F	F	F	VG	VG	G	G	G	(3.90, 6.60, 9.00)
	Chhre	G	G	G	G	G	VP	VP	VG	VG	VG	(4.10, 5.80, 7.90)
	Chhte	VG	VG	VG	VG	VG	P	P	VP	VP	VP	(3.50, 5.60, 6.90)
	Chhtes	VP	VP	VP	VP	VP	VP	VP	VP	VP	VP	(0.40, 3.40, 5.60)
409 M	Tmmeha	F	F	F	F	F	F	F	F	F	F	(2.00, 5.00, 8.00)
	Chhre	G	G	G	G	G	G	G	G	G	G	(5.00, 7.00, 10.0)
	Chhte	VG	VG	VG	VG	VG	VG	VG	VG	VG	VG	(7.00, 10.0, 10.0)
	Chhtes	VP	VP	VP	VP	VP	VP	VP	VP	VP	VP	(0.00, 0.00, 3.00)
J-304	Tmmeha	VP	VP	VP	VP	VP	VP	VP	VP	VP	VP	(0.00, 3.00, 5.00)
	Chhre	F	F	F	F	F	F	F	F	F	F	(2.00, 5.00, 8.00)
	Chhte	G	G	G	G	G	G	G	G	G	G	(5.00, 7.00, 10.0)
	Chhtes	VG	VG	VG	VG	VG	VG	VG	VG	VG	VG	(2.00, 2.80, 5.80)

Table 5: Fuzzy weight vs. TEHES-O-S-tube material dimensions for assessing EAI.

O-S-dimensions	Expert 1	Expert 2	Expert 3	Expert 4	Expert 5	Expert 6	Expert 7	Expert 8	Expert 9	Expert 10	Aggregated fuzzy weight
Yschht	ML	M	H	MH	VH	M	MH	VH	ML	H	(2.80, 5.00, 7.20)
Utschht	H	H	MH	H	ML	H	H	ML	H	MH	(3.10, 5.10, 7.70)
% Eht	VH	H	VH	M	VH	H	M	VH	VH	VH	(3.80, 6.00, 7.60)
Htchht	M	M	H	H	H	M	H	H	M	H	(2.50, 4.70, 7.30)
C	ML	ML	ML	M	M	ML	M	M	ML	ML	(1.40, 3.40, 5.70)
Crrchht	H	VH	MH	H	MH	VH	H	MH	H	MH	(2.80, 5.20, 7.70
Wrchht	M	ML	M	M	ML	ML	M	ML	M	M	(0.00, 1.80, 4.20)
Tmmeha	ML	ML	M	M	ML	M	M	ML	ML	ML	(0.00, 1.50, 4.00)
Chhre	VH	MH	H	MH	VH	H	MH	H	MH	ML	(4.20, 6.80, 9.20)
Chhte	ML	M	M	ML	ML	M	ML	M	M	ML	(0.00, 1.80, 4.20)
Chhtes	ML	ML	M	M	ML	M	M	ML	ML	ML	(0.00, 1.50, 4.00)

determines the compromise ranking and the compromise solution under initial weights [33]. The methodology formulates decision-making problem followed by normalization of decision-making information. The techniques construct weighted decision-making matrix via determining of the positive ideal solution and the negative ideal solution of the evaluated stuffs. VIKOR utilized equations (12)–(18) for decision rationalization and evaluation.

The operational rules of the trapezoidal fuzzy numbers $\tilde{a}$ and $\tilde{b}$ are shown as follows Chen et al. (2005):

$$r_{ij} = \frac{x_{ij}}{\sqrt{\sum_{j=1}^{n} x^2 ij}}, i = 1, 2, 3, \cdots\cdots m, \quad j = 1, 2, 3, \cdots\cdots n. \tag{12}$$

For beneficial attributes:

$$\tilde{\tilde{\mathscr{V}}}^{+} = \left[\tilde{\tilde{v}}_{j}^{+}\right]_{1\times n}, \tag{13}$$

$$\tilde{\tilde{\mathscr{V}}}^{-} = \left[\tilde{\tilde{v}}_{j}^{-}\right]_{1\times n}. \tag{14}$$

For nonbeneficial attributes:

$$\begin{aligned} \tilde{\tilde{\mathscr{V}}}^{+} &= \left[\tilde{\tilde{v}}_{j}^{-}\right]_{1\times n}, \\ \tilde{\tilde{\mathscr{V}}}^{-} &= \left[\tilde{\tilde{v}}_{j}^{+}\right]_{1\times n}, \end{aligned} \tag{15}$$

$$\mathscr{S}_i = \sum_{j=1}^{n} \frac{d\left(\tilde{\tilde{v}}_{j}^{+}, \tilde{\tilde{v}}_{ij}\right)}{d\left(\tilde{\tilde{v}}_{j}^{+}, \tilde{\tilde{v}}_{j}^{-}\right)}, \tag{16}$$

$$\mathscr{R}_i = \max_{j}\left[\frac{d\left(\tilde{\tilde{v}}_{j}^{+}, \tilde{\tilde{v}}_{ij}\right)}{d\left(\tilde{\tilde{v}}_{j}^{+}, \tilde{\tilde{v}}_{j}^{-}\right)}\right], \tag{17}$$

$$\mathscr{Q}_i = \nu\frac{(\mathscr{S}_i - \mathscr{S}^*)}{(\mathscr{S}^- - \mathscr{S}^*)} + (1-\nu)\frac{(\mathscr{R}_i - \mathscr{R}^*)}{(\mathscr{R}^- - \mathscr{R}^*)}, \tag{18}$$

where ν is introduced as weight of the strategy of the majority of criteria or the maximum group utility. Rank the alternatives by sorting the values of in ascending order.

3.3. FMF-Technique-2. It is full multiplicative form of *MOORA* [27]. It embodies the maximization as well as minimization of multiplicative utility function, where overall utility of i_{th} alternative is expressed as dimensionless number, and w_i is considered as priority weights:

$$U_i' = \frac{A_i}{B_i}. \tag{19}$$

Here, denotes the product of ben $A_i = \prod_{j=1}^{g} x_{ij}$; $i = 1, 2, \cdots, m$ eficial measures of the i_{th} alternative to be maximized with $g = 1, 2, \cdots, n$ being the number of measures to be maximized and $B_i = \prod_{j=g+1}^{n} x_{ij}$; $i = 1, 2, \cdots, m$ denotes the product of nonbeneficial measures of the i_{th} alternative to be minimized with $n - g$ being the number of measures to be minimized.

4. Case Study

This is an empirical case study of a TEHES production company, located at the north part of India. The manager of said company had received an order from one of the ECM (Electrical Discharge Machine) workshop/lab to design TEHES of such as material, which has high EAI. The material has capability to absorb or extract the heat from exiting toxic hot soap-linseed-kerosene water coolant after finishing each ECM machining operation, so that after cooling, ECM fluid (due to passing through TEHES) can be reused for machining of the next part. Therefore, the manager of the case study company has instructed the designer for designing TEHESs by mapping the EAI of composite TEHES tube materials under O-S dimensions. The developed and proposed TEHES-O-S-tube material evaluation model for assessing an EAI of composite TEHES tube material is shown in Table 1.

Table 6: Computed defuzzified crisp values of TEHES-O-S-tube material dimensions for assessing EAI.

O-S dimensions	Defuzzified priority weights/weight crisp value	Defuzzified appropriateness ratings/rating crisp value				
		J4	JSLAUS	J204Cu	409 M	J-304
Yschht	5.0	0.00	0.00	0.00	0.00	0.00
Utschht	5.2	0.00	0.00	0.00	0.00	0.00
% Eht	5.9	0.00	0.00	0.00	0.00	0.00
Htchht	4.8	0.00	0.00	0.00	0.00	0.00
C	3.5	0.00	0.00	0.00	0.00	0.00
Crrchht	5.2	0.00	0.00	0.00	0.00	0.00
Wrchht	1.9	0.00	0.00	0.00	0.00	0.00
Tmmeha	1.7	3.2	3.9	5.5	0.5	3.2
Chhre	6.8	5.5	3.9	3.3	2.8	5.5
Chhte	1.9	3.2	5.0	5.0	5.0	3.2
Chhtes	1.7	4.1	6.6	7.2	7.2	4.1

Table 7: Computed normalized values of TEHES-O-S-tube material dimensions for assessing EAI.

O-S-dimensions	J4	JSLAUS	J204Cu	409 M	J-304
Yschht	0.480	0.528	0.522	0.339	0.322
Utschht	0.473	0.514	0.517	0.296	0.397
% Eht	0.416	0.503	0.477	0.277	0.520
Htchht	0.480	0.475	0.470	0.382	0.421
C	0.333	0.625	0.357	0.548	0.265
Crrchht	0.300	0.581	0.094	0.750	0.019
Wrchht	0.417	0.399	0.379	0.607	0.393
Tmmeha	0.480	0.475	0.470	0.382	0.480
Chhre	0.333	0.625	0.357	0.548	0.333
Chhte	0.300	0.581	0.094	0.750	0.300
Chhtes	0.417	0.399	0.379	0.607	0.417

Table 8: Computed values of linking TEHES-O-S-tube material dimensions for assessing EAI.

O-S-dimensions	J4	JSLAUS	J204Cu	409 M	J-304
Yschht	0.232	0.000	0.031	0.915	1.000
Utschht	0.197	0.015	$0.00S_i0$	1.000	0.544
% Eht	0.573	0.930	0.823	0.000	1.001
Htchht	0.000	0.051	0.101	1.000	0.601
C	0.190	1.000	0.256	0.785	0.000
Crrchht	0.384	0.769	0.102	1.000	0.000
Wrchht	0.168	0.088	0.000	1.001	0.061
Tmmeha	0.015	0.000	1.000	0.015	0.480
Chhre	0.930	0.823	0.000	0.930	0.333
Chhte	0.051	0.101	1.000	0.051	0.300
Chhtes	0.417	0.399	0.379	0.607	0.417

4.1. The Further Steps Are Depicted Here. Step 1. 100 experts pertaining to different cross-functional departments of said case study company voluntarily participated in that context and provided valuable insights. The Research and Development RND body of company had introduced five alloy composite materials such as J4, JSLAUS, J204Cu, 409 M, and J-304 for assessment and evaluation of EAI under O-S-dimensions depicted in Table 1. The cost and other parameters/characteristics of J4, JSLAUS, J204Cu, 409 M, and J-304 alloy composite material are presented corresponding to alternative composite TEHES tube materials in Table 2.

Step 2. After finalizing the set of TEHES composite tube materials, two members from each depicting departments

Table 9: Computed weight stabilize values of S_i linking TEHES-O-S-tube material dimensions for assessing EAI.

O-S-dimensions	J4	JSLAUS	J204Cu	409 M	J-304
Yschht	0.154	0.000	0.020	0.606	0.662
Utschht	0.132	0.010	0.000	0.668	0.364
% Eht	0.487	0.791	0.700	0.000	0.852
Htchht	0.000	0.036	0.071	0.701	0.422
C	0.063	0.333	0.085	0.262	0.000
Crrchht	0.306	0.612	0.081	0.795	0.000
Wrchht	0.073	0.038	0.000	0.434	0.027
Tmmeha	0.154	0.000	0.020	0.606	0.662
Chhre	0.132	0.010	0.000	0.668	0.364
Chhte	0.487	0.791	0.700	0.000	0.852
Chhtes	0.000	0.036	0.071	0.701	0.422

Table 10: Tabulated cumulative values EAI with rankings.

Energy Absorbability Index (EAI) of alternatives	S_i	R_i	Performance index ($v = 0.5$) VIKOR-technique	Ranking	Performance index FMF-technique	Ranking	Comparative analysis Dominance theory
J4	1.214	0.487	0.0511	1	0.0019	1	1
JSLAUS	1.820	0.791	0.5886	3	0.0013	3	3
J204Cu	0.958	0.700	0.2917	2	0.0015	2	2
409 M	3.465	0.795	0.9228	5	0.0010	5	5
J-304	2.325	0.852	0.7727	4	0.0012	4	4

such as environmental, heat analysis, design, safety, and production of case study company were invited to choose a linguistic variable scale for assigning rating against only S dimensions of TEHES composite tube materials. The expert's panel elected a five-point TFN scale, shown in Table 3 for modelling S-dimensions. The appropriateness ratings or quotation against only O tube material dimensions was proposed vs. five alternative composite TEHES tube materials, i.e., J4, JSLAUS, J204Cu, 409 M, and J-304 by RND, and finally, data of O is mixed with S tube material dimensions to formulate problem, shown in Table 2.

Step 3. Later, the appropriateness subjective ratings against S-tube material dimensions and priority weights against all O-S-ph tube material dimensions, assigned by experts, are revealed in Tables 4 and 5.

Step 4. After evaluating TFN variables from the expert's panel, equations (5) and (9) were used to aggregate the fuzzy set and formulate the TEHES composite tube material evaluation problem, revealed in Tables 4 and 5. Next, the fuzzy data is transformed into crisp value or defuzzified by using equation (11), revealed in Table 6.

Step 5. The normalization of dimensions of TEHES composite tube materials is carried out by using equation (12); the computed values are shown in Table 7. Next, the values of S_i linking decision measures are computed by using equations (14)–(16), revealed in Table 8, and Q_i is determined by using equations (17) and (18), revealed in Table 9.

Step 6. Next, the full multiplicative form, equation (19), was applied on normalized values of Table 7 and multiplied with weights to evaluate the preference orders of TEHES composite tube materials. The results are shown in Table 10.

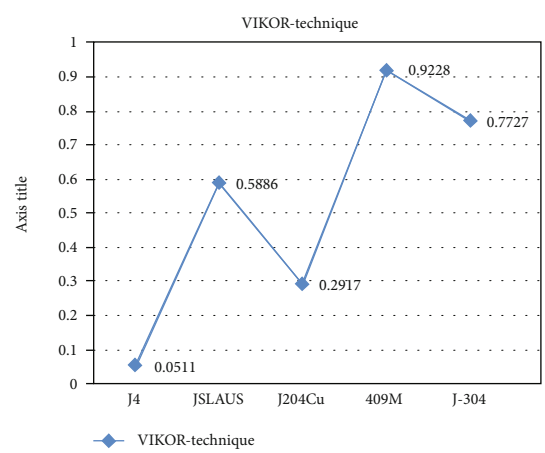

Figure 1: Crisp VIKOR application for evaluating EAI of TEHES tube materials under TEHES-O-S-tube material evaluation dimensions.

Step 7. It is discussed that reliability of results is a major concern in the presented research forum. The J4 TEHES composite tube material had the rich EAI under TEHES-O-S-dimensions to control GWAP, which is computed by application of dominance theory. The results are shown in Table 10.

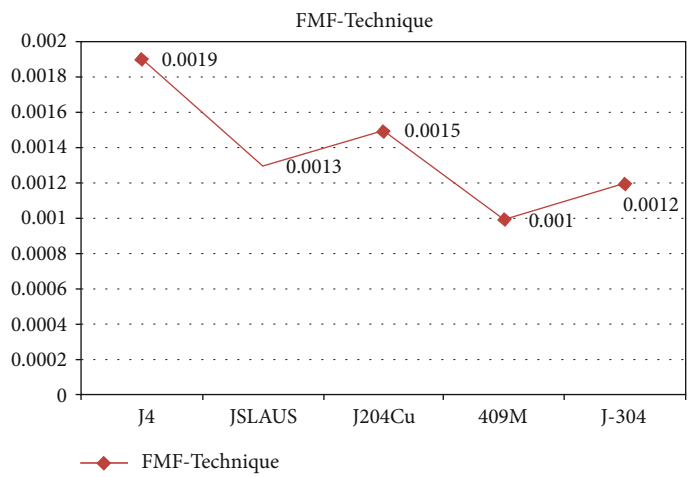

Figure 2: Crisp-FMF application for evaluating EAI of TEHES tube material under TEHES-O-S-tube material evaluation dimensions.

5. Discussions and Result Graphical Representations

The evaluation and selection of high EAI of composite TEHES tube material under umbrella of O-S-tube material dimensions (to reduce CHH loss) are ascertained as the complex and difficult task. As it is investigated by TEHES designers and researchers that preferable alternative selection is not a straightforward process as the acquired results can be sensitive, it is critical and leads to system success or failure. It is determined that unsuccessful elected composite TEHES tube materials not only increase the emission of CHH loss towards environment during toxic fluid circulation across TEHESs but also increase the manufacturing cost and unnecessarily maintenance costs and causes of GWAP.

Nowadays, companies are attempting to design their TEHESs in such a way, where TEHESs can reduce the GWAP by maximizing heat transfers between two toxic fluids with zero CHH emission, rich efficiency (good output), etc. The same can be achieved by engrossing and selecting the high EAI composite TEHES tube material, technologies, means, new products into existing manufacturing systems, said by ([1, 9, 10, 34]. The same is attempted in the presented research work as discussed.

In the presented research work as we discussed, a mixed mathematical modelling of the O-S (objective-subjective-) dimension model with an integrated approach embedded with dominance theory is proposed for evaluating the EAI of composite TEHES tube material to control and minimizing GWAP and green management vice vera. As a part of analysis, in the case study (Section 4), the designer was requested to use J4 from available materials such as JSLAUS, J204Cu, 409 M, and J-304 from green management and economic perspectives to build TEHES for extracting the heat from exiting toxic hot soap-linseed-kerosene water coolant after finishing each ECM operation. The results are tabulated in Table 10, the graphical representation (Figures 1 and 2) depicted the results, and however, dominance technique is applied additional for obtaining accurate results as discussed.

6. Conclusion

The evaluation of high EAI-composite TEHES tube material and then selection under O-S-tube material dimensions (mixed modelling) is a crucial phase. The appropriate high EAI-composite TEHES tube material evaluation and selection under both dimensions (mixed modelling) leads towards the success of TEHES production companies. In the presented research work, the efforts are implicated to develop and propose a TEHES-O-S-tube material evaluation model for assessing EAI and economically electing efficient TEHES tube material from available domains under O-S-ph dimensions. In the presented research work, the same is targeted by the authors by assessing the high EAI of TEHES composite TEHES tube material under TEHES-O-S-tube material dimensions. As discussed, the proposed TEHES-O-S-tube material evaluation model for assessing EAI consisted of five grades of TEHES composite tube materials, i.e., J4, JSLAUS, J204Cu, 409 M, and J-304. The RND department proposed materials to TEHES designer to examine them and assess that which is the best to fabricate TEHES under seven TEHES-O-tube material evaluation dimensions, i.e., Yschht, Utschht, % Eht, Htchht, C, Crrchht, and Wrchht in conjunctive with four TEHES-S-tube material evaluation dimensions, i.e., Tmmeha, Chhre, Chhte, and Chhtes. The solution is found by using integrated crisp-FMF-VIKOR techniques with dominance theory, where Yschht, Utschht, Htchht, Tmmeha, Chhre, Chhte, and Chhtes replicate beneficial dimension and % Eht, C, Crrchht, and Wrchht replicate nonbeneficial dimension. After the technical steps of integrated FMF-VIKOR techniques, it is found that TEHES-tube material J4 is prioritized as the best alternative on the application of crisp VIKOR and the next same alterative is also suggested on the application of crisp FMF. To conformity, the dominance theory is implicated to respond towards significant alternative TEHES-tube material evaluation; therefore, dominance theory also concluded same J4 alternative material. The case study company is advised to choose J4 to fabricate TEHES, has high EAI under mixed modelling (O-S) dimensions, and shall be fine for extracting the heat from exiting toxic

hot soap-linseed-kerosene water coolant after finishing each ECM operation. The research work provided the two innovative solutions to TEHES designers such as choose the economic/cost TEHESs and initiate to green management (reducing minimizing the GWAP). From future perspective, the forthcoming or advanced materials to be tested for fabricating the TEHESs can be investigated under proposed model (O-S) dimensions on replacement of O-S data.

Data Availability

The data used to support the findings of this study are available in Table 10.

Conflicts of Interest

The authors declare that there is no conflict of interest regarding the publication of this manuscript.

Acknowledgments

The paper is prepared by research employment.

References

[1] X. Qin, G. Huang, A. Chakma, X. Nie, and Q. Lin, "A MCDM-based expert system for climate-change impact assessment and adaptation planning - A case study for the Georgia Basin, Canada," *Canada, Expert Systems with Applications*, vol. 34, no. 3, pp. 2164–2179, 2008.

[2] P. Konidari and D. Mavrakis, "A multi-criteria evaluation method for climate change mitigation policy instruments," *Energy Policy*, vol. 35, no. 12, pp. 6235–6257, 2007.

[3] V. P. Darji and R. V. Rao, "Intelligent multi criteria decision making methods for material selection in sugar industry," *Procedia Materials Science*, vol. 5, pp. 2585–2594, 2014.

[4] E. K. Zavadskas, Z. Turskis, and T. Vilutiene, "Multiple criteria analysis of foundation instalment alternatives by applying additive ratio assessment (ARAS) method," *Archives of Civil and Mechanical Engineering*, vol. 10, no. 3, pp. 123–141, 2010.

[5] A. S. Milani, A. Shanian, R. Mandoliat, and J. A. Nemes, "The effect of normalization norms in multiple attribute decision making models: a case study in gear material selection," *Structural and Multidisciplinary Optimization*, vol. 29, no. 4, pp. 312–318, 2005.

[6] L. Anojkumar, M. Ilangkumaran, and V. Sasirekha, "Comparative analysis of MCDM methods for pipe material selection in sugar industry," *Expert Systems with Applications*, vol. 41, pp. 2964–2980, 2014.

[7] E. Zumelzu, C. Cabezas, O. Optitz, E. Quiroz, L. Goyos, and A. Parada, "Microstructural characteristics and corrosion behavior of high chromium cast iron alloys in sugar media," *Protection of Metals*, vol. 39, no. 2, pp. 183–188, 2003.

[8] Z. P. Fan, X. Zhang, F. D. Chen, and Y. Liu, "Extended TODIM method for hybrid multiple attribute decision making problems," *Knowledge-Based Systems*, vol. 42, pp. 40–48, 2013.

[9] M. K. Rathod and H. V. Kanzaria, "A methodological concept for phase change material selection based on multiple criteria decision analysis with and without fuzzy environment," *Material and Design*, vol. 32, no. 6, pp. 3578–3585, 2011.

[10] S. R. Maitya and S. Chakraborty, "Grinding wheel abrasive material selection by using fuzzy AHP and TOPSIS technique," *International Journal of Humanities and Social Science*, vol. 1, no. 3, pp. 135–140, 2013.

[11] C. H. Wang, I. Y. Lu, and C. B. Chen, "Integrating hierarchical balanced scorecard with non-additive fuzzy integral for evaluating high technology firm performance," *International Journal of Production Economics*, vol. 128, no. 1, pp. 413–426, 2010.

[12] R. W. Christian, B. Christian, and O. R. Andreas, "Influence of treatment temperature and duration on selected biological, mechanical, physical and optical properties of thermally modified timber," *Wood Material Science & Engineering*, vol. 2, no. 2, pp. 66–76, 2007.

[13] D. T. Dang, N. D. A. Pham, and T. N. Phan, "Determine the special term of a two-dimensional heat source," *Applicable Analysis*, vol. 88, no. 3, pp. 457–474, 2009.

[14] N. Prakash, H. M. Karan, H. S. Mostafa, M. Z. Syed, and H. L. V. John, "Energy effectiveness of simultaneous heat and mass exchange devices," *Frontiers in Heat and Mass Transfer (FHMT)*, 2010.

[15] A. Loganathan and M. Ilangkumaran, "Decision making methodology for heat sink material selection using a compromise ranking and outranking method under fuzzy environment," *Journal of Advances in Chemistry*, vol. 12, no. 12, pp. 4564–4575, 2016.

[16] P. Reeju, "Overview of high-energy x-ray diffraction microscopy (HEDM) for mesoscale material characterization in three-dimensions," in *Materials Discovery and Design*, pp. 167–201, Springer, Cham, 2018.

[17] R. Uttamm and M. Mrinmoy, "Productivity yielding in shell and tube heat exchanger by MCDM-NBO approach," *Measurement and Control*, vol. 52, no. 3-4, pp. 262–275, 2019.

[18] H. Messaoud, A. Benaoumeur, C. Xavier et al., "Numerical analysis of a solar tower receiver novel design," *Sustainability*, vol. 12, no. 17, p. 6957, 2020.

[19] L. Zhengyi and S. Zheng, "The nelson-seiberg theorem generalized with nonpolynomial superpotentials," *Advances in High Energy Physics*, vol. 2020, Article ID 3701943, 6 pages, 2020.

[20] A. Tripathi, B. Chauhan, A. K. Rao, and R. P. Malik, "Massive spinning relativistic particle: revisited under brst and supervariable approaches," *Advances in High Energy Physics*, vol. 2020, Article ID 1236518, 25 pages, 2020.

[21] Q. Wang and F. H. Liu, "Excitation function of initial temperature of heavy flavor quarkonium emission source in high energy collisions," *Advances in High Energy Physics*, vol. 2020, Article ID 5031494, 31 pages, 2020.

[22] K. B. Aroon, "Quantum spectrum of tachyonic black holes in a brane-anti-brane system," *Advances in High Energy Physics*, vol. 2020, Article ID 6570890, 6 pages, 2020.

[23] Z. Y. Wang, "Mass or energy: on charge of gravity," *Advances in High Energy Physics*, vol. 2020, Article ID 8202609, 8 pages, 2020.

[24] K. C. Girish, K. Najimuddin, and M. Subhendra, "Super gravity model of inflation and explaining icecube hese data via pev dark matter decay," *Advances in High Energy Physics*, vol. 2020, Article ID 2478190, 14 pages, 2020.

[25] A. Guitouni and J. Martel, "Tentative guidelines to help choosing an appropriate MCDA method," *European Journal of Operational Research*, vol. 109, no. 2, pp. 501–521, 1998.

[26] L. A. Zadeh, "Fuzzy sets," *Information and Control*, vol. 8, no. 3, pp. 338–353, 1965.

[27] A. K. Sahu, H. K. Narang, M. S. Rajput, N. K. Sahu, and A. K. Sahu, "Performance modeling and benchmarking of green supply chain management," *Benchmarking: An International Journal*, vol. 25, no. 7, pp. 2248–2271, 2018.

[28] A. K. Sahu, N. K. Sahu, and A. K. Sahu, "Benchmarking CNC machine tool using Hybrid-Fuzzy methodology," *International Journal of Fuzzy System Applications*, vol. 4, no. 2, pp. 28–46, 2015.

[29] K. Tanaka, *An Introduction to Fuzzy Logic for Practical Applications*, Springer-Verlag, New York, NY, 1997.

[30] L. A. Zadeh, "The concept of a linguistic variable and its application to approximate reasoning–I," *Information Sciences*, vol. 8, no. 3, pp. 199–249, 1975.

[31] A. K. Sahu, N. K. Sahu, and A. K. Sahu, "Fuzziness: a mathematical tool," in *Theoretical and Practical Advancements for Fuzzy System Integration*, pp. 1–30, IGI Global, 2017.

[32] P. P. Mohanty and S. S. Mahapatra, "A compromise solution by VIKOR method for ergonomically designed product with optimal set of design characteristics," *Procedia Materials Science*, vol. 6, pp. 633–640, 2014.

[33] M. K. Sayadi, M. Heydari, and K. Shahanaghi, "Extension of VIKOR method for decision making problem with interval numbers," *Applied Mathematical Modelling*, vol. 33, no. 5, pp. 2257–2262, 2009.

[34] E. Thanassoulis, M. Kortelainen, and R. Allen, "Improving envelopment in data envelopment analysis under variable returns to scale," *European Journal of Operational Research*, vol. 218, no. 1, pp. 175–185, 2012.

Hindawi
Adsorption Science & Technology
Volume 2021, Article ID 3206293, 15 pages
https://doi.org/10.1155/2021/3206293

Research Article

Coal Refinery Process Absorbability Index Assessment against Foot Print of Air Pollution by Usage of Robust Optimization Algorithms: A Novel Green Environment Initiative

Hua Xu,[1] **Shuqiang Cheng**,[1] **M. Prabhu**,[2] **and Anoop Kumar Sahu**[3]

[1]*School of Economics and Management, Shaanxi University of Science and Technology, Xi'an Shaanxi 710021, China*
[2]*Assistant Professor, Department of Business Administration, Lebanese French University, 100 MTR Avenue, 44001 Erbil Kurdistan Region, Iraq*
[3]*Faculty, Mechanical Engg, Guru Ghasidas Vishwavidyalaya, Bilaspur, C.G, India*

Correspondence should be addressed to Hua Xu; xuhua0910@sina.cn

Received 1 June 2021; Accepted 8 September 2021; Published 18 November 2021

Academic Editor: Shien Hui

Coals are employed as fiery substance, and every day, millions of ton coal are consumed by coal users around the world. It is investigated that the millions of coal's transportation/logistic till the coal user plants via road route and also inside the coal user plants (known as twice factors) not only enhance the air pollution but also cause the global warming. It is earlier known that coals emit the toxic pollutants and offensive gases such as sulfur dioxide, SO_2; nitrogen oxides, NOX; hydrogen chloride arsenic; carbon monoxide, CO; methane; CH_4; and CO_2 on reacting with environmental O_2 due to said twice factors, i.e., during the transportation from coal refinery spot to entry gate of coal user plants (another spot) and in process logistic/movement inside the coal user plants (loading to conveyor to coal fire tubes "attached with coal crushers"). Therefore, the coal refinery technique/process is found as the best practice to control air pollution under concerns of twice factors. The reliable and trustworthy coal refining technology improves the quality of coal by eradicating or eliminating the coating or layers of toxic particles from coal's surface, which speedily crumble or decompose in reacting with environmental O_2 under twice factors. As results, coal refining technology adds the green supply chain value into proposed twice factors and also save the world from breeding of ills and viruses. It is understood that the best coal refinery technique/process helps to overcome and reduce air pollution by responding discussed twice factors (accepted as research challenge and motivation of research). In the presented research work, the authors developed and proposed a dynamic multidimension Coal Refinery Process Absorbability Index (CRPAI) structure (consisted of coal refinery core dimension and subdimensions correspond to CRPA alternative techniques/processes) appended with Robust Optimization Algorithm (ROA) to be explored for opting the best CRP from available options. But due to inherent ambiguity, vagueness, and inconsistency involve in both dimensions of proposed structure, the assessment of expert's panel is gathered in the terms of linguistic variable "appropriateness ratings" against the subdimensions of CRPAI structure corresponding to preferred CRP options. Next, assigned appropriateness ratings against the subdimensions are substituted by GIVFN. To arrive to core dimensions from subdimensions of CRPAI structure, a GITFN-OWGO (Ordered Weighted Geometric Operator) is investigated and modified as a Ordered Weighted Geometric Average Operator (OWGAO) to be applied for estimating the weights of subdimensions (core novelty of work). Finally, a ROA (consisted of MULTI-MOORA with dominance theory) is applied on the output of OWGAO for opting the viable and best CRP option. The positive effect of the dynamic multidimension CRPAI structure is that it helps the coal refinery companies to assess measure and evaluate the best and feasible coal refinery process under concern of twice factors using expert information. The research can be used to control the air pollution by responding aforesaid twice factors by single practice (the best coal refinery process/technique assessment and evaluation).

1. Introduction and State of Art

The CO_2 is ascertained as the foremost carbon intensive, which is accountable for more than 72% climate altering phenomenon and major source of air pollution and global warming vice versa. Today, coals are employed as burning material across the global coal user plants. The coal is found chemically intricate fuel as it librates flue gases, which might contain such as sulfur dioxide, SO_2; nitrogen oxides, NOX; hydrogen chloride arsenic; carbon monoxide, CO; methane; CH_4; and carbon dioxide, CO_2 [1–10]. Every day, millions of ton coal are fired by coal user plants. It is noticed that coal becomes extremely low contaminated/toxic gas emitter from coal refinery location/spot to entry gate of coal user plants and also throughout the logistic of coal inside the coal user plants if coal refinery is carried with best practices and technique at inception. Therefore, coal refinery is searched as the preeminent practice amongst many green practices to clean the environment and control air pollution. The coal refinery is respected as ecological balancer in the world, which function is to refine the coal to eliminate further air pollution ([6, 11–15]; CURC 2004; [1–5, 7–10, 16, 17]).

Refined coals are the burnable goods, which are produced by application of a coal-upgrading practices-technology, which eliminate the moisture and certain pollutants from surface of coal stone and add the calorific values. Coal refining is precombustion treatments or processes, which changes the characteristics of coal prior to move is to be burned. In India nation, the coal refinery company use, such as dynamic process, is exhibited here: crushing and breaking—crushing and breaking devices are feeder breakers, rotary breakers, hammer mills, and roll crushers. Sizing them—it is sizing the coal under 20 to 45 mm diameters. Storage and stockpiling—coal is stored in silos or stockpiled before and after cleaning. Spherical, cylindrical, conical silos, or stockpiled is used. Density separation—coal is cleaned by separating the lower density organic material from the higher density by falling it from high 7-10 m height to earth. Washing—washing is done by quenching algorithm and passing through flowing water. Coal drying—thermal drying is lastly carried out by using container, drying in open overcast by sun to reduce the moisture content.

In investigating the CRPAI research documents (RDs), the authors found the many RDs in relation to analyzing the coal supplier performance and materializing the coal emission quantities around the coal user plants. So few RDs are found, dealt with mapping CRPAI under core dimension modeling by *certain or quantitative data* (*except* core dimension modeling by *uncertain or qualitative data*). In addition to that, few CRPA index documents are also grasped, dealt with CRPAI, but constrained to consider the core dimension (*except both*: core and subdimension simultaneously) [2–4, 7, 9, 16].

Furthermore, in investigating the RDs against ROAs, the authors determined that most of the Absorbability Index evaluation RDs dealt with the single optimization algorithm (could tackle *certain data* vs. *core dimension only*). The authors were not found still relevant research document, especially dealt with dynamic multidimension CRPAI structure (consisted of coal refinery core dimension and subdimensions correspond to CRPA alternative processes) with ROAs (can tackle *uncertain/qualitative data vs. both*: *core and subdimension only*) to be used for opting the best CRP from available options. Therefore, the aforesaid research gaps motivated the authors to develop and propose a dynamic multidimension CRPAI structure (consisted of coal refinery core dimension and subdimensions) with ROA to opt the best CRP from available options under linguistic information of expert's panel.

To construct a dynamic multidimension CRPAI structure in addressing the qualitative modeling of core and subdimension simultaneously (CRPAI structure) and finding ROAs, the authors conduct a few literature surveys under aforesaid concerns:

1.1. A Literature over Framing the Dynamic Multidimension CRPAI Structure. [18–21], and [22] outlined the nature of the wastes; waste generating industries; waste characterization; health and environmental implications of waste management practices; steps towards planning; design and development of models for effective hazardous waste management; and treatment, approaches, and regulations for disposal of hazardous waste. Evaluation of the entire situation with reference to Indian scenario has been attempted in order that a better cost-effective strategy for waste management be evolved in the future. [23] proposed a decision model based on environmental performance indicators, which supported decision-making in supply chains in presence of environmental considerations. [24] implemented IVFN-TOPSIS (interval-valued fuzzy number-Technique for Order Preference Similar to Ideal Solution) approach in purpose to find out preference orders of manufacturing alternative firms in context of green supply chain management. [25] articulated an innovative, quantitative assessment of pollution avoidance attributable to environmental regulation enforced through integrated licensing, using Ireland's pharmaceutical-manufacturing sector as a case study. [16] argued the current coal consumption in the UK united with ecological impacts of coal mining, coal processing, and coal utilization for power generation. [7] shown impact of coal mining on land, water, health of workers, air, and social impact on surrounding villages and cities have evaluated. In addition to that, environment management plan of coal mining has also enlarged. [9] carried out a coal mining project in northwestern Bangladesh country in order to appraise the impacts of coal mining on the surrounding environment specifically on soil and water. The research of [26] was conducted to seek the miscellaneous paths to preserve the environmental and also put the environment out of fewer emission of carbon dioxide. The countless several conducted state of arts have been depicted as a citation in order that readers could seek the other way to diminish the universal warming issues in planet world ([1, 2, 8, 10, 17, 27–29]; Sahu et al., 2012; Sahu et al., 2013; [7, 30]a, b; [9, 22]).

Kalibatas and Turskis 2008 and [26] have also formed miscellaneous decision support system in context of manufacturing realm. [31] thermally treated the petroleum coke in the range of 1173–1673 K. The changes of the

composition and crystalline structure of petroleum coke were investigated. ([11, 14, 15]; ; [1–10, 13, 16, 17, 24, 30] a, b) worked to reduce air pollution by applying multivariable optimization methods. Venugopal et al. [32] stimulate the need for developing native solutions against the industrial challenges and revealed the importance of coal industry and coal washing process. Dhawan et al. [33] conducted an experiments for investigating the process parameters of catalytic coke pretreatment processes parameters. Sitorus et al. [34] applied a hybrid MCDM method to evaluate the coal mining and mineral processing units and discussed the pathways and future research directions of the proposed MCDM method. Pourabdollah et al. [35] studied the effect of thermal operation parameters against the graphitization of ethane-based catalytic coal. Dhawan et al. [36] investigated the usage of the catalyst K_2CO_3 over raw coal and the use of KCO_3 over the raw coal as well as help to extract the CO_2 gas from raw coal. Shukla et al. [37] studied about the emission level of CO_2 in India from coal. Various advanced methods for capturing CO_2 are highlighted.

1.2. Literature over Framing the ROAs. [38] explored the application of multiobjective optimization on the basis of ratio analysis (MOORA) algorithm to solve different decision-making problems as frequently encountered in the real-time manufacturing environment. Six decision-making problems have been solved to prove the applicability, potentiality, and flexibility of this algorithm while solving various complex decision-making problems in present day manufacturing environment. [39] implemented the MOORA algorithm for solving multiple criteria (objective) optimization problem in milling process. Six decision-making problems which include selection of suitable milling process parameters in different milling processes are considered, and the obtained results almost match with those derived by the previous researchers which prove the applicability, potentiality, and flexibility of this algorithm in manufacturing environment subsequently. Sahu et al. 2012, Sahu et al. 2013, [30] a, b, [9, 22] have conducted research in context of environmental subdimensions, which have been viewed as a case study. Sahu et al. [24] applied a weighted geometric aggregation operator on robot evaluation model to score the industrial value of robots. Bu et al. [40] proposed a GWmZd model consisted of green vendor evaluation parameters and solved it by knowledge-based grey-holistic technique with dominance theory for sustainable vendor evaluation. He et al. [41] proposed an advanced manufacturing machine tool evaluation model under objective information and solved it by grey relational analysis approach with dominance theory.

1.3. Summary of State of Art. As discussed, the authors only highlighted so few relevant literatures with brief description and cited more RDs to shorten research work. After literature survey, the authors consolidated the relevant CRPAI core and subdissensions and framed a dynamic multidimension CRPAI structure (consisted of coal refinery core dimension and subdimensions). In addition to that, the authors found a most significant ROA (MULTI-MOORA) and enable same to opt the best CRP from available options under linguistic information of expert's panel. But searched ROA was able for qualitative modeling of *core dissensions*. By using concept of fuzzy average rule, the authors made ROA able to tackle core and subdissensions simultaneously by introducing modification in the OWG operator (in previous researches, operator was able to act for qualitative modeling of only core level dimension). Moreover, on focusing over the most recent research of Bu et al. [40] and He et al. [41] for obtaining the reliable results, the authors applied the dominance theory for the comparison amongst the CRPAI preferences, provided by ROA.

2. Rationale to Conduct the Research

Coal pollutants mixed into the atmosphere, which disorder the ecosystem, are shown in Figure 1 ([38, 39, 42–47]; Sahu et al., 2012; Sahu et al., 2013; [30] a, b; [9, 22]).

As discussed, twice factors (transportation from coal refinery spot to entry gate of coal user plants (another spot) and in process logistic/movement inside the coal user plants (loading to conveyor to coal fire tubes attached with coal crushers)) push the attention of authors to conduct the research work in the context of CRP. The authors found a preresearch clue to overcome and control the air pollution and global warming vice versa ([25, 48, 49]; Sahu et al., 2012; Sahu et al., 2013; [30] a, b; [22]).

Later, the authors preaudited the RDs of CRPAI and ascertained that there are still no RDs pertaining to CRPAI structure, which can deal with the qualitative modeling of both core and subdimensions. Up next, the authors found that there are a few RDs related to evaluation of CRPAI by executing single optimization algorithms (SOAs) with the OWG operator (operator was able to act for qualitative modeling of only *core level dimension*). The authors claimed that there is no RD yet, which can tackle subdimensions of CRPAI structure under qualitative modeling in application of the OWG operator appended with ROAs ([30, 50–52]c, e).

Therefore, the aforesaid rationale stimulated the authors to develop and propose a dynamic multidimension CRPAI structure (consisted of coal refinery core dimension and subdimensions) with constructing ROAs (MULTI-MOORA with modification of OWG operator by average fuzzy rule) with application of dominance theory (Bu et al., [40] and He et al., [41] for evaluation of the best CRP from available options under the linguistic information of expert's panel. This proposed research work would assist the managers to identify the best CRP practice and technique or to opt viable CRPs amongst preferred CRPs.

3. Rationale to Implement Interval-Valued Fuzzy Number Set (IVFNs) than Other Fuzzy Number Set

In the present context, authors fruitfully implemented IVFN except other fuzzy numbers, as IVFN deals with completely unknown information. In IVFNs, fuzzy membership function values are intended in between 0 and 1, aligned over

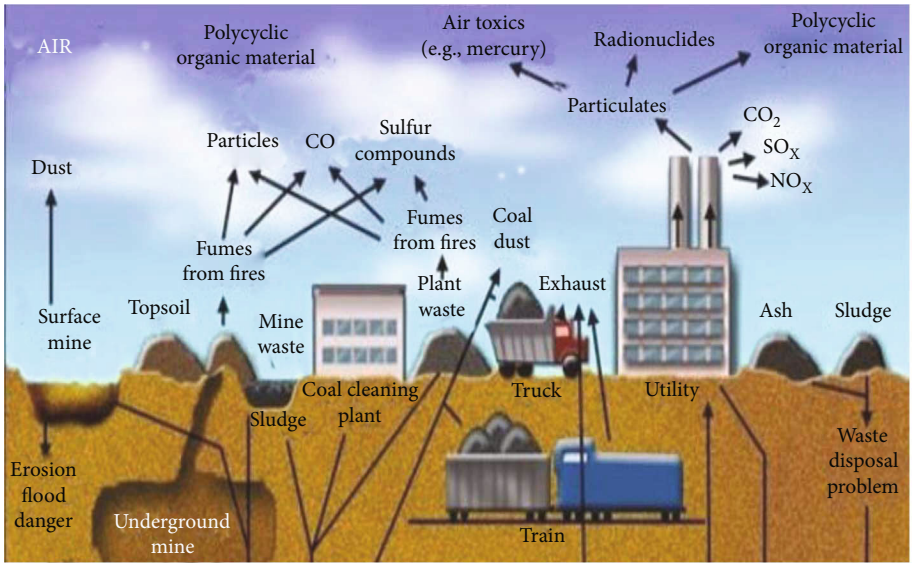

Figure 1: Disordering of ecosystem from coal under twice factors.

two boundaries (upper level (U^U) and lower level (U^L) of membership function. The considered boundaries also undertake the space between (U^u) and (U^L) and can tackle the imprecise, haziness, and vagueness associated with information of expert panel against defined core-subdimensions ([46, 50, 51, 53, 54]; Sahu et al., 2013; [30]), while other fuzzy numbers only deal with the single boundary, which not at all prove to engrave the imprecise, haziness, and vagueness associated with information of expert panel. Consequently, due to aforementioned rationale, IVFN is used for qualitative modeling of defined both dimensions (expert panel's information) for making the verdict [52, 55–59].

4. Fuzzy Preliminaries

Fuzzy sets and fuzzy logic are powerful mathematical tools, employed for modeling uncertain systems or qualitative information. A fuzzy set is an extension of a crisp set. A crisp set only allows full membership or nonmembership, while fuzzy sets allow the partial membership. The theoretical fundaments of fuzzy set theory are overviewed by [52, 55, 57–61]. This section presents the generalized interval-valued trapezoidal fuzzy numbers. In addition, the arithmetic operations and aggregation of the generalized interval-valued trapezoidal fuzzy numbers are as follows.

4.1. The Generalized Trapezoidal Fuzzy Numbers. A fuzzy set $\tilde{A}$ in a universe of discourse X is characterized by a membership function $\mu_{\tilde{A}}(x)$ which associates with each element x in X a real number in the interval [0, 1]. The function value $\mu_{\tilde{A}}(x)$ is termed the grade of membership of x in $\tilde{A}$. A trapezoidal fuzzy number can be defined as $\tilde{A} = (a_1, a_2, a_3, a_4; w_{\tilde{A}})$ as shown in Figure 2, and the membership function $\mu_{\tilde{A}}(x)$: $R \longrightarrow [0, 1]$ is defined as follows:

$$\mu_{\tilde{A}}(x) = \begin{cases} \dfrac{x - a_1}{a_2 - a_1} \times w_{\tilde{A}}, & x \in (a_1, a_2), \\ w_{\tilde{A}}, & x \in (a_2, a_3), \\ \dfrac{x - a_4}{a_3 - a_4} \times w_{\tilde{A}}, & x \in (a_3, a_4), \\ 0, & x \in (-\infty, a_1) \cup (a_4, \infty). \end{cases} \tag{1}$$

Here, $a_1 \le a_2 \le a_3 \le a_4$ and $w_{\tilde{A}} \in (0, 1)$.

Suppose that $\tilde{a} = (a_1, a_2, a_3, a_4; w_{\tilde{A}})$ and $\tilde{b} = (b_1, b_2, b_3, b_4; w_{\tilde{B}})$ are two trapezoidal fuzzy numbers, then the operational rules of the trapezoidal fuzzy numbers $\tilde{a}$ and $\tilde{b}$ are shown as follows:

$$\begin{aligned} \tilde{a} \oplus \tilde{b} &= (a_1, a_2, a_3, a_4; w_{\tilde{A}}) \oplus (b_1, b_2, b_3, b_4; w_{\tilde{B}}) \\ &= (a_1 + b_1, a_2 + b_2, a_3 + b_3, a_4 + b_4; \min\ (w_{\tilde{A}}, w_{\tilde{B}})), \end{aligned}$$

$$\begin{aligned} \tilde{a} - \tilde{b} &= (a_1, a_2, a_3, a_4; w_{\tilde{A}}) - (b_1, b_2, b_3, b_4; w_{\tilde{B}}) \\ &= (a_1 - b_4, a_2 - b_3, a_3 - b_2, a_4 - b_1; \min\ (w_{\tilde{A}}, w_{\tilde{B}})), \end{aligned}$$

$$\begin{aligned} \tilde{a} \otimes \tilde{b} &= (a_1, a_2, a_3, a_4; w_{\tilde{A}}) \otimes (b_1, b_2, b_3, b_4; w_{\tilde{B}}) = \tilde{a} \otimes \tilde{b} \\ &= (a_1 \times b_1, a_2 \times b_2, a_3 \times b_3, a_4 \times b_4; \min\ (w_{\tilde{A}}, w_{\tilde{B}})), \end{aligned}$$

$$\frac{\tilde{a}}{\tilde{b}} = \frac{(a_1, a_2, a_3, a_4; w_{\tilde{A}})}{(b_1, b_2, b_3, b_4; w_{\tilde{B}})} = \left(\frac{a_1}{b_4}, \frac{a_2}{b_3}, \frac{a_3}{b_2}, \frac{a_4}{b_1}; \min\ (w_{\tilde{A}}, w_{\tilde{B}})\right). \tag{2}$$

[27] introduced the center of gravity (COG) measure for generalized trapez4oidal fuzzy numbers. Let there be a generalized trapezoidal fuzzy number $\tilde{A} = (a_1, a_2, a_3, a_4; w_{\tilde{A}})$.

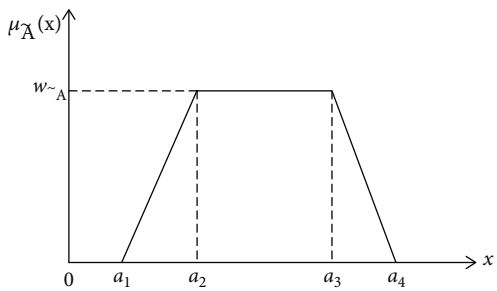

Figure 2: Trapezoidal fuzzy number $\tilde{A}$.

Then, it has its COG point $(x_{\tilde{A}}, y_{\tilde{A}})$, where

$$\begin{cases} y_{\tilde{A}} = \begin{cases} w_{\tilde{A}}\left(\dfrac{a_3 - a_2}{a_4 - a_1} + 2\right), a_1 \neq a_4 \\ \dfrac{w_{\tilde{A}}}{2}, a_1 = a_4 \end{cases} \\ x_{\tilde{A}} = \dfrac{y_{\tilde{A}}(a_2 + a_3) + (a_1 + a_4) + (w_{\tilde{A}} - y_{\tilde{A}})}{2w_{\tilde{A}}} \end{cases}. \quad (3)$$

4.2. The Generalized Interval-Valued Trapezoidal Fuzzy Numbers. Some basic concepts of IVFNs and their arithmetic operations are discussed below:

[57] defined IVFNs and presented their extended operational rules. The trapezoidal IVFN $\tilde{\tilde{A}}$ has been represented by ([46, 50, 51, 53, 55]; Sahu et al., 2013; [30]).

$$\tilde{\tilde{A}} = \left[\tilde{\tilde{A}}^L, \tilde{\tilde{A}}^U\right] = \left[\left(a_1^L, a_2^L, a_3^L, a_4^L; w^L_{\tilde{\tilde{A}}}\right), \left(a_1^U, a_2^U, a_3^U, a_4^U; w^U_{\tilde{\tilde{A}}}\right)\right], \quad (4)$$

Here, $a_1^L \le a_2^L \le a_3^L \le a_4^L, a_1^U \le a_2^U \le a_3^U \le a_4^U, \tilde{\tilde{A}}^L$ denotes the lower IVFN, $\tilde{\tilde{A}}^U$ denotes the upper IVFN, and $\tilde{\tilde{A}}^L \subset \tilde{\tilde{A}}^U$.

Assume that there are two IVFNs $\tilde{\tilde{A}}$ and $\tilde{\tilde{B}}$, where

$$\begin{aligned} \tilde{\tilde{A}} &= \left[\tilde{\tilde{A}}^L, \tilde{\tilde{A}}^U\right] = \left[\left(a_1^L, a_2^L, a_3^L, a_4^L; w^L_{\tilde{\tilde{A}}}\right), \left(a_1^U, a_2^U, a_3^U, a_4^U; w^U_{\tilde{\tilde{A}}}\right)\right], \\ \tilde{\tilde{B}} &= \left[\tilde{\tilde{B}}^L, \tilde{\tilde{B}}^U\right] = \left[\left(b_1^L, b_2^L, b_3^L, b_4^L; w^L_{\tilde{\tilde{B}}}\right), \left(b_1^U, b_2^U, b_3^U, b_4^U; w^U_{\tilde{\tilde{B}}}\right)\right]. \end{aligned} \quad (5)$$

$0 \le w^L_{\tilde{\tilde{A}}} \le w^U_{\tilde{\tilde{A}}} \le 1, \tilde{\tilde{A}}^L \subset \tilde{\tilde{A}}^U, 0 \le w^L_{\tilde{\tilde{B}}} \le w^U_{\tilde{\tilde{B}}} \le 1$, and $\tilde{\tilde{B}}^L \subset \tilde{\tilde{B}}^U$.

From Figure 3, it can be concluded that interval-valued trapezoidal fuzzy number $\tilde{\tilde{A}}$ consists of the lower values of interval-valued trapezoidal fuzzy number $\tilde{\tilde{A}}^L$ and the upper values of interval-valued trapezoidal fuzzy number $\tilde{\tilde{A}}^U$. The operation rules of interval-valued trapezoidal fuzzy numbers as given by [57] have been reproduced below.

Suppose that

$$\tilde{\tilde{A}} = \left[\tilde{\tilde{A}}^L, \tilde{\tilde{A}}^U\right] = \left[\left(a_1^L, a_2^L, a_3^L, a_4^L; w^L_{\tilde{\tilde{A}}}\right), \left(a_1^U, a_2^U, a_3^U, a_4^U; w^U_{\tilde{\tilde{A}}}\right)\right], \quad (6)$$

and

$$\tilde{\tilde{B}} = \left[\tilde{\tilde{B}}^L, \tilde{\tilde{B}}^U\right] = \left[\left(b_1^L, b_2^L, b_3^L, b_4^L; w^L_{\tilde{\tilde{B}}}\right), \left(b_1^U, b_2^U, b_3^U, b_4^U; w^U_{\tilde{\tilde{B}}}\right)\right], \quad (7)$$

are the two interval-valued trapezoidal fuzzy numbers, where

$$\begin{aligned} &0 \le a_1^L \le a_2^L \le a_3^L \le a_4^L \le 1, \\ &0 \le a_1^U \le a_2^U \le a_3^U \le a_4^U \le 1, \\ &0 \le w^L_{\tilde{\tilde{A}}} \le w^U_{\tilde{\tilde{A}}} \le 1, \tilde{\tilde{A}}^L \subset \tilde{\tilde{A}}^U, \\ &0 \le b_1^L \le b_2^L \le b_3^L \le b_4^L \le 1, \\ &0 \le b_1^U \le b_2^U \le b_3^U \le b_4^U \le 1, \\ &0 \le w^L_{\tilde{\tilde{B}}} \le w^U_{\tilde{\tilde{B}}} \le 1, \tilde{\tilde{B}}^L \subset \tilde{\tilde{B}}^U. \end{aligned} \quad (8)$$

(i) The sum of two interval-valued trapezoidal fuzzy numbers $\tilde{\tilde{A}} \oplus \tilde{\tilde{B}}$

$$\begin{aligned} \tilde{\tilde{A}} \oplus \tilde{B} &= \left[\left(a_1^L, a_2^L, a_3^L, a_4^L; w^L_{\tilde{\tilde{A}}}\right), \left(a_1^U, a_2^U, a_3^U, a_4^U; w^U_{\tilde{\tilde{A}}}\right)\right] \\ &\quad \oplus \left[\left(b_1^L, b_2^L, b_3^L, b_4^L; w^L_{\tilde{\tilde{B}}}\right), \left(b_1^U, b_2^U, b_3^U, b_4^U; w^U_{\tilde{\tilde{B}}}\right)\right] \\ &= \left[\begin{array}{l} \left(a_1^L + b_1^L, a_2^L + b_2^L, a_3^L + b_3^L, a_4^L + b_4^L; \min\left(w^L_{\tilde{\tilde{A}}}, w^L_{\tilde{\tilde{B}}}\right)\right), \\ \left(a_1^U + b_1^U, a_2^U + b_2^U, a_3^U + b_3^U, a_4^U + b_4^U; \min\left(w^U_{\tilde{\tilde{A}}}, w^U_{\tilde{\tilde{B}}}\right)\right) \end{array}\right] \end{aligned} \quad (9)$$

(ii) The difference of two interval-valued trapezoidal fuzzy numbers $\tilde{\tilde{A}} - \tilde{\tilde{B}}$

$$\begin{aligned}\tilde{\tilde{A}}-\tilde{\tilde{B}}&=\left[\left(a_1^L,a_2^L,a_3^L,a_4^L;w_{\tilde{A}}^{\sim L}\right),\left(a_1^U,a_2^U,a_3^U,a_4^U;w_{\tilde{A}}^{\sim U}\right)\right]\\&\quad-\left[\left(b_1^L,b_2^L,b_3^L,b_4^L;w_{\tilde{B}}^{\sim L}\right),\left(b_1^U,b_2^U,b_3^U,b_4^U;w_{\tilde{B}}^{\sim U}\right)\right]\\&=\left[\begin{array}{c}\left(a_1^L-b_4^L,a_2^L-b_3^L,a_3^L-b_2^L,a_4^L-b_1^L;\min\left(w_{\tilde{A}}^{\sim L},w_{\tilde{B}}^{\sim L}\right)\right),\\\left(a_1^U-b_4^U,a_2^U-b_3^U,a_3^U-b_2^U,a_4^U-b_1^U;\min\left(w_{\tilde{A}}^{\sim U},w_{\tilde{B}}^{\sim U}\right)\right)\end{array}\right]\end{aligned}\tag{10}$$

(iii) The product of two interval-valued trapezoidal fuzzy numbers $\tilde{\tilde{A}}\otimes\tilde{\tilde{B}}$

$$\begin{aligned}\tilde{\tilde{A}}\otimes\tilde{\tilde{B}}&=\left[\left(a_1^L,a_2^L,a_3^L,a_4^L;w_{\tilde{A}}^{\sim L}\right),\left(a_1^U,a_2^U,a_3^U,a_4^U;w_{\tilde{A}}^{\sim U}\right)\right]\\&\quad\otimes\left[\left(b_1^L,b_2^L,b_3^L,b_4^L;w_{\tilde{B}}^{\sim L}\right),\left(b_1^U,b_2^U,b_3^U,b_4^U;w_{\tilde{B}}^{\sim U}\right)\right]\\&=\left[\begin{array}{c}\left(a_1^L\times b_1^L,a_2^L\times b_2^L,a_3^L\times b_3^L,a_4^L\times b_4^L;\min\left(w_{\tilde{A}}^{\sim L},w_{\tilde{B}}^{\sim L}\right)\right),\\\left(a_1^U\times b_1^U,a_2^U\times b_2^U,a_3^U\times b_3^U,a_4^U\times b_4^U;\min\left(w_{\tilde{A}}^{\sim U},w_{\tilde{B}}^{\sim U}\right)\right)\end{array}\right]\end{aligned}\tag{11}$$

(iv) The product between an interval-valued trapezoidal fuzzy number and a constant $\lambda\tilde{\tilde{A}}$

$$\begin{aligned}\lambda\tilde{\tilde{A}}&=\lambda\times\left[\left(a_1^L,a_2^L,a_3^L,a_4^L;w_{\tilde{A}}^{\sim L}\right),\left(a_1^U,a_2^U,a_3^U,a_4^U;w_{\tilde{A}}^{\sim U}\right)\right]\\&=\left[\left(\lambda a_1^L,\lambda a_2^L,\lambda a_3^L,\lambda a_4^L;w_{\tilde{A}}^{\sim L}\right),\left(\lambda a_1^U,\lambda a_2^U,\lambda a_3^U,\lambda a_4^U;w_{\tilde{A}}^{\sim U}\right)\right],\lambda>0\end{aligned}\tag{12}$$

(v) The division between two interval-valued trapezoidal fuzzy numbers $\tilde{\tilde{A}}/\tilde{\tilde{B}}$

$$\begin{aligned}\frac{\tilde{\tilde{A}}}{\tilde{\tilde{B}}}&=\frac{\left[\left(a_1^L,a_2^L,a_3^L,a_4^L;w_{\tilde{A}}^{\sim L}\right),\left(a_1^U,a_2^U,a_3^U,a_4^U;w_{\tilde{A}}^{\sim U}\right)\right]}{\left[\left(b_1^L,b_2^L,b_3^L,b_4^L;w_{\tilde{B}}^{\sim L}\right),\left(b_1^U,b_2^U,b_3^U,b_4^U;w_{\tilde{B}}^{\sim U}\right)\right]}\\&=\left[\begin{array}{c}\left(\min\left(U^L\right),\min\left(\frac{U^L}{x^L}\right),\max\left(\frac{U^L}{y^L}\right),\max\left(U^L\right);\min\left(w_{\tilde{A}}^{\sim L},w_{\tilde{B}}^{\sim L}\right)\right),\\\left(\min\left(U^U\right),\min\left(\frac{U^U}{x^U}\right),\max\left(\frac{U^U}{y^U}\right),\max\left(U^U\right);\min\left(w_{\tilde{A}}^{\sim U},w_{\tilde{B}}^{\sim U}\right)\right)\end{array}\right]\end{aligned}\tag{13}$$

Here,

$$\begin{aligned}U^L&=\left\{\frac{a_1{}^L}{b_1{}^L},\frac{a_2{}^L}{b_2{}^L},\frac{a_3{}^L}{b_3{}^L},\frac{a_4{}^L}{b_4{}^L}\right\},\\U^L&=\left\{\frac{a_1{}^U}{b_1{}^U},\frac{a_2{}^U}{b_2{}^U},\frac{a_3{}^U}{b_3{}^U},\frac{a_4{}^U}{b_4{}^U}\right\},\end{aligned}\tag{14}$$

$$x^L=\min\left(U^L\right),x^U=\min\left(U^U\right),y^L=\max\left(U^L\right),y^U\ \max\left(U^U\right),\tag{15}$$

and the operator "/" denotes exclusion of a certain term from sets U^L andU^U.

(vi) Rising to the power of a constant λ

$$\begin{aligned}\tilde{\tilde{A}}^{\lambda}&=\left[\left(a_1^L,a_2^L,a_3^L,a_4^L;w_{\tilde{A}}^{\sim L}\right),\left(a_1^U,a_2^U,a_3^U,a_4^U;w_{\tilde{A}}^{\sim U}\right)\right]^{\lambda}\\&\quad\cdot\left[\left(\left(a_1^L\right)^{\lambda},\left(a_2^L\right)^{\lambda},\left(a_3^L\right)^{\lambda},\left(a_4^L\right)^{\lambda},w_{\tilde{A}}^{\sim L}\right),\left(\left(a_1^U\right)^{\lambda},\left(a_2^U\right)^{\lambda},\left(a_3^U\right)^{\lambda},\left(a_4^U\right)^{\lambda},w_{\tilde{A}}^{\sim U}\right)\right]\end{aligned}\tag{16}$$

By considering (Equation (3)), we can define the COG point for an interval-valued trapezoidal fuzzy number $\tilde{\tilde{A}}=[\tilde{\tilde{A}}^L,\tilde{\tilde{A}}^U]=[(a_1^L,a_2^L,a_3^L,a_4^L;w_{\tilde{A}}^{\sim L}),(a_1^U,a_2^U,a_3^U,a_4^U;w_{\tilde{A}}^{\sim U})]$. Firstly, Equation (3) is employed to obtain the coordinates of the COG points for the lower and upper values of $\tilde{\tilde{A}}$, viz., $(x_{\tilde{A}}^{\sim L},y_{\tilde{A}}^{\sim L})$ and $(x_{\tilde{A}}^{\sim U},y_{\tilde{A}}^{\sim U})$ for $\tilde{\tilde{A}}^L$ and $\tilde{\tilde{A}}^U$, respectively. Secondly, the COG of $(x_{\tilde{A}}^{\sim},y_{\tilde{A}}^{\sim})$ is found as follows:

$$\begin{cases}x_{\tilde{A}}^{\sim}=\dfrac{\left(x_{\tilde{A}}^{\sim L}+x_{\tilde{A}}^{\sim U}\right)}{2},\\[2ex]y_{\tilde{A}}^{\sim}=\dfrac{\left(y_{\tilde{A}}^{\sim L}+y_{\tilde{A}}^{\sim U}\right)}{2}.\end{cases}\tag{17}$$

Let there exist an interval-valued fuzzy number.

$$\tilde{\tilde{B}}=\left[\tilde{\tilde{B}}^L,\tilde{\tilde{B}}^U\right]=\left[\left(b_1^L,b_2^L,b_3^L,b_4^L;w_{\tilde{B}}^{\sim L}\right),\left(b_1^U,b_2^U,b_3^U,b_4^U;w_{\tilde{B}}^{\sim U}\right)\right].\tag{18}$$

One can define the COG point $(x_{\tilde{B}}^{\sim},y_{\tilde{B}}^{\sim})$ in the spirit of Equation (3). The distance $d_{\tilde{A}}^{\sim}$ and $d_{\tilde{B}}^{\sim}$ between the origin point and two generalized interval-valued trapezoidal fuzzy numbers $\tilde{\tilde{A}}$ and $\tilde{\tilde{B}}$

$$\tilde{\tilde{A}}=\left[\tilde{\tilde{A}}^L,\tilde{\tilde{A}}^U\right]=\left[\left(a_1^L,a_2^L,a_3^L,a_4^L;w_{\tilde{A}}^{\sim L}\right),\left(a_1^U,a_2^U,a_3^U,a_4^U;w_{\tilde{A}}^{\sim U}\right)\right],\tag{19}$$

and

$$\widetilde{\widetilde{B}} = \left[\widetilde{\widetilde{B}}^L, \widetilde{\widetilde{B}}^U\right] = \left[\left(b_1^L, b_2^L, b_3^L, b_4^L; w_{\widetilde{\widetilde{B}}}^{\sim L}\right), \left(b_1^U, b_2^U, b_3^U, b_4^U; w_{\widetilde{\widetilde{B}}}^{\sim U}\right)\right], \tag{20}$$

respectively, are calculated by virtue of the Euclidean distance:

$$d_{\widetilde{\widetilde{A}}} = \sqrt{x_{\widetilde{\widetilde{A}}}^2 + y_{\widetilde{\widetilde{A}}}^2}, \tag{21}$$

$$d_{\widetilde{\widetilde{B}}} = \sqrt{x_{\widetilde{\widetilde{B}}}^2 + y_{\widetilde{\widetilde{B}}}^2}. \tag{22}$$

Accordingly, if $d_{\widetilde{\widetilde{A}}} > d_{\widetilde{\widetilde{B}}}$, then $\widetilde{\widetilde{A}} \succ \widetilde{\widetilde{B}}$.

The COG coordinates can also be employed when estimating the distance between two interval-valued trapezoidal fuzzy numbers say $\widetilde{\widetilde{A}}$ and $\widetilde{\widetilde{B}}$ [50, 53].

$$d\left(\widetilde{\widetilde{A}}, \widetilde{\widetilde{B}}\right) = \sqrt{\frac{\left\{\left(x_{\widetilde{\widetilde{A}}}^{\sim L} - x_{\widetilde{\widetilde{B}}}^{\sim L}\right)^2 + \left(y_{\widetilde{\widetilde{A}}}^{\sim L} - y_{\widetilde{\widetilde{B}}}^{\sim L}\right)^2 + \left(x_{\widetilde{\widetilde{A}}}^{\sim U} - x_{\widetilde{\widetilde{B}}}^{\sim U}\right)^2 + \left(y_{\widetilde{\widetilde{A}}}^{\sim U} - y_{\widetilde{\widetilde{B}}}^{\sim U}\right)^2\right\}}{4}}. \tag{23}$$

Alternatively, one can employ the following technique (Liu and Jin, 2012):

$$d\left(\widetilde{\widetilde{A}}, \widetilde{\widetilde{B}}\right) = \frac{1}{8}\left(\begin{array}{c} \left|w_{\widetilde{\widetilde{A}}}^{\sim L} a_1{}^L - w_{\widetilde{\widetilde{B}}}^{\sim L} b_1{}^L\right| + \left|w_{\widetilde{\widetilde{A}}}^{\sim L} a_2{}^L - w_{\widetilde{\widetilde{B}}}^{\sim L} b_2{}^L\right| + \left|w_{\widetilde{\widetilde{A}}}^{\sim L} a_3{}^L - w_{\widetilde{\widetilde{B}}}^{\sim L} b_3{}^L\right| \\ + \left|w_{\widetilde{\widetilde{A}}}^{\sim L} a_4{}^L - w_{\widetilde{\widetilde{B}}}^{\sim L} b_4{}^L\right| + \left|w_{\widetilde{\widetilde{A}}}^{\sim U} a_1{}^U - w_{\widetilde{\widetilde{B}}}^{\sim U} b_1{}^U\right| + \left|w_{\widetilde{\widetilde{A}}}^{\sim U} a_2{}^U - w_{\widetilde{\widetilde{B}}}^{\sim U} b_2{}^U\right| + \\ \left|w_{\widetilde{\widetilde{A}}}^{\sim U} a_3{}^U - w_{\widetilde{\widetilde{B}}}^{\sim U} b_3{}^U\right| + \left|w_{\widetilde{\widetilde{A}}}^{\sim U} a_4{}^U - w_{\widetilde{\widetilde{B}}}^{\sim U} b_4{}^U\right| \end{array}\right). \tag{24}$$

4.3. The Generalized Interval-Valued Trapezoidal Fuzzy Number Ordered Weighted Geometric Average Operator (OWGAO). [52] proposed an interesting and well-grounded approach, named the ordered weighted average (OWA), which enabled to aggregate the variables in terms of their order in the set. Such an approach enables to avoid the subjectivity arising from group decision-making. [51] and later [24] introduced the generalized interval-valued trapezoidal fuzzy number ordered weighted geometric (GIFN-OWG) operator, which was able to tackle fuzzy ratings at 1st level. But in the presented research work, the (GIFN-OWGA) is merged with average fuzzy rule and modified with renaming generalized interval-valued trapezoidal fuzzy number ordered weighted geometric average (GIFN-OWG) operator.

Let $\widetilde{\widetilde{A}}_j$ be a set of generalized interval-valued trapezoidal fuzzy
numbers,-
$\widetilde{\widetilde{A}}_{jk} = [\widetilde{\widetilde{A}}_{jk}^L, \widetilde{\widetilde{A}}_{jk}^U] = [(a_{1jk}^L, a_{2jk}^L, a_{3jk}^L, a_{4jk}^L; \widetilde{\widetilde{w}}_{A_{jk}^L}), (a_{1jk}^U, a_{2jk}^U, a_{3jk}^U, a_{4jk}^U; \widetilde{\widetilde{w}}_{A_{jk}^U})]$, with $jk = 1, 2, 3, \cdots, n$, Ω is the set of all generalized interval-valued trapezoidal fuzzy numbers; $(\sigma(1), \sigma(2), \cdots, \sigma(n))$ is a permutation of $(1, 2, 3, .., n)$, such that $\widetilde{\widetilde{A}}_{\sigma(jk-1)} \succ \widetilde{\widetilde{A}}_{\sigma(jk)}, \forall jk = 2, 3, \cdots, n$. Then, we have GITFNOWGA: $\Omega^n \longrightarrow \Omega$, which can be employed in the following way:

$$\begin{aligned} \text{GITFNOWGA}_w\left(\widetilde{\widetilde{A}}_1, \widetilde{\widetilde{A}}_2, \cdots, \widetilde{\widetilde{A}}_n\right) &= \frac{\prod_{jk=1}^n \left(\widetilde{\widetilde{A}}_{\sigma(jk)}\right)^{W_{jk}}}{\sum_{jk}^n \xi_{jk}} \\ &= \prod_{jk=1}^n \left[\left(a_{1\sigma(jk)}^L, a_{2\sigma(jk)}^L, a_{3\sigma(jk)}^L, a_{4\sigma(jk)}^L; w_{\widetilde{\widetilde{A}}_{\sigma(jk)}}^{\sim L}\right), \right. \\ &\quad \left. \times \left(a_{1\sigma(jk)}^U, a_{2\sigma(jk)}^U, a_{3\sigma(jk)}^U, a_{4\sigma(jk)}^U; w_{\widetilde{\widetilde{A}}_{\sigma(jk)}}^{\sim U}\right)\right]^{W_{jk}}. \end{aligned} \tag{25}$$

Here, w_{jk} is a weight of subdimensions to the jk_{th} largest variable $(jk = 1, 2, \cdots, n)$. The vector of weights can be obtained by virtue of the following equation [62]:

$$w_{jk+1} = \frac{C_{n-1}^i}{2^{n-1}}, \forall i = 0, 1, 2, 3 \cdots, n-1. \tag{26}$$

5. The Crisp MULTI-MOORA Algorithm

The Multiobjective Optimization by Ratio Analysis (MOORA) algorithm was introduced by [43], Sahu et al. [24], Bu et al. [40], and He et al. [41] and extended the algorithm to make it more robust as MULTI-MOORA (MOORA plus the full multiplicative form).

The MOORA algorithm begins with matrix X where its elements x_{ij} denote i_{th} alternative of j_{th} objective $(i = 1, 2, \cdots, m; j = 1, 2, \cdots, n)$. The MOORA algorithm consists of two parts: the ratio system and the reference point approach. The MULTI-MOORA algorithm includes internal normalization and treats originally all the objectives equally important. In principle, all stakeholders interested in the issue only could give more importance to an objective. Therefore, they could either multiply the dimensionless number representing the response on an objective with a significance coefficient or they could decide beforehand to split an objective into different subobjectives.

5.1. The Ratio System of MOORA. Ratio system defines data normalization by comparing alternative of an objective to all values of the objective:

$$x_{ij}^* = \frac{x_{ij}}{\sqrt{\sum_{i=1}^m x_{ij}^2}}. \tag{27}$$

Here, x_{ij}^* denotes i_{th} alternative of j_{th} objective. Usually these numbers belong to the interval [0, 1]. These indicators are added (if desirable value of indicator is maximum) or subtracted (if desirable value is minimum); thus, the

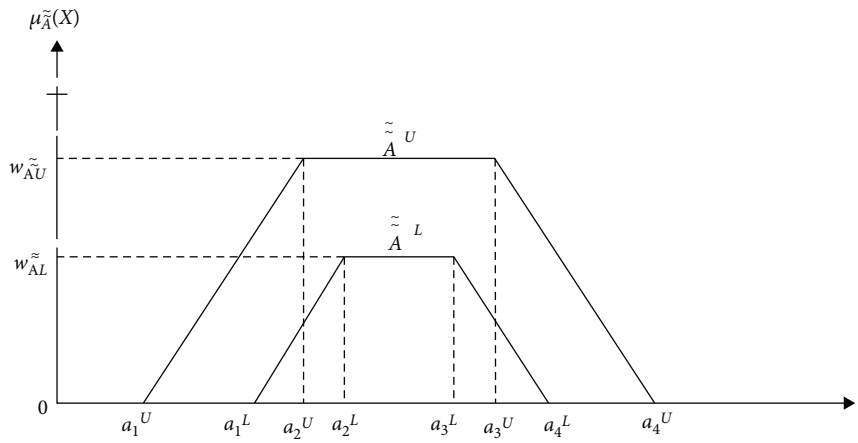

Figure 3: Interval-valued trapezoidal fuzzy numbers.

summarizing index of each alternative is derived in this way:

$$y_i^* = \sum_{j=1}^{g} x_{ij}^* - \sum_{j=g+1}^{n} x_{ij}^*. \tag{28}$$

Here, $g = 1, \cdots, n$ denotes number of objectives to be maximized. Then, every ratio is given the rank: the higher the index, the higher the rank.

In some cases, it is often observed that some attributes are more important than the others. In order to give more importance to an attribute, it could be multiplied with its corresponding weight (significance coefficient) [38, 42, 62]. When these attribute weights are taken into consideration, Equation (28) becomes as follows:

$$y_i^* = \sum_{j=1}^{g} w_j x_{ij}^* - \sum_{j=g+1}^{n} w_j x_{ij}^*, j = 1, 2, \cdots, n. \tag{29}$$

Here, w_j is the weight of j_{th} subdimensions.

5.2. The Reference Point of MOORA. Reference point approach is based on the ratio system. The Maximal Objective Reference Point (vector) is found according to ratios found by employing Eq. The j_{th} coordinate of the reference point can be described as ($r_j = \max\ x_{ij}^*$) in the case of maximization. Every coordinate of this vector represents maximum or minimum of certain objective (indicator). Then, every element of normalized response matrix is recalculated, and the final rank is given according to deviation from the reference point and the Min-Max Metric of Tchebycheff:

$$\min_i \left(\max_j \left| r_j - x_{ij}^* \right| \right). \tag{30}$$

5.3. The Full Multiplicative Form and MULTI-MOORA. [43] proposed MOORA to be updated by the full multiplicative form algorithm embodying maximization as well as minimization of purely multiplicative utility function. Overall utility of the i_{th} alternative can be expressed as dimensionless number:

$$U_i' = \frac{A_i}{B_i}. \tag{31}$$

Here, $A_i = \prod_{j=1}^{g} x_{ij}$; $i = 1, 2, \cdots, m$ denotes the product of objectives of the i_{th} alternative to be maximized with $g = 1, 2, \cdots, n$ being the number of objectives to be maximized and where $B_i = \prod_{j=g+1}^{n} x_{ij}$; $i = 1, 2, \cdots, m$ denotes the product of objectives of the i_{th} alternative to be minimized with $n - g$ being the number of objectives (indicators) to be minimized. Thus, MULTI-MOORA summarizes MOORA (i.e., ratio system and reference point) and the full multiplicative form.

5.4. MULTI-MOORA Algorithm Based upon Interval-Valued Trapezoidal Fuzzy Numbers. Let $E = 1, 2, \cdots, e$ denote the e_{th} expert involved in a decision-making process. Suppose that the experts provide ratings for each i_{th} alternative against each j_{th} criterion with $i = 1, 2, \cdots, m$ and $j = 1, 2, \cdots, n$. The set of criteria can be split into two subsets, namely, those of cost criteria, C, and benefit criteria, B. Cost criteria are to be minimized, whereas benefit criteria are to be maximized. Each criterion can be attributed with respective weight W_j, such that $W_j \geq 0$, and $\sum_j W_j = 1$.

Step 1. Each of decision-makers constructs his own decision matrix: $(\tilde{\tilde{A}}^k)_{m \times n}$ with elements $\tilde{\tilde{a}}_{ij}^k = [(a_{ijk1}^L, a_{ijk2}^L, a_{ijk3}^L, a_{ijk4}^L ; w_{ijk}^L), (a_{ijk1}^U, a_{ijk2}^U, a_{ijk3}^U, a_{ijk4}^U ; w_{ijk}^U)]$ being responses of alternatives on criteria.

Table 1: Dynamic multidimension Coal Refinery Process Absorbability Index (CRPAI) structure.

Coal refinery process, (C)	Dimensions; ξ_j	Subdimensions; ξ_{jk}
Coal Refinery Process Absorbability Index evaluation	Absorbability index on crushing and breaking process, ξ_1	Effective primary breaking with low gas emission, ξ_{11}
		Effective final breaking with low gas emission, ξ_{12}
	Absorbability index on sizing process, ξ_2	Effective machining for sizing with low gas emission, ξ_{21}
	Absorbability index on storage and stockpiling process and density separation, ξ_3	Toxic gas emission on the stockpiling of coal, ξ_{31}
		Emission of toxic gases on density separation, ξ_{32}
	Absorbability index on density separation and washing process, ξ_4	Emission of toxic gases on quenching process, ξ_{41}
		Water prequenching treatment level, ξ_{42}
		Water final-quenching treatment level, ξ_{43}
	Absorbability index on drying process, ξ_5	Moisture drying pretreatment level, ξ_{42}, ξ_{51}
		Moisture drying final treatment level, ξ_{51}

Table 2: Nine-member linguistic terms (rating scale) and their corresponding interval-valued fuzzy numbers.

Linguistic terms	Interval-valued trapezoidal fuzzy numbers
Absolutely poor, AP	[(0.0, 0.0, 0.0, 0.0; 0.5), (0.0, 0.0, 0.0, 0.0; 1.0)]
Very poor, VP	[(0.0075, 0.0075, 0.015, 0.0525; 0.5), (0.0, 0.0, 0.02, 0.07; 1.0)]
Poor, P	[(0.0875, 0.12, 0.16, 0.1825; 0.5), (0.04, 0.10, 0.18, 0.23; 1.0)]
Fairly poor, FP	[(0.2325, 0.255, 0.325, 0.3575; 0.5), (0.17, 0.22, 0.36, 0.42; 1.0)]
Medium, M	[(0.4025, 0.4525, 0.5375, 0.5676; 0.5), (0.32, 0.41, 0.58, 0.65; 1.0)]
Fairly satisfactory, FS	[(0.65, 0.6725, 0.7575, 0.79; 0.5), (0.58, 0.63, 0.80, 0.86; 1.0)]
Satisfactory, S	[(0.7825, 0.815, 0.885, 0.9075; 0.5), (0.72, 0.78, 0.92, 0.97; 1.0)]
Very impressive, VI	[(0.9475, 0.985, 0.9925, 0.9925; 0.5), (0.93, 0.98, 1.0, 1.0; 1.0)]
Absolutely impressive, AI	[(1.0, 1.0, 1.0, 1.0; 0.5), (1.0, 1.0, 1.0, 1.0; 1.0)]

Step 2. Individual decision matrices are aggregated by employing the GITFNOWGA operator.

$$\mathrm{GITFNOWGA}_w\left(\tilde{\tilde{a}}_{ij}^1, \tilde{\tilde{a}}_{ij}^2, \cdots, \tilde{\tilde{a}}_{ij}^K\right) = \prod_{k=1}^{K}\left(a_{ij}^{\sigma(k)}\right)^{w_k}, \forall i, j. \tag{32}$$

Here, w_k is the weight of the k_{th} largest response obtained by Equation (26) and

$$\tilde{\tilde{a}}_{ij} = \left[\left(a_{ij1}^L, a_{ij2}^L, a_{ij3}^L, a_{ij4}^L; w_{ij}^L\right), \left(a_{ij1}^U, a_{ij2}^U, a_{ij3}^U, a_{ij4}^U; w_{ij}^U\right)\right]. \tag{33}$$

It must be noted that Equation (21) is employed to compare the values of the generalized interval-valued trapezoidal fuzzy numbers.

Step 3. In case some of criteria involve numeric data, the normalization has to be carried out.

$$\begin{aligned}\tilde{\tilde{x}}_{ij} &= \left[\left(\frac{a_{ij1}^L}{d_j}, \frac{a_{ij2}^L}{d_j}, \frac{a_{ij3}^L}{d_j}, \frac{a_{ij4}^L}{d_j}; w_{ij}^L\right), \left(\frac{a_{ij1}^U}{d_j}, \frac{a_{ij2}^U}{d_j}, \frac{a_{ij3}^U}{d_j}, \frac{a_{ij4}^U}{d_j}; w_{ij}^U\right)\right] \\ &= \left[\left(x_{ij1}^L, x_{ij2}^L, x_{ij3}^L, x_{ij4}^L; w_{ij}^L\right), \left(x_{ij1}^U, x_{ij2}^U, x_{ij3}^U, x_{ij4}^U; w_{ij}^U\right)\right], j = 1, 2, \cdots, n; i = 1, 2, \cdots, n.\end{aligned} \tag{34}$$

Here, $d_j = \sqrt{\sum_{i=1}^m \sum_{p=1}^4 \left(a_{ijp}^L\right)^2 + \sum_{i=1}^m \sum_{p=1}^4 \left(a_{ijp}^U\right)^2}$, $p = \{1, 2, 3, 4\}$ for $\forall j = 1, 2, \cdots, n$.

Step 4. The ratio system:

Table 3: Appropriateness ratings (in linguistic scale) against CRPAI subdimensions assigned by EP.

θ_i	ξ_{ij}	E_1	E_2	E_3	E_4	E_5
θ_1	ξ_{11}	S	VI	M	FS	AI
	ξ_{12}	VI	S	FS	M	AI
θ_2	ξ_{11}	FS	S	S	S	S
	ξ_{12}	S	S	FS	S	S
θ_3	ξ_{11}	S	S	S	VI	VI
	ξ_{12}	S	S	S	VI	VI
θ_4	ξ_{11}	M	M	M	M	M
	ξ_{12}	M	M	M	M	M
θ_1	ξ_{21}	FS	S	FS	S	FS
θ_2	ξ_{21}	FP	M	M	M	M
θ_3	ξ_{21}	FS	S	FS	FS	FS
θ_4	ξ_{21}	S	S	VI	VI	S
θ_1	ξ_{31}	AI	AI	AI	VI	VI
	ξ_{32}	AI	AI	AI	VI	VI
θ_2	ξ_{31}	S	VI	VI	VI	VI
	ξ_{32}	S	VI	VI	VI	VI
θ_3	ξ_{31}	FS	S	S	S	S
	ξ_{32}	FS	S	S	S	S
θ_4	ξ_{31}	S	S	S	VI	VI
	ξ_{32}	S	S	S	VI	VI
θ_1	ξ_{41}	M	M	S	VI	M
	ξ_{42}	M	M	S	VI	M
	ξ_{41}	M	M	S	VI	M
θ_2	ξ_{41}	FS	S	M	M	FS
	ξ_{42}	FS	S	M	M	FS
	ξ_{43}	FS	S	M	M	FS
θ_3	ξ_{41}	FP	M	S	S	M
	ξ_{42}	FP	M	S	S	M
	ξ_{43}	FP	M	S	S	M
θ_4	ξ_{41}	S	FS	M	M	FS
	ξ_{42}	FS	S	M	M	FS
	ξ_{43}	FS	S	M	M	FS
θ_1	ξ_{51}	AI	AI	AI	VI	VI
	ξ_{52}	VI	AI	AI	AI	VI
θ_2	ξ_{51}	S	VI	S	VI	VI
	ξ_{52}	S	VI	S	VI	VI
θ_3	ξ_{51}	FS	S	S	FS	S
	ξ_{52}	FS	S	S	FS	S
θ_4	ξ_{51}	S	S	S	VI	VI
	ξ_{52}	VI	S	S	S	VI

The normalized values are added up for the benefit criteria and subtracted for the cost criteria:

$$\mathrm{RS}_i = \sum_{j\in B}\tilde{\tilde{x}}_{ij} - \sum_{j\in C}\tilde{\tilde{x}}_{ij} = \left[\left(\mathrm{RS}_{i1}^L, \mathrm{RS}_{i2}^L, \mathrm{RS}_{i3}^L, \mathrm{RS}_{i4}^L ; w_{\mathrm{RS}_i}^L\right), \cdot \left(\mathrm{RS}_{i1}^U, \mathrm{RS}_{i2}^U, \mathrm{RS}_{i3}^U, \mathrm{RS}_{i4}^U ; w_{\mathrm{RS}_i}^U\right)\right]. \tag{35}$$

Here, RS_i denotes the overall utility of the i_{th} alternative in terms of the ratio system. The alternatives are then ranked by measuring their distances from the origin point in the spirit of Equation (21). Specially, alternatives with higher distances receive higher ranks.

Step 5. The reference point approach:

For the sake of convenience, one can employ the Maximal Utopian Reference Point (MURP), rather than the Maximal Objective Reference Point. In the case of the generalized interval-valued trapezoidal fuzzy numbers, MURP is defined as follows:

$$\tilde{\tilde{r}}_j = \begin{cases} (1, 1, 1, 1 ; 1), & \forall j \in B, \\ (0, 0, 0, 0 ; 1), & \forall j \in C. \end{cases} \tag{36}$$

Therefore, Equations (23) and (24) can be utilized to identify the maximal deviation from the MURP for each alternative:

$$\max_j d\left(\tilde{\tilde{r}}_j, \tilde{\tilde{x}}_{ij}\right). \tag{37}$$

Then, the alternatives are ranked by minimizing the maximal deviances found in Equation (36).

Step 6. The full multiplicative form:

The fuzzy utility of the i_{th} alternative is obtained by employing Equations (12) and (14).

$$\tilde{\tilde{U}}_i = \frac{\tilde{\tilde{A}}_i}{\tilde{\tilde{B}}_i}. \tag{38}$$

Here, $\tilde{\tilde{A}}_i = \prod_{j\in B}\tilde{\tilde{x}}_{ij}$, $i = 1, 2, \cdots, m$ denotes the product of objectives of the i_{th} alternative to be maximized with B being the set of objectives to be maximized and where $\tilde{\tilde{B}}_i = \prod_{j\in C}\tilde{\tilde{x}}_{ij}$ denotes the product of objectives of the i_{th} alternative to be minimized with C being the set of objectives (indicators) need to be minimized. The alternatives are ranked in descending order of $\tilde{\tilde{U}}_i$ by employing Equation (21).

Table 4: Computed aggregated fuzzy ratings against CRPAI subdimensions (ξ_j).

ξ_j	θ_i	Aggregated fuzzy ratings against CRPAI subdimensions; ξ_j
ξ_1	θ_1	[(0.764,0.796,0.856,0.877,0.500),(0.706,0.765,0.887,0.928,1.000)]
	θ_2	[(0.774,0.804,0.869,0.890,0.500),(0.716,0.772,0.901,0.947,1.000)]
	θ_3	[(0.830,0.864,0.917,0.933,0.500),(0.779,0.837,0.944,0.979,1.000)]
	θ_4	[(0.625,0.661,0.742,0.770,0.500),(0.550,0.621,0.781,0.840,1.000)]
ξ_2	θ_1	[(0.688,0.697,0.715,0.721,0.500),(0.671,0.688,0.724,0.736,1.000)]
	θ_2	[(0.389,0.437,0.522,0.552,0.500),(0.308,0.395,0.564,0.633,1.000)]
	θ_3	[(0.657,0.659,0.662,0.663,0.500),(0.654,0.657,0.664,0.666,1.000)]
	θ_4	[(0.830,0.864,0.917,0.933,0.500),(0.779,0.837,0.944,0.979,1.000)]
ξ_3	θ_1	[(0.983,0.995,0.998,0.998,0.500),(0.978,0.994,1.000,1.000,1.000)]
	θ_2	[(0.937,0.974,0.986,0.987,0.500),(0.916,0.967,0.995,0.998,1.000)]
	θ_3	[(0.718,0.743,0.795,0.812,0.500),(0.668,0.717,0.820,0.857,1.000)]
	θ_4	[(0.830,0.864,0.917,0.933,0.500),(0.779,0.837,0.944,0.979,1.000)]
ξ_4	θ_1	[(0.500,0.549,0.632,0.660,0.500),(0.418,0.507,0.673,0.737,1.000)]
	θ_2	[(0.567,0.589,0.624,0.636,0.500),(0.525,0.570,0.641,0.666,1.000)]
	θ_3	[(0.479,0.525,0.609,0.639,0.500),(0.396,0.482,0.650,0.717,1.000)]
	θ_4	[(0.830,0.864,0.917,0.933,0.500),(0.779,0.837,0.944,0.979,1.000)]
ξ_5	θ_1	[(0.983,0.995,0.998,0.998,0.500),(0.978,0.994,1.000,1.000,1.000)]
	θ_2	[(0.937,0.974,0.986,0.987,0.500),(0.916,0.967,0.995,0.998,1.000)]
	θ_3	[(0.718,0.743,0.795,0.812,0.500),(0.668,0.717,0.820,0.857,1.000)]
	θ_4	[(0.830,0.864,0.917,0.933,0.500),(0.779,0.837,0.944,0.979,1.000)]

Table 5: Preference orders computed by ratio system analysis algorithm.

θ_i	RS_i	$d_{A^{\approx}}$	Preference orders
θ_1	[(3.920,4.033,4.199,4.253,5.00),(3.751,3.947,4.283,4.401,1.000)]	8.582	2
θ_2	[(3.603,3.778,3.986,4.052,5.00),(3.380,3.669,4.095,4.242,1.000)]	8.406	4
θ_3	[(3.402,3.535,3.778,3.858,5.00),(3.167,3.411,3.899,4.075,1.000)]	8.456	3
θ_4	[(3.946,4.119,4.410,4.502,5.00),(3.668,3.970,4.558,4.757,1.000)]	8.730	1

Step 7. The dominance theory ([45], [40], [41]) is employed to aggregate the ranks, provided by respective parts of MULTI-MOORA.

6. Empirical Research

In the presented research forum, the authors developed a standard dynamic multidimension Coal Refinery Process Absorbability Index (CRPAI) structure by conducting the real CRP audit and the prior state of arts and proposed the same to CRP companies for finding the best CRP technique/practice to control further air pollution-global warming under discussed twice factors, shown in Table 1.

To simulate the CRPAI, the authors used modified OWGA operator with application of the MULTI-MOORA algorithm embedded with dominance theory. To validate the CRPAI, the authors solved a problem of a CRP company, existing north part of India. The CRP company wanted to evaluate and finalize a reliable CRP alternative amongst available (θ_1, θ_2, θ_3, and θ_4) for controlling further air pollution, occurs due to discussed twice factors. For data modeling of the subdimensions of CRPAI, a board of five highly experience decision-makers E_1, E_2,E_3,E_4, and E_5 are evaluated from the inventory, production, and environmental departments of CRP (case study) company. Next, the expert's panel is invited to sight, audit, and assess the

Table 6: Preference orders computed by reference point algorithm.

θ_i	Max $j\{d(\beta ij, \beta j)$	Preference orders
θ_1	0.562	3
θ_2	0.644	4
θ_3	0.549	2
θ_4	0.476	1

Table 7: Preference orders computed by full multification form (MULTI-MOORA) algorithm.

θ_i	y_i	$d_{A^{\approx}}$	Preference orders
θ_1	[(0.255,0.302,0.385,0.415,0.500),(0.189,0.263,0.432,0.503,1.000)]	1.930	2
θ_2	[(0.150,0.196,0.275,0.304,0.500),(0.097,0.162,0.322,0.398,1.000)]	1.908	4
θ_3	[(0.135,0.165,0.234,0.260,0.500),(0.090,0.136,0.274,0.343,1.000)]	1.919	3
θ_4	[(0.297,0.369,0.524,0.583,0.500),(0.203,0.305,0.621,0.772,1.000)]	1.963	1

capability of alternative CRPs such as θ_1, θ_2, θ_3, and θ_4 with high concern about the discussed twice factors. After that, decision-makers are assisted with linguistic variable scale, expressed 1-9 IVFN scale as shown in Table 2, so that decision-makers can assign appropriateness ratings against individual subdimensions.

The procedural steps are summarized below:

Step 1. Gathering information from the expert group in relation to performance ratings of different evaluation dimensions and subdimensions using linguistic terms:

In order to acquire appropriateness ratings against subdimensions, evaluated board expert's panel, e.g., E_1, E_2, E_3, E_4, and E_5, instructed to assign appropriateness ratings (evaluation score) against subdimensions (associated in proposed structure), which is further transformed into IV-fuzzy number. The appropriateness ratings (in linguistic terms) against evaluated subdimensions assigned by the expert panel corresponding to preferred options, e.g., θ_1, θ_2, θ_3, and θ_4, have depicted in Table 3.

Step 2. Approximation of the linguistic evaluation information by IV trapezoidal fuzzy numbers:

The assigned appropriateness ratings acquired in the form of IVFNs against subdimensions, shown in Table 3, are shifted into 1st level (core dimensions) by using modified GITFN-OWGAO (generalized interval-valued trapezoidal fuzzy number ordered weighted geometric average operator); In Equations (25) and (26), consequently, the problem appeared as structure modeling, revealed in Table 4.

$$\left(\left[\tilde{\tilde{A}}\right]\right) = \begin{array}{c} \\ \theta_1 \\ \theta_2 \\ \theta_3 \end{array} \begin{array}{c} \begin{array}{cccccc} \xi_1 & \xi_1 & \xi_3 & & & \xi_j \end{array} \\ \begin{bmatrix} \xi_{11} & \xi_{12} & \xi_{13} & \cdots\cdots\cdots\cdots\cdots\cdots & & \xi_{ij} \\ \xi_{21} & \xi_{22} & \xi_{23} & \cdots\cdots\cdots\cdots\cdots\cdots\cdots & & \xi_{ij} \\ \xi_{31} & \xi_{32} & \xi_{33} & \cdots\cdots\cdots\cdots\cdots\cdots\cdots & & \xi_{ij} \end{bmatrix} \end{array} \tag{39}$$

Step 3. Normalization:

After forming structure matrix, the IV fuzzy set value against core dimensions is found out in between [0, 1] and core dimensions were beneficial in nature, Hence, structural matrix was not normalized with exploration of Equation (34).

Step 4. The ratio system:

In the ratio system (RS), the values of IVFNs against core dimensions corresponding to CRP alternative or techniques are added up for the benefit criteria and subtracted for the cost criteria with exploration of Equation (35); the results are shown in Table 5. The higher scores are prioritized corresponds to higher preference orders.

Table 8: CRPAI of CR process.

θ_i	Ratio system	Reference point	Full multification form	Dominance theory
θ_1	2	3	2	2
θ_2	4	4	4	4
θ_3	3	2	3	3
θ_4	1	1	1	1

Step 5. Reference point approach:

We define the reference point (ascertained the core dimensions are benefit in nature)

$$\tilde{\tilde{r}}_i = (1, 1, 1, 1\,; 1). \tag{40}$$

Thus, the preference order of preferred CRPs is decided in accordance to their distances from fuzzy reference points and is computed by using Equations (36) and (37). Smaller distances of subdimensions from fuzzy reference points are preferred first, shown in Table 6.

Step 6. The full multiplicative form:

Eventually, Equation (38) is utilized to obtain preference orders of CRP options in accordance to full multiplicative form of MOORA, and the results are shown in Table 7.

Step 7. Final ranking orders by exploring of dominance theory:

By passing through respective computational algorithms of MULTI-MOORA: ratio system analysis, reference point, and full multiplicative form, finally the dominance theory ([45]; [40], [41]) is implemented to summarize the preference orders provided by three respective parts of MULTI-MOORA computational algorithms Bu et al. [40] and He et al. [41]. Hence, the final preference orders of preferred CRP options are presented in Table 8.

As results, the fourth CRP practice/technique/process (θ_4) is found more viable amongst preferred CRP practices/-techniques/processes as per the subjective report of expert panel, whereas the first CRP practice/technique/process (θ_1) and subsequently (θ_3) are found as a second and third best

CRP practice/technique/process. At the other end of spectrum, second coal partner (θ_2) has regrettably found as a worst CRP practice/technique/process, and final preference orders are depicted as $\theta_4 \succ \theta_1 \succ \theta_3 \succ \theta_2$.

It was visibly found that (θ_4) CRP technique/process would be the best to diminish the air pollution, growing universal warming and preserving the ecological balance caused by CRPs said by ([7, 19, 20, 22, 28, 48, 63]; Langergraber).

7. Novelties of Conducted Research

(i) The authors served a research clue in the front of CRP researchers to overcome global warming issue by addressing the discussed twice factors

(ii) The authors proposed and developed CRPAI structure (consisted of coal refinery core dimension and subdimensions corresponding to CRP alternative) to diminish the air pollution

(iii) This research dealt with comprehensive qualitative modeling of dimension and subdimensions corresponding to CRP alternative using expert information

(iv) These authors adapted and applied the three qualitative data optimization algorithms concurrently to robustly opt the viable CRP [40, 41]

(v) The authors modified the IVFN-OWGA (interval-valued fuzzy number ordered weighted geometric average) operator by introducing the average fuzzy rule, depicted in Equations (25) and (26), and consequently, ROAs were made able to tackle core and subdissensions simultaneously by applying the modified OWGA operator (operator was able to act for qualitative modeling of only core level dimensions)

(vi) The authors applied dominance theory to conduct robust comparison amongst the CRPAI preferences, received by the three parts of the MUTIMOORA algorithm [40, 41].

(vii) The modified OWGA operator can be explored in future to tackle the extended or advanced CRP core-subdimensions

8. Conclusions

The coal is determined as a fossil fuel, which releases the several offensive monoparticles and high magnitude of CO_2 to the atmosphere and also causes acid rain and high temperature ([6, 11–13]; CURC 2004; [1, 20]). It is well purported by the ecological scholars that CRP contributes in controlling the air pollution [2, 7, 18, 19, 22, 26, 28, 48, 63]. Therefore, to control such as air pollution and global warming vice versa, the presented research work enrolled a dynamic multidimension CRPAI structure accompanied with the ROA (modification of OWGAO appended with MULTIMOORA with application of dominance theory) algorithm to scrutinize and benchmark the best CRP from available options under linguistic information of expert's panel. This proposed research work assisted the managers to identify the best CRP practice and technique or to opt viable CRPs amongst preferred CRPs that will reduce the air pollution, consequently weaken the virus and ills, and make living people happy.

For making decision, manager can use the proposed dynamic multidimension CRPAI structure and invite the evaluated team of expert of own and other industries to view the preferred CRP alternatives one by one. Next, the expert would ask to provide the ratings against subdimensions of CRPAI structure by using proposed linguistic variable corresponding to IVFN. Next, assigned rating would be substituted by IVFN by using OWGOA. Later, the MUTIMOORA algorithm would deliver results for further comparison by dominance theory and making final decision. This proposed research work assists the managers of CRP to acquire the many coal supplying orders from coal user plants (which strictly follow the green policies). The proposed research dossier helps to finalize the best CRPAI technique or CRPs amongst available for winning the discussed twice factors such as coal logistic from coal refinery location to entry gate of coal user power plants and in process logistic/movement inside the power plants, linked to diminish the air pollution. The wok cannot shape other problems such as liner programming and route algorithm.

Data Availability

The data used to support the findings of this study are available in Tables 5–7.

Conflicts of Interest

The authors declare that there is no conflict of interest regarding the publication of this manuscript.

References

[1] Z. Bian, H. Wang, S. Mu, and H. Leng, "The impact of disposal and treatment of coal mining wastes on environment and farmland," in *International Conference on Waste Management, Environmental Geotechnology and Global Sustainable Development (ICWMEGGSD'07-GzO'07)*, pp. 1–76, Ljubljana, Slovenia, 2007.

[2] P. Billing, "Emission of hazardous air pollutants from coal fired power plants," *Environmental Health & Engineering*, vol. 5, 2011.

[3] Environmental compliance and performance report, *Management of Dust from Coal Mines*, Department of Environment and Climate Change and Water NSW, Sydney, 2010.

[4] F. S. Greb, C. F. Eble, D. C. Peters, and A. R. Papp, *Coal and the Environment*, AGI Environmental Awareness Series, 2006.

[5] B. G. Gottlieb, G. Steven, and L. G. Evans, *Coal ash the toxic threat to our health and environment*, Report from Physicians for Social Responsibility and Earthjustice, 2010.

[6] E. L. Heffern and D. A. Coates, "Geologic history of natural coal-bed fires, Powder River basin, USA," *International Journal of Coal Geology*, vol. 59, no. 1-2, pp. 25–47, 2004.

[7] D. Katoria, D. Sehgal, and S. Kumar, "Environment impact assessment of coal mining," *International Journal of Environmental Engineering and Management*, vol. 4, pp. 245–250, 2013.

[8] V. Munnik, *The Social and Environmental Consequences of Coal Mining in South Africa: A Case Study*, Copyright: Environmental Monitoring Group, 2010.

[9] H. O. Rashid, S. Hossain, Z. Urbi, and S. Islam, "Environmental impact of coal mining: a case study on the Barapukuria coal mining industry," *Bangladesh, Middle-East Journal of Scientific Research*, vol. 21, no. 1, pp. 268–274, 2014.

[10] M. Shealy and J. P. Dorian, "Growing chinese coal use: dramatic resource and environmental implications," *Energy Policy*, vol. 38, no. 5, pp. 2116–2122, 2010.

[11] M. Keating, *Radle to Grave: the environmental impacts from coal*, Clean Air Task Force 77 Summer Street, Boston, MA, USA, 2001.

[12] T. E. Kjellstrom, A. Neller, and R. W. Simpson, "Air pollution and its health impacts: the changing panorama," *Medical Journal of Australia*, vol. 177, no. 11, pp. 604–608, 2002.

[13] P. J. Lloyd, *Coal Mining and the Environment Energy Research Institute*, University of Cape Town, Lloyd-Coal & the Environment IBA Durban, 2002.

[14] K. L. Strellec, "Economic and Environmental Impact Assessment of Proposed Effluent Limitations Guidelines and Standards for the Coal Mining Industry," *Remining and Western Alkaline Subcategories*, vol. 3, 2000.

[15] J. I. Sams III and K. M. Beer, *Effects of Coal-Mine Drainage on Stream Water Quality in the Allegheny and Monongahela River Basins-Sulfate Transport and Trends*, National Water-Quality Assessment Program, 2000.

[16] D. Mamurekli, "Environmental impacts of coal mining and coal utilization in the UK," *Acta Montanistica Slovaca Rocnik*, vol. 15, pp. 134–144, 2010.

[17] L. Ruhl, A. Vengosh, G. S. Dwyer et al., "Survey of the potential environmental and health impacts in the immediate aftermath of the coal ash spill in Kingston, Tennessee," *Environmental Science & Technology*, vol. 43, no. 16, pp. 6326–6333, 2009.

[18] D. Casper, R. Golob, M. Buchanan, J. Tobo, and J. Sykes, *Guide to Prevention and Control of Infectious Diseases in the Workplace*, A Joint Initiative BC service employees union and public service agency, 2007.

[19] S. P. Deshmukh and V. K. Sunnapwar, "Validation of performance measures for green supplier selection in Indian industries," *International Journal of Modern Engineering Research (IJMER)*, vol. 3, no. 3, pp. 1617–1622, 2013.

[20] G. Langergraber and E. Muellegger, "Ecological Sanitation–a way to solve global sanitation problems?," *Environment International*, vol. 31, no. 3, pp. 433–444, 2005.

[21] V. Misra and S. D. Pandey, "Hazardous waste, impact on health and environment for development of better waste management strategies in future in India," *Environment International*, vol. 31, no. 3, pp. 417–431, 2005.

[22] M. K. Chien, "Influences of green supply chain management practices on organizational sustainable performance," *International Journal of Environmental Monitoring and Protection*, vol. 1, no. 1, pp. 12–23, 2014.

[23] G. T. Tsoulfas and C. P. Pappis, "A model for supply chains environmental performance analysis and decision making," *Journal of Cleaner Production*, vol. 16, no. 15, pp. 1647–1657, 2008.

[24] N. K. Sahu, A. K. Sahu, and A. K. Sahu, "Cluster approach integrating weighted geometric aggregation operator to appraise industrial robot," *Kybernetes*, vol. 47, no. 3, pp. 487–524, 2018.

[25] D. Styles, K. O'Brien, and M. B. Jones, "A quantitative integrated assessment of pollution prevention achieved by integrated pollution prevention control licensing," *Environment International*, vol. 35, no. 8, pp. 1177–1187, 2009.

[26] J. Annamalai and M. Namasivayam, "Endocrine disrupting chemicals in the atmosphere: Their effects on humans and wildlife," *Environment International*, vol. 76, pp. 78–97, 2015.

[27] S. M. Chen and J. H. Chen, "Fuzzy risk analysis based on ranking generalized fuzzy numbers with different heights and different spreads," *Expert Systems with Applications*, vol. 36, no. 3, pp. 6833–6842, 2009.

[28] A. Diabat and K. Govindan, "An analysis of the drivers affecting the implementation of green supply chain management," *Resources, Conservation and Recycling*, vol. 55, no. 6, pp. 659–667, 2011.

[29] X. X. Long and X. Jun, "*Green supplier evaluation and controlling based on life cycle assessment theory*'," *Journal of Jiamusi University, Natural Science Edition*, vol. 2, 2007.

[30] A. K. Sahu, N. K. Sahu, and A. Sahu, "Appraisal of CNC machine tool by integrated MULTI-MOORA-IGVN circumstances: an empirical study," in *International Journal of Grey Systems: Theory and Application (IJGSTA)*, Emerald, Group Publishing limited, UK, 2014.

[31] C. Li, L. Xin, Z. Zhijie, D. Zhenghua, Y. Ji, and F. Wang, "Effect of heat treatment on structure and gasification reactivity of petroleum coke," *International Journal of Coal Science & Technology*, vol. 3, pp. 53–61, 2016.

[32] R. Venugopal, J. P. Patel, and C. Bhar, "Coal washing scenario in India and future prospects," *International Journal of Coal Science & Technology*, vol. 3, no. 2, pp. 191–197, 2016.

[33] H. Dhawan, S. Upadhyayula, and D. K. Sharma, "Design of experiments to optimize the extraction parameters of a power grade Indian coal," *International Journal of Coal Science & Technology*, vol. 5, no. 4, pp. 417–429, 2018.

[34] F. Sitorus, J. J. C. Pablo, and R. B. Parada, "Multi-criteria decision making for the choice problem in mining and mineral processing: applications and trends," *Expert Systems with Applications*, vol. 121, no. 1, pp. 393–417, 2019.

[35] K. Pourabdollah, M. S. Zakaria, M. M. Najafizadeh Seyed, and F. Motaghedi, "Experimental investigation of process parameters during graphitization of catalytic coke," *International Journal of Coal Science & Technology*, vol. 6, no. 4, pp. 611–620, 2019.

[36] H. Dhawan, R. Kumar, S. Upadhyayula, K. K. Pant, and D. K. Sharma, "Fractionation of coal through organo-separative refining for enhancing its potential for the CO2-gasification," *International Journal of Coal Science & Technology*, vol. 7, no. 3, pp. 504–515, 2020.

[37] A. Kumar Shukla, Z. Ahmad, M. Sharma et al., "Advances of carbon capture and storage in coal-based power generating units in an Indian context," *Energies*, vol. 13, no. 16, 2020.

[38] S. Chakraborty, "Applications of the MOORA method for decision making in manufacturing environment," *International Journal Advanced Manufacturing Technology*, vol. 54, no. 9-12, pp. 1155–1166, 2011.

[39] V. S. Gadakh, "Application of MOORA algorithm for parametric optimization of milling processes," *International Journal of Applied Engineering Research*, vol. 1, no. 4, 2011.

[40] Z. Bu, M. Prabhu, R. R. Ahmed, and A. K. Sahu, "Exploiting GWmZd Model by Exploring Knowledge-Based Grey-Holistic Technique for Sustainable Vendor Evaluation," *Mathematical Problems in Engineering*, vol. 2020, Article ID 8970947, 18 pages, 2020.

[41] Z. He, X. Ma, J. Luo, A. K. Sahu, A. K. Sahu, and N. K. Sahu, *Exploitation of the Advanced Manufacturing Machine Tool Evaluation Model under Objective-Grey Information: A Knowledge-Based Cluster with the Grey Relational Analysis Approach*, Grey Systems: Theory and Application, 2020.

[42] W. K. M. Brauers and E. K. Zavadskas, "Robustness of the MULTI-OBJECTIVE MOORA METHOD with a test for the facilities sector," *Technological and Economic Development of Economy*, vol. 15, no. 2, pp. 325–375, 2009.

[43] W. K. M. Brauers and E. K. Zavadskas, "Project management by MULTIMOORA as an instrument for transition economies / PROJEKTŲ VADYBA SU MULTIMOORA KAIP PRIEMONĖ PEREINAMOJO LAIKOTARPIO ŪKIAMS," *Technological and Economic Development of Economy*, vol. 16, no. 1, pp. 5–24, 2010.

[44] W. K. M. Brauers, A. Balezentis, and T. Balezentis, "MULTIMOORA for the EU member states updated with fuzzy number theory / NERAIŠKIŲJŲ SKAIČIU TEORIJA PAPILDYTAS MULTIMOORA METODAS EUROPOS SĄJUNGOS VALSTYBIŲ NARIŲ IŠSIVYSTYMO VERTINIMUI," *Technological and Economic Development of Economy*, vol. 17, no. 2, pp. 259–290, 2011.

[45] W. K. M. Brauers and E. K. Zavadskas, "MULTIMOORA optimization used to decide on a bank loan to buy property," *Technologic al and Economic Development of Economy*, vol. 17, no. 1, pp. 174–188, 2011.

[46] S. M. Chen and K. Sanguansat, "Analyzing fuzzy risk based on similarity measures between interval-valued fuzzy numbers," *Expert Systems with Applications*, vol. 38, no. 7, pp. 8612–8621, 2011.

[47] G. D. Li, D. Yamaguchi, and M. Nagai, "A grey-based decision-making approach to the supplier selection problem," *Mathematical and Computer Modelling*, vol. 46, no. 3-4, pp. 573–581, 2007.

[48] M. Kutz, *Environmentally conscious materials handling*, John Wiley & Sons, Inc., 2009.

[49] I. Linkov, F. K. Satterstrom, G. Kiker, C. Batchelor, T. Bridges, and E. Ferguson, "From comparative risk assessment to multi-criteria decision analysis and adaptive management: Recent developments and applications," *Environment International*, vol. 32, no. 8, pp. 1072–1093, 2006.

[50] P. D. Liu, "A weighted aggregation operators multi-attribute group decision-making method based on interval-valued trapezoidal fuzzy numbers," *Expert Systems with Applications*, vol. 38, no. 1, pp. 1053–1060, 2011.

[51] P. D. Liu and F. Jin, "A multi-attribute group decision-making method based on weighted geometric aggregation operators of interval-valued trapezoidal fuzzy numbers," *Applied Mathematical Modelling*, vol. 36, no. 6, pp. 2498–2509, 2012.

[52] R. R. Yager, "On ordered weighted averaging aggregation operators in multicriteria decisionmaking," *IEEE Transactions on Systems, Man and Cybernetics*, vol. 18, no. 1, pp. 183–190, 1988.

[53] P. D. Liu, "An extended TOPSIS algorithm for multiple attribute group decision making based on generalized interval-valued trapezoidal fuzzy numbers," *Informatica*, vol. 35, pp. 185–196, 2011.

[54] J. Zhang, D. Wu, and D. L. Olson, "The method of grey related analysis to multiple attribute decision making problems with interval numbers," *Mathematical and Computer Modelling*, vol. 42, no. 9-10, pp. 991–998, 2005.

[55] S. H. Chen, "Operations of fuzzy numbers with step form membership function using function principle," *Information Sciences*, vol. 108, no. 1-4, pp. 149–155, 1998.

[56] T. H. Comes, M. Hiete, N. Wijngaards, and F. Schultmann, "Decision maps: A framework for multi-criteria decision support under severe uncertainty," *Decision Support Systems*, vol. 52, no. 1, pp. 108–118, 2011.

[57] S. H. Wei and S. M. Chen, "Fuzzy risk analysis based on interval-valued fuzzy numbers," *Expert Systems with Applications*, vol. 36, no. 2, pp. 2285–2299, 2009.

[58] H. J. Zimmermann, *Fuzzy Set Theory and Its Applications*, Kluwer Academic Publishers, Boston, Dordrecht, London, Second Eds edition, 1991.

[59] A. Zakarian, "Analysis of process models: a fuzzy Logic approach," *International Journal of Advanced Manufacturing Technology*, vol. 17, no. 6, pp. 444–452, 2001.

[60] L. A. Zadeh, "Fuzzy sets," *Information and Control*, vol. 8, no. 3, pp. 338–353, 1965.

[61] L. A. Zadeh, "The concept of a linguistic variable and its application to approximate reasoning–I," *Information Sciences*, vol. 8, no. 3, pp. 199–249, 1975.

[62] T. Balezentis and S. Zeng, "Group multi-criteria decision making based upon interval-valued fuzzy numbers: An extension of the MULTIMOORA method," *Expert Systems with Applications*, vol. 40, no. 2, pp. 543–550, 2013.

[63] P. K. Dey and W. Cheffi, "Green supply chain performance measurement using the analytic hierarchy process: a comparative analysis of manufacturing organisations," *Production Planning & Control: The Management of operations*, vol. 24, no. 8-9, pp. 702–720, 2013.

Hindawi
Adsorption Science & Technology
Volume 2021, Article ID 8790974, 16 pages
https://doi.org/10.1155/2021/8790974

Review Article

Research Progress of Adsorption and Photocatalysis of Formaldehyde on TiO_2/AC

Xinwei Zhu, Denghui Wang, and Shien Hui

School of Energy and Power Engineering, Xi'an Jiaotong University, Xi'an 710049, China

Correspondence should be addressed to Denghui Wang; denghuiwang@163.com

Received 7 September 2021; Revised 23 October 2021; Accepted 25 October 2021; Published 10 November 2021

Academic Editor: George Kyzas

Based on the increasingly serious formaldehyde pollution, effective degradation of formaldehyde has become a practical problem that humans urgently need to solve. Among many treatment methods, activated carbon has the advantages of large specific surface area, high adsorption efficiency, and uniform pore size distribution. As a kind of clean photocatalytic material for formaldehyde degradation, titanium dioxide supported by activated carbon has become a research hotspot to develop adsorption-catalytic materials for formaldehyde degradation. In this paper, the research progress of activated carbon and its modification, the photocatalytic principle and modification of titanium dioxide, and TiO_2/AC materials are reviewed. The results show that the pore size distribution gradient and acidic oxygen-containing functional groups of activated carbon play key roles in the formaldehyde adsorption process. TiO_2 doped with metal ions and nonmetal ions can significantly improve the photocatalytic activity. The TiO_2/AC material can greatly improve the photocatalytic rate and achieve the technical goal of efficient and clean degradation for formaldehyde.

1. Introduction

Relevant research shows that, with the rapid development of economic society, decoration materials are emerging one after another, and most of these materials (such as man-made panels and glue paint) contain pollutants such as formaldehyde [1, 2] which is also known as ant aldehyde, chemical formula HCHO, molecular weight 30.03, formaldehyde gas relative density 1.067, liquid density 0.815 g/cm^3 (-20°C), melting point -92°C, and boiling point -19.5°C. In addition to decoration materials, the bedding (such as bedclothes and pillowcases), wardrobes, carpets, and air fresheners we use every day also contain more or less [3] formaldehyde which has a long release period. Indoor air pollution [4, 5] will occur when the cumulative amount of release exceeds a certain threshold. People spend 80% of their time indoors on average every day [6], so the emission of indoor air pollutants (such as formaldehyde, benzene, and radon) will seriously endanger people's health [7].

Low concentrations of formaldehyde which is recognized as allergen source [8] can cause diseases such as eye redness, tracheitis, and asthma, and high concentrations can induce cerebral palsy [9]. Formaldehyde has been classified as a Category 1 carcinogen by international organizations (Word Health Organization and American Red Cross). In addition, formaldehyde can also cause varying degrees of harm to the nervous system, respiratory system, and immune system of children, the elderly, and pregnant women [10]. Formaldehyde has an inhibitory effect on the immune system and causes decreased neutrophil respiratory burst activity. Formaldehyde inhalation can affect the electropsychological function of the heart, resulting in bradycardia, abnormal or missing P waves, and changes in R-T interval. Apart from health effects, formaldehyde can also reduce people's work efficiency [11].

James et al. and Amesj et al. [12, 13] measured that the emission factors of formaldehyde in rapeseed oil, soybean oil, and fried vegetables were 20.1 mg/kg vegetables, 18.6 mg/kg vegetables, and 12.4 mg/kg vegetables, respectively. In 2018, Zhao et al. [14] explored the emission rates of formaldehyde in the kitchen in the actual cooking process by using the mass balance equation of gaseous pollutants with natural gas as fuel. The research results showed that the emission rates of formaldehyde in the kitchen during

the actual cooking process were $0.876 \pm 0.055 \sim 2.738 \pm 0.590$ mg/min. Hu et al. [15] studied the release parameters of formaldehyde in synthetic rubber, and the results are shown in Table 1. Formaldehyde release is also affected by environmental factors such as temperature and humidity. From the above hazards and emission characteristics, the treatment of formaldehyde and other indoor environmental pollutants has become research hotspot of domestic and foreign scholars.

In the table, C_i stands for formaldehyde concentration, C_{si} stands for formaldehyde concentration in standard state, and EF is calculated as follows:

$$EF = \frac{Csi \times V \times AC}{S}. \quad (1)$$

In recent years, researchers have been working on new ways to remove formaldehyde. The removal method of formaldehyde pollution can be broadly divided into two kinds, one is the source of governance that does not use decoration materials or supplies which contain formaldehyde; the method is more convenient and does not need to put a specific material or process in indoor, but the technical means for the production of decoration materials without formaldehyde are limited, so it is not realistic to remove formaldehyde from the source. The second is posttreatment, such as ventilation method, plant absorption method, plasma purification method, adsorbent adsorption method, and photocatalyst degradation method. Due to the long release cycle of formaldehyde and being easily affected by the season, it is not applicable to take ventilation to remove formaldehyde in some cold areas. Green plants such as cactus, *Chlorophytum*, and aloe [16] can remove low concentration of formaldehyde; however, its normal growth will be affected or even withered in high concentration of indoor, so it has little effect on absorption of formaldehyde. The low-temperature plasma method, which refers to the use of ions to undergo a complex reaction with the molecular structure of formaldehyde to catalyze the degradation of formaldehyde, is an emerging method for removing formaldehyde. Studies [17] have shown that this method has the advantages of fast and efficient and can completely degrade formaldehyde into carbon dioxide and water, but it will produce O_3 and CO and other substances, and the consumption of technology and economy is large, waiting for be further developed. The adsorption method uses the pore size distribution and surface functional groups of activated carbon fiber (ACF) [18], activated carbon (AC) [19], and other porous adsorbents to deal with pollutants such as formaldehyde, which has the advantages of easy material availability and convenient operation. Common adsorbents include alumina and zeolite molecular sieves. Photocatalytic degradation technology uses light of a certain wavelength to irradiate photocatalyst materials to produce active species, which participate in the reaction to degrade formaldehyde into carbon dioxide and water, and so produces the effect of air purification [20].

In this paper, the adsorption mechanism and modification of activated carbon, the structure of photocatalyst TiO_2, the principle of photocatalytic reaction, and the load and modification treatment were reviewed, and the adsorption and degradation properties of activated carbon and TiO_2/AC for formaldehyde were analyzed and compared, providing scientific guidance for the degradation of formaldehyde.

Table 1: Summary of formaldehyde emission parameters for synthetic rubbers [15].

No.	A_i	T (°C)	C_i (mg·m^{-3})	C_{si} (mg·m^{-3})	EF (mg m^{-2} h^{-1})
1	0.02	60.4	0.004	0.005	NDb
2	0.557	59.3	0.269	0.320	0.801
3	0.058	60.8	0.023	0.027	0.068
4	0.019	60.7	0.003	0.004	ND
5	0.509	60.2	0.245	0.293	0.730
6	0.076	60.0	0.032	0.038	0.094
7	0.145	59.3	0.066	0.078	0.195
8	0.299	59.2	0.141	0.168	0.421
9	0.063	60.6	0.025	0.03	0.075
10	0.268	60.0	0.126	0.150	0.379
11	0.051	60.9	0.019	0.023	0.058
12	0.071	60.2	0.029	0.035	0.087
13	0.042	60.7	0.015	0.018	0.044
14	0.887	59.3	0.431	0.514	1.283
15	0.064	60.5	0.026	0.031	0.077
16	0.097	59.9	0.042	0.050	0.125
17	0.053	60.1	0.020	0.024	0.060
18	0.030	60.9	0.009	0.011	ND
19	0.826	60.8	0.401	0.480	1.199
20	0.077	60.3	0.032	0.038	0.096

2. Activated Carbon and Its Modification

2.1. Adsorption of Formaldehyde over Activated Carbon. Activated carbon has the characteristics of large specific surface area, fast adsorption rate, and moderate pore size distribution, which has significant advantages [18] in adsorption and separation of formaldehyde pollutants. According to different adsorption methods, activated carbon adsorption is divided into physical adsorption and chemical adsorption. In the physical adsorption process, the pore size gradient distribution determines the adsorption capacity and rate. The large and medium pores play the role of transporting formaldehyde molecules, and the micropores have a huge specific surface area, which can provide enough places for pollutants to stay. The adsorption of formaldehyde over activated carbon is mainly realized by electrostatic force, covalent bond dispersion force, induction force, π-electron polarization attraction, and hydrogen bond [21]. Chemical adsorption refers to the chemical reaction between the carboxyl group and phenolic hydroxyl group in the oxygen-containing functional group of activated carbon and the formaldehyde adsorbate molecule, and the adsorption is relatively stable and irreversible [22]. It can be seen from the

physical adsorption and chemical adsorption processes of activated carbon that the pore size distribution and surface functional groups of activated carbon play an extremely important role in the adsorption process of adsorbates. Therefore, scholars at home and abroad have conducted a lot of research on the adsorption of formaldehyde on activated carbon.

Tang et al. [23] studied the influence of activated carbon micropores and mesopores on the adsorption performance of formaldehyde and found that the adsorption effect of activated carbon is positively correlated with the proportion of micropores; when the specific surface area of the mesopores increases, the time to reach adsorption equilibrium is shortened. Song [24] studied the adsorption of organic pollutants on activated carbon from the perspective of pore size distribution. He proposed that a better pore gradient distribution accelerated the internal diffusion of pollutants in the pore size of activated carbon and improved the adsorption capacity.

It can be seen from the research of Song that although activated carbon micropores can provide a huge specific surface area, transport pores such as macropores and mesopores are also required. The pore size gradient affects the adsorption capacity and rate.

In addition to exploring the effect of pore size distribution of activated carbon on adsorption performance, Lin et al. [25] studied the influence of surface functional groups on adsorption performance of coconut shell and woody activated carbon through dynamic penetration experiment. The experimental results showed that the coconut shell carbon had the highest adsorption performance for formaldehyde, and they believed that the coconut shell carbon had a higher content of phenolic hydroxyl and nitrogenous functional groups on its surface. Kowalczyk et al. [26] studied the reaction mechanism between functional groups on the surface of activated carbon and formaldehyde. Formaldehyde can not only form hydrogen bonds with functional groups but also oxidize with carboxyl and phenolic hydroxyl groups in pore size.

It can be seen from the previous studies that the content of functional groups on the surface of activated carbon determines the degree of chemical adsorption and oxidation reaction, the large specific surface area of micropores provides sufficient physical adsorption sites for pollutants, and the pore size distribution affects the internal diffusion ability of formaldehyde molecules. However, activated carbon is mainly dominated by physical adsorption, which is unstable and desorbs under certain pressure and temperature conditions, causing secondary pollution. Through the redox method, the number and type of chemical functional groups on the surface of activated carbon are changed, and the physical adsorption is transformed into physical-chemical synergy adsorption, which can effectively improve the adsorption of formaldehyde molecules on the surface of activated carbon.

2.2. Activated Carbon Modification. The increase of acid oxygen-containing functional groups on the surface of activated carbon can provide more chemisorption sites for formaldehyde which is polar molecule. The acidic functional groups can attract the free π electrons on the surface of activated carbon. When the activated carbon is treated with alkali, the number of oxygen-containing functional groups increases the density of π electron cloud on the surface of activated carbon, the $\pi - \pi$ dispersion force between the activated carbon and formaldehyde is strengthened, and the adsorption property of activated carbon is improved. Researchers at home and abroad have conducted a lot of research on the modification of activated carbon functional groups.

He et al. [27] studied the effect of activated carbon modified by $KMnO_4$ on the adsorption of formaldehyde through experiments. When the concentration of $KMnO_4$ was 2%, activated carbon had the best adsorption performance for formaldehyde pollutants, and they believed that this phenomenon was attributed to the increased content of C=O and C-OH. In order to further explore the dual influence of $KMnO_4$ concentration and heat treatment temperature on the modification of activated carbon, Jiang et al. [28] treated activated carbon with different $KMnO_4$ concentrations and thermal temperatures, respectively, to explore the influence of modification on the formaldehyde adsorption performance of activated carbon samples. The study found that when the heat treatment temperature is 65°C and impregnation concentration is 0.08 mol/L, the adsorption capacity of formaldehyde molecule on modified activated carbon is the highest. However, when the concentration of $KMnO_4$ is high, the pore size of activated carbon is blocked, and the adsorption capacity decreases.

From the research of Jiang and others, it can be seen that activated carbon is impregnated with higher concentration of $KMnO_4$, and the specific surface and adsorption capacity are reduced to a certain extent, but after the reduction of $KMnO_4$, MnO_x which could decompose the adsorbates in pore channels into small molecules was generated.

The polar adsorbents can be stably adsorbed on the surface of acidic modified activated carbon because of the increase of functional group content. Liu et al. [29] explored the formaldehyde adsorption performance of activated carbon modified by phosphoric acid and activated by nitrogen. The experiment showed that the formaldehyde adsorption capacity of modified activated carbon was 4.78 mg/g when the phosphoric acid mass fraction was 40%, and the nitrogen activation temperature was 550°C. Liu et al. [30] modified activated carbon with H_2SO_4, formaldehyde saturation adsorption capacity increased by nearly 50%, and desorption peak area and peak height increased to a certain extent. It can be seen from Liu et al.'s experiment that the formaldehyde adsorption capacity of the acidified activated carbon increases, which may be attributed to the synergistic effect of physical adsorption and chemical adsorption.

In addition to oxidation modification, surface physical modification of activated carbon is mainly to increase specific surface area and adjust pore size, and its distribution by physical and chemical means to achieve the purpose of changing surface physical structure of activated carbon. The surface physical modification of activated carbon is

Table 2: Common semiconductors and band gap widths.

Semiconductors	$SrTiO_3$	TiO_2	Ta_2O_5	ZrO_2	Nb_2O_5	SnO_2	ZnO_2	ZnS	WO_3	CdS
Band gap width (eV)	3.2	3.2	4.6	5.0	3.4	3.8	3.2	3.6	2.8	3.24

firstly modified by adding some activator in the preparation process of activated carbon, and secondly, it can be physically modified by microwave radiation technology instead of traditional heating technology, so as to improve its adsorption and catalytic performance [31, 32]. Microwave modification mainly uses microwave power, radiation time, and radiation temperature to modalize the surface structure and functional group content of activated carbon, which usually interacts with N_2 and O_2 to change the surface functional group content, so as to achieve the effect of improving the adsorption and catalytic performance of activated carbon. Jones et al. [33] conducted microwave radiation on activated carbon in O_2 atmosphere and found that the surface carboxyl of oxygen-containing functional groups increased significantly, and the pore size increased significantly at higher power. Plasma modification technology is a kind of material surface modification technology developed rapidly in recent years. This technology which can produce large amounts of charged particles, excited state particles, photons, free radicals, and so on plasma in the gas medium (O_2, N_2, NH_3, and CF_4), using these high-energy plasma impacts the material surface to make the material surface physical and chemical properties change, with little damage to the material surface characteristics at the same time, so as to improve the specific surface area, pore size, pore volume, surface functional groups, and other related properties of the technology. Li et al. [34] used low-pressure nitrogen plasma to modify the surface of activated carbon, and the surface oxygen-containing acidic groups decreased with the increase of plasma power, while the nitrogen-containing basic functional groups increased accordingly.

Although the surface modification technology of activated carbon has made progress in many aspects, low cost, high performance, and simple environmental protection process are still the development direction of activated carbon modification in the future. Through the modification of activated carbon, its application has been involved in many fields, but most of it is still applied to simple adsorption process, lack of functional high-quality special activated carbon, especially as a catalyst, and catalyst carrier activated carbon. Optimizing the preparation process of activated carbon, developing activated carbon with high specific surface area and large pore volume, exploring the optimal adsorption conditions of activated carbon, reducing the consumption of resources, and improving the economic feasibility are also important research directions in the future.

2.2.1. Comment 6. Besides the activated carbon adsorption method, the photocatalytic degradation for formaldehyde by titanium dioxide is nontoxic and harmless, which has aroused the research of scholars at home and abroad.

3. Mechanism of Photocatalytic Degradation

According to the formula [35]

$$\Delta E = \frac{\hbar^2\pi^2}{2R^2}\left[\frac{1}{\mathrm{m}_e} + \frac{1}{m_h}\right] - \frac{1.8e^2}{\varepsilon R} - 0.248E_{Ry}{}^*, \qquad (2)$$

where R represents the radius of the nanocrystal, m_e represents the effective mass of the electron, m_h represents the effective mass of the hole, ε represents the dielectric constant, and $E_{Ry}{}^*$ represents the effective Rydberg energy. It can be seen from the formula that the particle radius and absorption wavelength are invertically proportional to the band gap width. In order to enable TiO_2 to respond to visible light and achieve spectral redshift, it is necessary to reduce the band gap, and the particle radius increases when the band gap decreases, which may affect the catalytic performance of TiO_2. It can be seen that this is a contradictory relationship, so the smaller the gap width is not the better. Table 2 lists the band gap widths of common semiconductors, most of semiconductor photocatalyst such as nano-ZnO and SnO_2 will undergo chemical corrosion, and the noble metals have high cost, so they are not suitable for indoor photocatalyst materials. The titanium dioxide (TiO_2) is regarded as the ideal photocatalytic degradation of the material [36, 37] of the formaldehyde and enjoys the advantage of nontoxic harmless, safe and green, and high photocatalytic efficiency.

Nano-TiO_2 is a semiconductor with a discontinuous energy band structure [38] formed by the hybridization of Ti3d and O2p orbitals, which is composed of valence band (VB), condition band (CB), and energy gap (Eg).

German physicist Hertz discovered that photoelectrons will escape from the material only when λ_{in} is greater than a certain value; otherwise, no photoelectrons will be produced regardless of the intensity of the irradiation. This is the well-known principle of photoelectric effect [39]. As shown in Figure 1 [40], electrons (e^-) preferentially fill the valence band. According to the photoelectric effect, at this time, electrons in the low-energy valence band are excited to cross the forbidden band and enter the conduction band [41]. Accordingly, holes (h^+) are formed in the valence band, and photogenerated electrons (e^-) are generated in the conduction band. After the electrons in the valence band are excited, there are two forms [42]:

(1) Some of part electrons were captured by the defect site of titanium dioxide

(2) Some of the excited photoelectrons are captured by the hole, and energy is released in the form of heat, which reduces the separation efficiency of

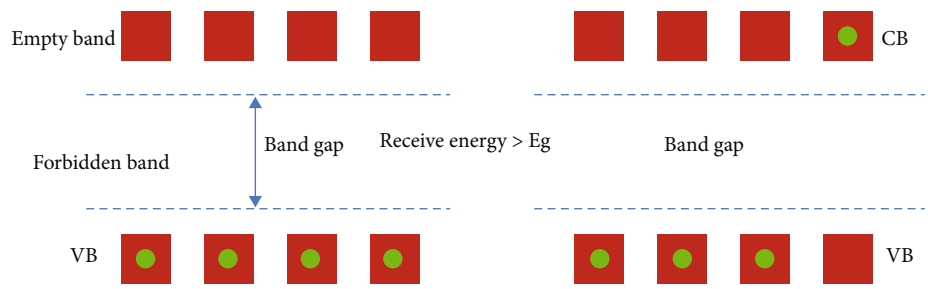

Figure 1: Energy band theory schematic.

electrons and holes, thus affecting the photocatalytic efficiency.

The photocatalytic degradation mechanism is shown in Figure 2 [43]. Photogenerated carriers migrate to different positions of the semiconductor under the action of electric field force, combine with O_2, H_2O, or OH^- on the surface of TiO_2 and react as follows, producing two active species -OH and $-O_2^-$. These substances have strong oxidation capacity, equivalent to the high temperature of 3600 K. Pollutants such as formaldehyde can be catalyzed into carbon dioxide, water, or other inorganic small molecules.

(I) The formation of electrons (e^-) and holes (h^+)

$$TiO_2 + h_v \longrightarrow TiO_2 + h^+ + e^- \tag{3}$$

(II) The formation mechanism of $-O_2^-$

$$\begin{aligned} O_2 + e^- &\longrightarrow -O_2^-, \\ Ti^{4+} + e^- &\longrightarrow Ti^{3+}, \\ O_2 + Ti^{3+} &\longrightarrow -O_2^- + Ti^{4+} \end{aligned} \tag{4}$$

(III) The formation mechanism of -OH

(1) Adsorb water molecules in the air to form

$$H_2O + h^+ \longrightarrow -OH + H^+ \tag{5}$$

(2) Formed with the aid of the intermediate H_2O_2:

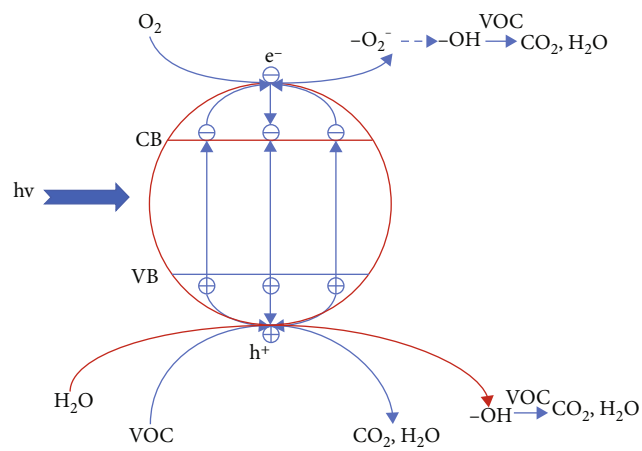

Figure 2: Photocatalytic mechanism of TiO_2.

The formation of H_2O_2 is as follows:

$$\begin{aligned} -O_2^- + H^+ &\longrightarrow -HO_2, \\ 2-HO_2 &\longrightarrow H_2O_2 + O_2, \\ -O_2^- + -HO_2 &\longrightarrow HO_2^- + O_2, \\ HO_2^- + H^+ &\longrightarrow H_2O_2 \end{aligned} \tag{6}$$

The formation of -OH is as follows:

$$\begin{aligned} H_2O_2 + e^- &\longrightarrow -OH + OH^-, \\ H_2O_2 + -O_2^- &\longrightarrow -OH + OH^- + O_2, \\ H_2O_2 + h_v &\longrightarrow 2-OH \end{aligned} \tag{7}$$

(3) Formed by reaction with OH^-:

$$h^+ + OH^- \longrightarrow -OH \tag{8}$$

(IV) Hole-electron pair recombination:

$$h^+ + e^- \longrightarrow \text{Thermal Energy}. \tag{9}$$

Yang [44] studied the intermediate species and reaction mechanism in the oxidation process of formaldehyde by physical methods such as TPD and ESR. He proposed that the reaction process of formaldehyde being oxidized into CO_2 and H_2O was as follows:

$$\begin{aligned}
&\mathrm{HCHO} + -\mathrm{OH} \cdot \mathrm{CHO} + \mathrm{H_2O},\\
&\cdot\mathrm{CHO} + -\mathrm{OH} \longrightarrow \mathrm{HCOOH},\\
&\cdot\mathrm{CHO} + -\mathrm{O_2}^- \longrightarrow \mathrm{HCO_3}^- + \mathrm{H}^+ \longrightarrow \mathrm{HCOOOH} + \mathrm{HCHO} \longrightarrow \mathrm{HCOOH},\\
&\mathrm{HCOOH} \longrightarrow \mathrm{HCOO}^- + -\mathrm{OH} \longrightarrow \mathrm{H_2O} + -\mathrm{CO_2}^-,\\
&\text{或}\mathrm{HCOO}^- + h^+ \longrightarrow \mathrm{H}^+ - \mathrm{CO_2}^-,\\
&-\mathrm{CO_2}^- + h^+ \longrightarrow \mathrm{CO_2}.
\end{aligned} \tag{10}$$

In addition to exploring the photocatalytic reaction mechanism of formaldehyde in experiments, Xie et al. [45] studied the connection relationship between reactants on the reaction potential energy plane and intermediate species at the level of 6-311++G(2df,pd) by using the B3LYP method and MP2 method of the density functional theory. Simulation shows that the intermediate is the isomer form of formic acid (HCOOH) (HOCOH).

According to the study of reaction mechanism by Yang et al., e^-, h^+, and -OH are crucial in the oxidative degradation of formaldehyde. Ishibashi et al. [46], respectively, compared the quantum yields of -OH, h^+, and photocatalysis in the reaction process, and the results showed that the yield of holes and the quantum efficiency of photocatalysis were in the same order of magnitude. In addition, the importance of holes in the photocatalytic process can be seen from the above series of reactions. Therefore, the recombination of electron-hole pairs should be inhibited as much as possible to allow more holes to participate in the reaction to form active species.

Because e^- in the valence band will recombine with h^+, be trapped by defect sites, or migrate to different positions in the semiconductor to react, the life of electron and hole is very short, only picoseconds. For example, Yang and Tamai [47] found that the trapping time of electrons was 260 fs, while the trapping time of holes was shorter, only 50 fs. Tamaki et al. [48] found that the shallow capture time of electrons is about 100 fs, the deep capture time is 150 fs, and from the shallow capture time to the deep capture time is 50 fs.

The charge transport capacity is also an important factor affecting the photocatalytic efficiency [49]. Hoffmann et al. [50] studied the UV excitation process of TiO_2 particles and other related issues. The photocatalytic reaction process and its characteristic time are shown in Table 3. The characteristic time of interfacial charge transfer is shorter than that of carrier generation, capture, and recombination. The characteristic time of interfacial charge transfer is shorter than that of carrier generation, capture, and recombination. Huang [51] believed that the recombination of photogenerated electrons and holes was much faster than charge transfer, which greatly reduced the number of photogenerated electrons and holes involved in the reaction. Therefore, effectively reducing the recombination of electrons and holes was also an important research content in the field of photocatalysis.

Table 3: Primary processes and characteristic time domains for photocatalysis on TiO_2 semiconductor.

Initial reaction step	Characteristic time
Generation of photogenerated carriers	
$TiO_2 + h_\nu \longrightarrow e^- + h_{\nu b}{}^+$	Fast (fs)
Capture of photogenerated carriers	
$h_{VB}{}^+ + >\mathrm{Ti^{IV}OH} \longrightarrow \{>\mathrm{Ti^{IV}} \cdot \mathrm{OH}\}$	Fast (10 ns)
$e_{CB}{}^- + >\mathrm{Ti^{IV}OH} \longrightarrow \{>\mathrm{Ti^{III}OH}\}$	Mild capture (100 ps)
$e_{CB}{}^- + >\mathrm{Ti^{IV}} \longrightarrow >\mathrm{Ti^{III}}$	Deep capture (10 ns)
Recombination of photogenerated carriers	
$e_{CB}{}^- + \{>\mathrm{Ti^{IV}OH}\} + \longrightarrow >\mathrm{Ti^{IV}OH}$	Slow (100 ns)
$h_{VB}{}^+ + \{>\mathrm{Ti^{III}OH}\} + \longrightarrow >\mathrm{Ti^{IV}OH}$	Fast (10 ns)
Interface charge transfer	
$\{>\mathrm{Ti^{III}OH}\}^+ + \mathrm{Red} \longrightarrow \mathrm{Ti^{IV}OH} + \mathrm{Red}$	Mild capture (100 ps)
$e_{tr}{}^- + O_x \longrightarrow \mathrm{Ti^{IV}OH} + O_x{}^-$	Very slow (ms)

4. Properties and Structure of TiO_2

The three crystal structures of nano-TiO_2 can be divided into rutile phase, anatase and brookite. The similarity between them is that they have the same basic components which is the TiO_6 octahedron structure [52]. However, the crystal structure, arrangement, connection mode, distortion degree, band gap, and defect types are different.

Anatase TiO_2 is octahedral common edge connection, while the rutile type is common edge and common fixed point connection, as shown in Figures 3 and 4 [53]. Rutile TiO_2 is a stable crystal with fewer oxygen vacancies [54]. Anatase TiO_2 has more dislocation and defects, so its distortion degree is higher than that of rutile phase, so anatase TiO_2 has excellent catalytic performance [55]. The forbidden width of anatase TiO_2 is about 3.2 eV, and that of rutile TiO_2 is about 3.0 eV [56]. The structural parameters of anatase, titanite, and rutile TiO_2 are shown in Table 4 [57], and it can be seen that their space groups, crystal cell parameters, and Ti-O bond lengths are different.

Under the calcination condition of about 600°C, anatase transforms into rutile phase through continuous bond breaking and atomic rearrangement, and the phase transition temperature is affected by the size of titanium dioxide particles and ion doping, etc. [58]. The mixed phase of anatase, plate titanium, or rutile has good catalytic performance. For example, P25 (20%rutile + 80%anatase) can be used as a standard material for photocatalytic testing because of its good catalytic performance [59].

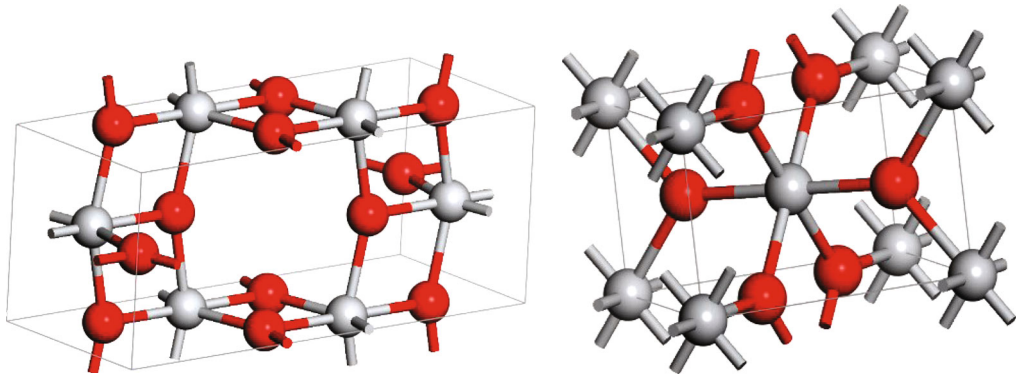

(a) (b)

Figure 3: Simulations of anatase and rutile nanosized titanium dioxide. (a) Anatase type. (b) Rutile type.

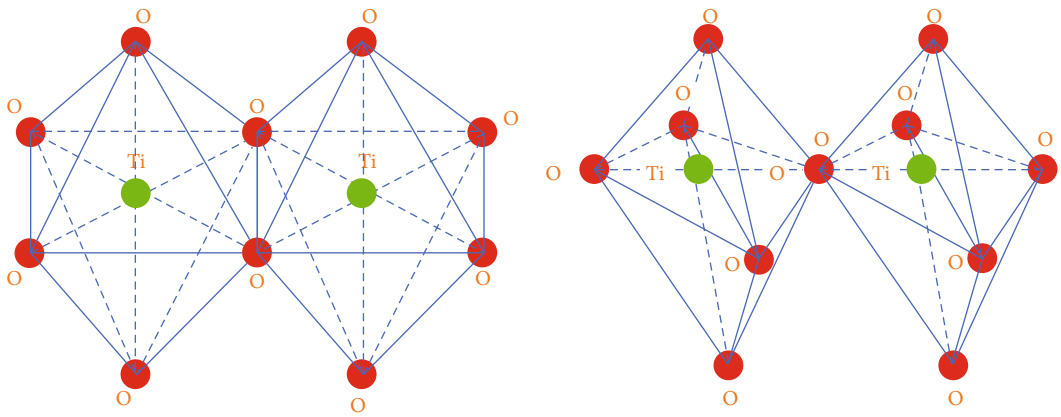

(a) (b)

Figure 4: A schematic diagram of nanosized titanium dioxide structure connection. (a) Coedge way. (b) Concurrent way.

Table 4: Crystallographic data of different TiO_2 polymorphs.

		Rutile	Anatase	Brookite
Crystal system		Tetragonal system	Tetragonal system	Orthogonal
Space group		$P4_2/mnm$ $a = b = 4.5933$	$I4_1/amd$ $a = b = 3.7842$	Pcab $a = 9.1819$
Crystal cell parameters		$c = 2.9592$	$c = 9.5139$	$b = 4.4558$ $c = 5.1429$
Ti coordination number		6	6	6
	Ti-O_1	1.988	1.946	1.87
	Ti-O_2	1.988	1.946	2.04
Ti-O band length	Ti-O_3	1.944	1.937	1.99
	Ti-O_4	1.944	1.937	1.94
	Ti-O_5	1.944	1.937	1.92
	Ti-O_6	1.944	1.937	2.00
Connection method		Common edge and common point connection	Common edge connection	

5. Modification of TiO_2

Zhu et al. [60] explored the influence of TiO_2 irradiated with different wavelengths of light on the degradation effect of formaldehyde, and the study showed that the degradation rate of formaldehyde was about 29% without UV irradiation. Titanium dioxide which is a photocatalytic material has the advantages of safety, high efficiency, energy saving, good treatment effect, and no secondary pollution, so it can degrade formaldehyde and other toxic gases or liquids. However, titanium dioxide has the following disadvantages, so it has not been applied on a large scale in industry.

The disadvantages of nanoscale titanium dioxide in the field of photocatalysis are as follows [61]:

(1) The dispersion of nanosized titanium dioxide is poor, which is prone to agglomeration. Therefore, the specific surface area and the contact area with formaldehyde molecules are reduced, affecting the photocatalytic performance

(2) The lifetime of electrons and holes is short, and the holes and electrons need to be continuously generated during the reaction process, so that they migrate to different positions in the semiconductor and participate in the reaction to produce active species

(3) TiO_2 has a low utilization rate of light.

In summary, titanium dioxide has disadvantages of small particle size, poor dispersion, high electron-hole pair recombination rate, and low utilization rate of sunlight. In order to improve its catalytic performance, researchers have conducted a lot of exploration.

5.1. Deposition of Noble Metal. Zhu et al. [62] studied the effect of Au/TiO_2 photocatalytic removal for gaseous formaldehyde, and the results showed that when the relative humidity and blue light intensity were 13% and 38.5 MW/cm^2, respectively, the degradation rate of formaldehyde under light reaction was 77%, much higher than the conversion rate under dark reaction.

The principle of action on TiO_2 modified by noble metal [63] is as follows:

(1) Since the Fermi level of TiO_2 is different from noble metals, a noble metal-TiO_2 heterojunction can be generated when noble metals are deposited on TiO_2. After the photogenerated electrons are excited by light, they will transfer from the surface of TiO_2 to the surface of noble metals. A space charge layer will be formed when the Fermi level reaches the same level. The unbalanced charge distribution causes band bending to form the Schottky barrier, as shown in Figure 5 [64]. The excited electrons in the valence band can be captured by the Schottky barrier

(2) Lattice distortion is formed when noble metals are doped into the TiO_2 crystal lattices, which hinders the recombination of electron-hole pairs to some extent and improves the photocatalytic performance of nano-TiO_2.

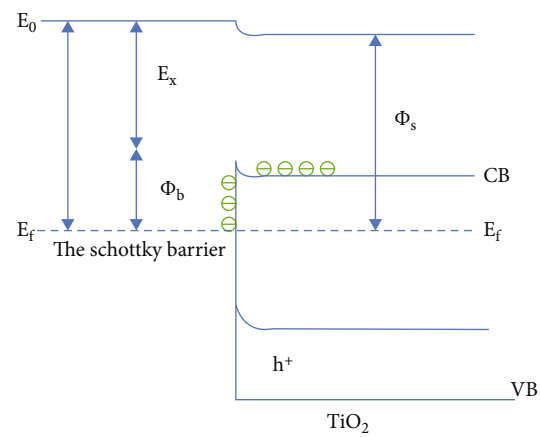

Figure 5: The schematic Schottky barrier. In the figure, Ef represents the Fermi level, VB represents valence band, CB stands for conduction band, h^+ denotes a hole. Φb is the height of the Schottky barrier, and Φs is the work function of titanium dioxide; E_x stands for built-in electric field; E_0 represents the surface potential energy of the precious metal.

When the noble metal is deposited on the surface of TiO_2, it has little shielding effect on TiO_2 and does not affect the specific surface area of TiO_2. Studies have shown that when 10% Pt is deposited on the surface of titanium dioxide, the effect on nanosized titanium dioxide is only 6%. The recombination rate of electron-hole pairs will be increased if the noble metal is deposited in a large amount of titanium dioxide. According to the study [65–68], the noble metals deposited on the surface of TiO_2 are mainly Pt and Ag. Huang et al. [69] found that Pd/TiO_2 with 0.1% load of Pd could completely degrade formaldehyde into CO_2 and H_2O at room temperature.

5.2. Surface Photosensitization. Surface photosensitization [70] is a relatively simple method, and it is one of the effective ways to broaden the absorption spectrum of TiO_2 to the visible region. There are two kinds of dye sensitization and compound sensitization.

Dye sensitization refers to the adsorption of organic dyes with an excited state potential more negative than TiO_2 on the surface of TiO_2 by physical or chemical means. After light irradiation, photogenerated electrons are generated and transferred to different positions and reacted with oxygen on the surface of TiO_2. The mechanism of action is shown in Figure 6 [71]. Studies have shown that the photocatalytic activity of TiO_2 modified by photosensitizer can be improved, and the utilization efficiency of photons can be improved by 30-80% [72]. Photosensitizers with certain stability include rosin, chlorophyll, eosin B, eosin thioneine, nori, etc. [73].

Compound sensitization uses the combination of a semiconductor with a small forbidden band width and a titanium dioxide material to form a heterojunction. According to the working principle of the heterojunction, the electrons in the

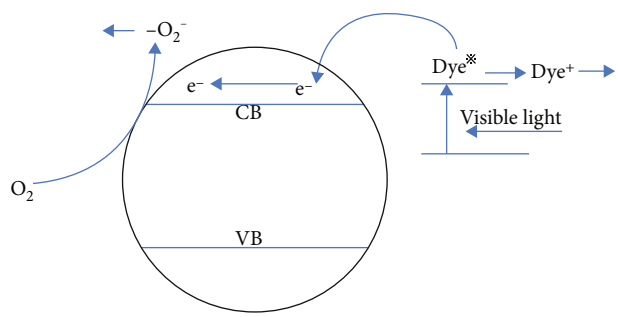

Figure 6: Mechanism of dye-sensitized titanium dioxide photocatalytic reaction.

valence band of the TiO_2 composite semiconductor are excited and transported to the TiO_2 conduction band, as shown in Figure 7 [74]. Generally, a semiconductor with a similar band structure and a narrow band gap is chosen to composite with titanium dioxide. For example, CdS-TiO_2, SnO_2-TiO_2, Fe_2O_3-TiO_2, WO_3-TiO_2, and other semiconductor composites have been applied. The synergistic effect between the matched band structure of two components can broaden the spectral response range of the composite catalyst and improve the life of photocarriers to a certain extent. The construction of heterojunction is a new research direction in the field of photocatalysis [75–78]. The band diagram of CdS-TiO_2 composite system is shown in Figure 8 [79]. The band gap of CdS is about 2.4 eV. CdS is excited first under illumination, and the photogenerated electrons are transported to the TiO_2 conduction band to achieve photogenerated carrier separation [80]. Studies have shown [81] that CdS-TiO_2 is usually used in experiments due to its good composite effect.

5.3. Metal Ion Doping. The results [82] showed that the absorption spectra of nano-TiO_2 doped with Fe^{3+} and Mn^{2+} could produce red shift and improve its photocatalytic activity. This discovery quickly led to the study of metal ion modification of pure titanium dioxide. Li [83] prepared Ag-doped TiO_2 to degrade formaldehyde and found that when the dosage of Ag/TiO_2 was 40 g, the degradation rate of formaldehyde could reach more than 93%. Kubacka et al. [84] studied the catalytic degradation of toluene by TiO_2 modified by cations (such as V, Mo, and W) and found that photocatalytic activity of TiO_2 modified by V and W is improved. Frindell et al. [85] studied the influence of doping with rare earth elements on TiO_2 and found that the spectral response range of TiO_2 was effectively broadened after modification by rare earth elements. Li et al. [86] found that TiO_2 modified by Au/Au^{3+} has a good photocatalytic ability to degrade methylene blue, because the doping of Au^{3+} can broaden the spectral response range. Researchers [87–89] found that some metal ions such as 19 kinds of Mo^{5+}, Fe^{3+}, etc. can improve the photocatalytic activity of TiO_2, while some were on the contrary, such as CO^{3+} and Al^{3+}, which would accelerate the recombination of electrons and holes to a certain extent and reduce its photocatalytic activity. Huang [90] studied the modification of titanium dioxide by doping La and Ce, and the results showed that when the doping amount of La and Ce was 1.5 wt% and 0.5 wt%, respectively, the transformation of TiO_2 from anatase to rutile phase could be greatly inhibited. Liu [91] studied the influence of doping amount of Fe^{3+} on formaldehyde degradation performance of TiO_2, and the results showed that when doped with 0.5% Fe^{3+}, formaldehyde degradation rate was up to 92.5%.

The action principle of TiO_2 doped by metal ion is as follows [92]:

(1) The position of Ti^{4+} is replaced by metal ions, causing lattice distortion. TiO_2 produces more defects to capture free electrons, which improves the photocatalytic activity to a certain extent

(2) Metal ions are doped into TiO_2, and they can be used as free electron acceptors to capture them, which hinders the recombination of carriers

(3) After doping with metal ions, TiO_2 forms an impurity level [93], which reduces the band gap width to a certain extent and widens the spectral response range.

The following conditions which can improve the photocatalytic activity of TiO_2 doped by metal ion should be met:

(1) The shallow trapping potential wells for electrons and holes are formed in TiO_2 which is doped with metal ions. For example, the energy level of Fe^{3+} is close to the valence band and conduction band of TiO_2 [94], so TiO_2 doped by Fe^{3+} forms a shallow trapping potential well, effectively capturing electrons and holes [95, 96]. In recent years, researchers have achieved outstanding results by doping [97, 98] titanium dioxide with rare earth elements. The reason is that the 5d vacant orbit of rare earth elements provides a place for electron migration

(2) Doping with metal ions similar to Ti^{4+} ion radii (74.5 pm) (for example, Fe^{3+}, Co^{3+}, Ni^{3+}, and Cr^{3+} ion radii are 69.0 pm, 68.5 pm, 70.7 pm, and 75.5 pm [99], respectively). Because metal ions with similar ionic radius are more likely to replace Ti^{4+}, the band structure of TiO_2 is changed, the shallow trapping potential well is formed, and the photocatalytic activity is improved. There is a parabolic relationship between the concentration of doped metal ions and the photocatalytic performance [100, 101], so the photocatalytic activity can be improved only by doping metal ions with appropriate concentration.

5.4. Nonmetallic Ion Doping. Studies [102, 103] have shown that N-doped nano-TiO_2 can broaden its spectral response range, which has aroused the attention of scholars at home and abroad to nonmetal ion doped TiO_2. Li [104] believed that the formaldehyde degradation rate of $TiO_{2-x}N_x$ material obtained at a solution pH of 5 and calcination temperature of 500°C could reach 70.18%, and the degradation

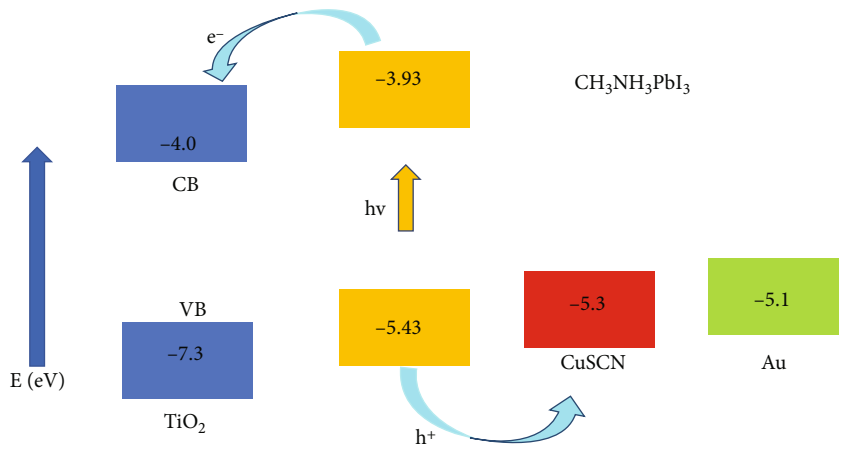

Figure 7: Schematic energy level diagram of TiO_2 and $CH_3NH_3Pb\ I_3$.

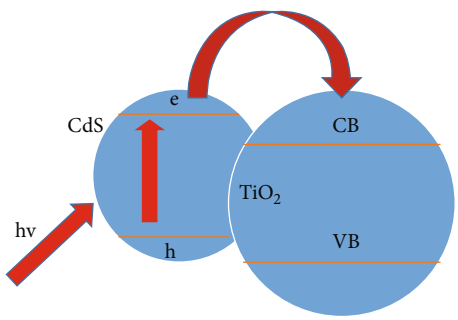

Figure 8: Energy band diagram of the CdS-TiO_2 composite system.

Table 5: The relationship between TiO_2/AC usage times and formaldehyde degradation rate.

Usage times	Formaldehyde degradation rate
1	96.54
2	96.06
3	96.74
4	94.82
5	93.85
6	92.72

reaction complied with first-order kinetics. Liu et al. [105] used the sol-gel method to prepare the nitrogen-doped TiO_2 film to degrade formaldehyde. The study showed that the degradation rate of formaldehyde reached 90% within 24 h, and it had excellent stability and reusability. Wang et al. [106] believe that TiO_2 is doped with nitrogen, and the N2p state near the valence band is the reason for improving catalytic performance. Palgrave et al. [107] studied the band gap width of titanium dioxide after nitrogen doping, and he believed that there was a correlation between the diffusion path and chemical state of nitrogen atom doping and TiO_2 band gap. Tompsett et al. [108] modified titanium dioxide by nitrogen atoms and found that nanotitanium dioxide had good photocatalytic degradation performance under the light condition of 440 nm wavelength. Zhang et al. [109] studied the photocatalytic performance of the TiO_2 product calcined in NH_3 and then calcined in H_2. They found that the synergistic effect of oxygen vacancies and N impurities can improve the efficiency of degrading pollutants.

The action principle of TiO_2 doped by nonmetallic ion is as follows:

(1) When the oxygen position of TiO_2 is replaced by nonmetallic anions, which can change the distortion of the TiO_2 structure and reduce the recombination of electron-hole pairs to a certain extent, more electrons and holes can participate in the reaction [110]

(2) The hybridization of O orbital with nonmetallic ions (such as N^{3-} and C^{4-}) causes the conduction band of TiO_2 to shift down, which reduces the band gap width of TiO_2 and widens the spectral response range

(3) Nonmetallic anions enter the titanium dioxide lattice to replace the interstitial sites, forming a deep impurity level. On the one hand, the spectral response range is broadened; on the other hand, at the deep impurity level, electrons and holes will recombine. It has been proven that it is very important to solve this competitive relationship for improving the photocatalytic activity. N^{3-}, P^{3-}, C^{4-}, and S^{2-} are common nonmetallic anions which doped into titanium dioxide, among which N^{3-} [111] has the best doping effect.

In summary, the main methods to broaden the spectral response range of nano-TiO_2 and improve its photocatalytic performance include noble metal deposition, surface photosensitization, metal ion doping, nonmetal ion doping, etc.

6. TiO_2 Loaded on Activated Carbon

Studies at home and abroad have found that nano-TiO_2 supported on the carrier (such as silicon dioxide and activated carbon) to prepare TiO_2/AC composite material can

Table 6: Some previous studies on adsorption and photocatalysis.

Type	Researchers	Degradation effect of formaldehyde	Experimental inquiry factor
Adsorption	Lin et al. [25]	Coconut shell carbon has the highest adsorption performance for formaldehyde.	Explore the effect of activated carbon pore size distribution on adsorption performance.
	Liu et al. [60]	The adsorption capacity of modified activated carbon to formaldehyde is 4.78 mg/g.	The adsorption performance of formaldehyde on phosphoric acid modified and nitrogen activated carbon was studied.
	Liu et al. [62]	The saturated adsorption capacity of formaldehyde increased by nearly 50%.	H_2SO_4 modified activated carbon was investigated.
Photocatalytic	Zhu et al. [60]	The degradation rate of formaldehyde is about 29% without UV irradiation.	Explore the influence of different wavelengths of light irradiation TiO_2 on formaldehyde degradation.
	Zhu et al. [62]	When the relative humidity and blue light intensity were 13% and 38.5 mW/cm^2, the degradation rate of formaldehyde was 77%.	The effect of Au/TiO_2 photocatalytic removal of formaldehyde in gas phase was studied.
	Liu et al. [105]	Formaldehyde degradation rate reached 90% within 24 h and has excellent stability.	TiO_2 thin films doped with nitrogen were prepared by the sol-gel method.
	Sun et al. [115]	The adsorption capacity of TiO_2/ACF is 60 mg/g, which is much higher than that of activated carbon alone.	The degradation effect of TiO_2/ACF adsorptive catalyst on formaldehyde was studied.
	Li et al. [122]	When the TiO_2/AC material was used for six times continuously, the formaldehyde degradation rate still reached 92%.	The reusability of the adsorption-catalyzed comaterial was studied.

effectively solve the problem of difficult recovery of titanium dioxide powder and increase the photocatalytic activity of TiO_2. Activated carbon can increase the local concentration around the catalyst, increase the contact area between pollutants and titanium dioxide, and completely degrade the intermediate products [112].

Huang et al. [113] studied the layer-by-layer deposition of photocatalyst TiO_2 and activated carbon on electrospun fibers by electrospray and obtained the NF-P/C multilayer composite film. It was found that the reason why the composite film has a larger contact area with air pollutants is because the electrospun nanofibers with a large specific surface area serve as the carrier of the photocatalyst. At the same time, it is more convenient to access and prevent the powder from scattering. Wu [114] prepared ACF/photocatalyst-free composite materials, which combined adsorption and catalysis to accelerate the degradation of indoor pollutants such as formaldehyde. Sun et al. [115] studied the degradation effect of TiO_2/ACF adsorption catalyst materials on formaldehyde, and the results showed that the degradation rate of synergistic materials to formaldehyde can reach 94.06%, and the adsorption capacity of activated carbon for formaldehyde is 60 mg/g, which is much higher than that of the single activated carbon.

From the study on the degradation of formaldehyde by the adsorption-catalytic synergistic material prepared by Wu et al., it can be seen that the degradation rate of HCHO can be greatly increased after the adsorption-mass transfer-degradation process. While the supporting body provides a reaction environment for the catalyst, the AC can be regenerated in situ.

Chen et al. [116] explored the effect of the pore structure and specific surface area of activated carbon on the catalytic performance of the adsorption-catalytic synergistic material, and the results showed that the photocatalytic activity of the synergistic material increased with the increase of the average pore size and specific surface area of the activated carbon. At the same time, Lu et al. [117] used the sol-gel method to support activated carbon with different pore sizes and specific surface areas on titanium dioxide to degrade toluene, the degradation rate of titanium dioxide supported by activated carbon with large specific surface area could reach 97%, and the deactivation time of catalyst was significantly delayed.

It can be seen from the research of Chen and others that the specific surface area and pore size of activated carbon have a significant impact on the catalytic degradation performance of the adsorption-catalytic synergistic material. Activated carbon with mesopores and macropores supported titanium dioxide can significantly improve the photocatalytic performance.

Luo et al. [118] studied the dispersibility of TiO_2 in synergistic materials, and they found that titanium dioxide has excellent dispersibility, with an average particle size of about 40 nm, and the catalyst active sites are evenly distributed, so the synergistic performance is significantly improved. Wang [119] studied the dispersibility of titanium dioxide on the surface of TiO_2/AC materials through an electron microscopy. They found that titanium dioxide is more uniformly supported on the surface of activated carbon, but there are also a small part of titanium dioxide agglomerated particles, which they believe the particles can reduce the free energy of the system through agglomeration to improve the load stability. Xing et al. [120] effectively controlled the agglomeration of catalyst particles by controlling the times of supporting TiO_2 on the surface of activated carbon.

Ma and Li [121] explored the influence of nano-TiO_2 loading amount on the degradation of formaldehyde by wood-based activated carbon/TiO_2 composite materials. The study showed that the degradation rate of formaldehyde first increased and then decreased with the increase of nano-TiO_2 loading amount. Li et al. [122] found that when the titanium dioxide loading concentration on the surface of activated carbon increased, the light transmittance would decrease, so the degradation rate of formaldehyde would decrease. At the same time, she also studied the repeated practicability of adsorption-catalytic synergistic materials. As shown in Table 5, when the TiO_2/AC material was used for six times continuously, the degradation rate of formaldehyde still reached 92%.

Hu and Deng [123] studied the position of titanium dioxide loaded in the pore size of activated carbon by scanning electron microscopy. By comparing the electron micrographs of the activated carbon surface before and after loading, they found that when the catalyst loading reaches a certain threshold, the transition pores of activated carbon would be blocked, thus affecting the adsorption performance.

According to Hu and Deng's research on the effect of titanium dioxide loading on the degradation of adsorbates, when the loading amount reaches a certain threshold, TiO_2 will block the macropores and mesopores of activated carbon, affecting the migration rate of pollutants and thus reducing the degradation efficiency. Therefore, the composite ratio of adsorbent and catalyst should be adjusted to achieve the best catalytic degradation activity.

Table 6 lists some previous research results. It can be seen that compared with conventional formaldehyde degradation system, TiO_2/AC has significantly improved formaldehyde degradation effect.

7. Conclusions and Outlook

According to the different adsorption modes, activated carbon adsorption can be divided into physical adsorption and chemical adsorption. Better pore gradient distribution speeds up the internal diffusion of formaldehyde in the aperture of activated carbon, improves the physical adsorption capacity, and increases the number of acidic oxygen-containing functional groups on the surface of activated carbon is conducive to improving the chemical adsorption of formaldehyde polar molecules. TiO_2/AC adsorption and catalytic comaterial prepared by TiO_2 supported on activated carbon is conducive to solving the problem of difficult recycling of catalyst. Through the absorption and concentration of formaldehyde by activated carbon, it provides a good reaction environment for photocatalysis and improves the degradation rate. In the preparation process, metal ion/non-metal ion doping modification, on the one hand, can effectively broaden the spectral response range and, on the other hand, to a certain extent, inhibits the recombination of electrons and holes. If modified TiO_2 is loaded on the surface of activated carbon, the adsorption synergistic material will have great advantages in adsorption catalysis.

With the in-depth study of TiO_2 mechanism, TiO_2/AC materials with high removal efficiency, large adsorption capacity, low energy consumption, and selectivity will be prepared to improve the preparation level of adsorption-catalytic comaterials, and TiO_2/AC materials will have broader application prospects.

Conflicts of Interest

The authors declared no potential conflicts of interest with respect to the research, authorship, and/or publication of this article.

Acknowledgments

The present work was supported by the National Natural Science Foundation of China (51906193) and the Basic Research Program of Natural Science in Shaanxi Province (2020JQ-039).

References

[1] Z. ML, W. JH, and W. XD, "Study on adsorption of formaldehyde in air by different bentonites," *New Building Material*, vol. 44, no. 7, p. 27, 2007.

[2] L. Liu, X. Yu, X. Dong, Q. Wang, Y. Wang, and J. Huang, "The research on formaldehyde concentration distribution in new decorated residential buildings," *Procedia Engineering*, vol. 205, pp. 1535–1541, 2017.

[3] W. P. Qin, C. L. Miao, X. H. Wang, and C. Y. Gao, "Harm of formaldehyde in daily chemicals and research progress in its analysis," *Detergent & Cosmetics*, vol. 13, pp. 4–6, 2016.

[4] L. Huang, J. Mo, J. Sundell, Z. Fan, and Y. Zhang, "Health risk assessment of inhalation exposure to Formaldehyde and benzene in newly remodeled Buildings, Beijing," *PLoS One*, vol. 8, no. 11, article e79553, 2013.

[5] R. Kostianen, "Volatile organic compounds in the indoor air of normal and sick houses," *Atomspheric Environment*, vol. 29, no. 6, pp. 693–702, 1995.

[6] G. Liqun and G. Yanqun, "Study on building materials and indoor pollution," *Procedia Engineering*, vol. 21, pp. 789–794, 2011.

[7] X. Y. Zhang, B. Gao, A. E. Creamer, C. Cao, and Y. Li, "Adsorption of VOCs onto engineered carbon materials: a review," *Journal of Hazardous Materials*, vol. 338, no. 15, pp. 102–123, 2017.

[8] T. Salthammer, S. Mentese, and R. Marutzky, "Formaldehyde in the indoor environment," *Chemical Reviews*, vol. 110, no. 4, pp. 2536–2572, 2010.

[9] M. M. Loh, J. I. Levy, J. D. Spengler, E. A. Houseman, and D. H. Bennett, "Ranking cancer risks of organic hazardous air pollutants in the United States," *Environmental Health Perspectives*, vol. 115, no. 8, pp. 1160–1168, 2007.

[10] J. Ye, X. F. Zhu, B. Cheng, J. Yu, and C. Jiang, "Few-Layered Graphene-like boron nitride: a highly efficient adsorbent for indoor formaldehyde removal," *Environmental Science & Technology Letters*, vol. 4, no. 1, pp. 20–25, 2017.

[11] Q. M. Hu, "Research on indoor air purification technology and its evaluation method," *Shandong Industrial Technology*, vol. 11, pp. 101-102, 2019.

[12] J. J. Schauer, M. J. Kleeman, G. R. Cass, and B. R. T. Simoneit, "Measurement of emissions from air pollution Sources. 4. C1 –C27Organic compounds from cooking with seed oils," *Environmental Science & Technology*, vol. 36, no. 4, pp. 567–575, 2002.

[13] J. J. Schauer, M. J. Kleeman, G. Cass, and B. R. T. Simoneit, "Measurement of emissions from air pollution Sources. 1. C1through C29Organic compounds from meat charbroiling," *Science & Technology*, vol. 33, no. 10, pp. 1566–1577, 1999.

[14] Y. Zhao, C. Chen, and B. Zhao, "Is oil temperature a key factor influencing air pollutant emissions from Chinese cooking?," *Atmospheric Environment*, vol. 193, pp. 190–197, 2018.

[15] J. H. Hu, H. Z. Yao, H. Z. Xu, Z. Ni, B. Dong, and R. Yuan, "Investigation of the characteristics of gaseous formaldehyde emission from synthetic rubbers assisted by S-TiO2catalyst," *Earth and Environmental Science*, vol. 675, no. 1, pp. 012194–012197, 2021.

[16] J. X. Zhong, W. Li, and H. P. Hou, "Formaldehyde removal by potted plant-soil systems," *Journal of Hazardous Materials*, vol. 192, no. 1, pp. 314–318, 2011.

[17] M. B. Chang and C. C. Lee, "Destruction of formaldehyde with dielectric barrier discharge plasmas," *Environmental Science & Technology*, vol. 29, no. 1, pp. 181–186, 1995.

[18] S. Suresh and T. J. Bandosz, "Removal of formaldehyde on carbon -based materials: A review of the recent approaches and findings," *Carbon*, vol. 137, no. 1, pp. 207–221, 2018.

[19] C. Ma, X. Li, and T. Zhu, "Removal of low-concentration formaldehyde in air by adsorption on activated carbon modified by hexamethylene diamine," *Carbon*, vol. 49, no. 8, pp. 2873–2875, 2011.

[20] B. Liu, X. Zhao, J. Yu, I. P. Parkin, A. Fujishima, and K. Nakata, "Intrinsic intermediate gap states of TiO_2 materials and their roles in charge carrier kinetics," *Journal of Photo-chemistry and Photobiology C: Photochemistry Reviews*, vol. 39, pp. 1–57, 2019.

[21] Q. Li, "Study on the effect of modified activated carbon on adsorption and removal of gaseous pollutants formaldehyde and ammonia," *Liaoning Chemical Industry*, vol. 50, no. 7, p. 2, 2021.

[22] B. C. Liu and X. M. Zhao, "Research progress on removal of indoor formaldehyde by activated carbon adsorption," *Journal of Chengdu Textile College*, vol. 34, no. 1, pp. 2-3, 2017.

[23] J. H. Tang, X. Z. Liang, D. H. Long, X. J. Liu, and L. C. Ling, "Effect of pore structure and surface functional group on formaldehyde adsorption performance of activated carbon," *Carbon*, vol. 26, no. 3, pp. 21–25, 2007.

[24] J. F. Song, *VOCs absorption by activated carbon and its structure-activity relationship*, Central South University, 2014.

[25] L. L. Lin, Z. F. Qiu, X. L. Han, C. L. Ye, and Y. L. Liu, "Selection of activated carbon for adsorption of gas phase formaldehyde," *Environmental Pollution and Prevention*, vol. 35, no. 12, pp. 19–25, 2013.

[26] P. Kowalczyk, J. Miyawaki, Y. Azuma et al., "Molecular simulation aided nanoporous carbon design for highly efficient low- concentrated formaldehyde capture," *Carbon*, vol. 124, pp. 152–160, 2017.

[27] M. He, L. Yuan, K. Q. Qu, Y. H. Zhang, and S. X. Liu, "Study on formaldehyde adsorption performance of activated carbon modified by potassium permanganate," *Guangzhou Chemical Industry*, vol. 45, no. 14, p. 3, 2017.

[28] L. Y. Jiang, S. X. Zhou, W. Z. Wang, J. Q. Wu, and G. J. Lu, "Activated carbon loaded manganese oxide for formaldehyde adsorption," *Journal of Environmental Sciences*, vol. 2, pp. 337–341, 2008.

[29] X. M. Liu, J. W. Chen, K. X. Chen, and X. M. Song, "Adsorption of formaldehyde on activated carbon from camellia shell modified by phosphoric acid," *Applied Chemical Industry*, vol. 47, no. 4, pp. 679–683, 2018.

[30] Y. Y. Liu, C. W. Zhou, T. Y. Hou, L. Shi, and X. F. Li, "Study on formaldehyde adsorption performance of H_2O_2/H_2SO_4 modified activated carbon from corn stalk," *Hubei Agricultural Sciences*, vol. 19, pp. 4584–4586, 2014.

[31] L. Q. Li, S. Liu, X. Liang, and Z. Liu, "Adsorption of 1, 2-dichloroethane on activated carbon modified by microwave," *Journal of Hunan University*, vol. 42, no. 6, pp. 90–95, 2015.

[32] Z. G. Xie and C. L. Liu, "Application of microwave irradiation technology in the preparation of activated carbon," *Guangzhou Chemistry*, vol. 31, no. 2, pp. 66–70, 2006.

[33] D. A. Jones, T. P. Lelyveld, S. D. Mavrofidis, S. W. Kingman, and N. J. Miles, "Microwave heating applications in environmental engineering–a review," *Resources Conservation and Recycling*, vol. 34, no. 2, pp. 75–90, 2002.

[34] L. T. Li, Q. Xie, J. Li, X. L. Zhang, and J. Zhang, "Surface modification of activated carbon by low-pressure nitrogen plasma," *Proceedings of national Activated Carbon Symposium*, vol. 2004, pp. 357–363, 2004.

[35] L. Zeng, "Study on preparation and mechanism of nano-TiO2 photocatalyst for strong degradation of VOC," Huazhong University of Science and Technology, Wuhan, 2015.

[36] Z. Zhang, J. Zhang, S. H. Li, G. X. Zhang, and Y. L. Zhao, "Research progress of TiO_2 photocatalyst and its application in environment," *Chemistry and Bonding*, vol. 39, no. 2, p. 135, 2017.

[37] H. N. Chen, Nanayakkara, and V. H. Grassian, "Titanium dioxide photocatalysis in atmospheric chemistry," *Chemical Reviews*, vol. 112, no. 11, pp. 5919–5948, 2012.

[38] J. J. Zhao and J. Cheng, "Theoretical study on electronic band structure of anatase TiO2(101) surface," *Journal of Electrochemistry*, vol. 1, pp. 45–52, 2017.

[39] L. L. Huo, S. Y. Meng, and X. Q. Yang, "Experimental analysis of photoelectric effect," *Physical Experiment*, vol. 21, no. 2, p. 1, 2001.

[40] Q. S. Shi, G. W. Wang, Z. Cheng et al., *Principle and current situation of photocatalyst technology*, Shanghai Aircraft Design and Research Institute, Shanghai, 2012.

[41] D. Kong, *Study on TiO2 Nanorods Modified by Metal Nanoparticles and their Application in Photocatalytic Reduction of CO2*, Zhejiang University, Nanjing, 2014.

[42] Y. K. Liu, *Analysis on the photocatalyst and catalytic oxidation mechanism of nano titania modified by metal ions doped on activated carbon*, Shandong Jianzhu University, Jinan, 2018.

[43] L. Zeng, *Study on preparation and mechanism of nano-TiO2 photocatalyst for strong degradation of VOC*, Huazhong University of Science and Technology, Wuhan, 2015.

[44] J. J. Yang, "Reaction mechanism of photocatalytic oxidation of formaldehyde," *Journal of Physicochemical*, vol. 17, no. 3, pp. 278–281, 2001.

[45] P. T. Xie, C. Q. Li, and H. M. Bi, "Theoreticalstudy on photocatalytic oxidation mechanism of formaldehyde," *Journal of Hebei Normal University*, vol. 42, no. 4, pp. 4-5, 2018.

[46] K. Ishibashi, A. Fujishima, T. Watanabe, and K. Hashimoto, "Quantum yields of active oxidative species formed on TiO_2 photocatalyst," *Journal of Photochemistry and Photobiology A-chemistry*, vol. 134, no. 1-2, pp. 139–142, 2000.

[47] X. Yang and N. Tamai, "How fast is interfacial hole transfer? In situ monitoring of carrier dynamics in anatase TiO_2 nanoparticles by femtosecond laser spectroscopy," *Physical Chemistry Chemical Physics*, vol. 3, no. 16, pp. 3393–3398, 2001.

[48] Y. Tamaki, A. Furube, M. Murai, K. Hara, R. Katoh, and M. Tachiya, "Dynamics of efficient electron–hole separation in TiO2nanoparticles revealed by femtosecond transient absorption spectroscopy under the weak-excitation condition," *Physical Chemistry Chemical Physics*, vol. 9, no. 12, pp. 1453–1460, 2007.

[49] M. Y. Li, *Study on the mechanism and properties of black titanium dioxide for enhancing visible light absorption and photocatalytic efficiency*, Lanzhou University, Lanzhou, 2013.

[50] M. R. Hoffmann, S. T. Martin, W. Y. Choi, and D. W. Bahnemann, "Environmental Applications of semiconductor photocatalysis," *Chemical Reviews*, vol. 95, no. 1, pp. 69–96, 1995.

[51] X. J. Huang, *Preparation and doping modification of TiO_2 photocatalyst*, Hunan University, Changsha, 2015.

[52] L. Zeng, *Study on Preparation and Mechanism of Nano-TiO2 Photocatalyst for Strong Degradation of VOC*, Huazhong University of Science and Technology, Wuhan, 2015.

[53] Y. K. Liu, *Analysis on the photocatalyst and catalytic oxidation mechanism of nano titania modified by metal ions doped on activated carbon*, Shandong Jianzhu University, Jinan, 2018.

[54] M. Y. Li, *Study on the mechanism and properties of black titanium dioxide for enhancing visible light absorption and photocatalytic efficiency*, Lanzhou University, Lanzhou, 2013.

[55] R. Ma, *Study on Photocatalytic Reforming of Anatase-Rutile Mission-Phase TiO_2 for Biological Hydrogen Production*, Dalian Ocean University, DA Lian, 2019.

[56] X. Zhang, Y. Lin, D. He, J. Zhang, Z. Fan, and T. Xie, "Interface junction at anatase/rutile in mixed-phase TiO_2: Formation and photo-generated charge carriers properties," *Chemical Physics Letters*, vol. 504, no. 1-3, pp. 71–75, 2011.

[57] L. Zeng, *Study on Preparation and Mechanism of Nano-TiO2 Photocatalyst for Strong Degradation of VOC*, Huazhong University of Science and Technology, Wuhan, 2015.

[58] S. Bakardjieva and J. Subrt, "Photoactivity of anatase-rutile TiO_2 nanocrystalline mixtures obtained by heat treatment of homogeneously precipitated anatase," *Applied Catalysis B: Environmental*, vol. 1, pp. 193–202, 2005.

[59] C. H. Wang, C. L. Shao, X. T. Zhang, and Y. Liu, "SnO2Nanostructures-TiO2Nanofibers heterostructures: controlled fabrication and High Photocatalytic properties," *Inorganic Chemistry*, vol. 48, no. 15, pp. 7261–7268, 2009.

[60] Q. Zhu, L. N. Liu, C. X. Huang, M. J. Feng, and Z. F. Peng, "Photocatalytic degradation of formaldehyde by TiO_2," *Guangzhou Chemical Industry*, vol. 49, no. 10, pp. 2-3, 2021.

[61] N. Li, W. Zhang, and G. X. Li, "Research progress of TiO_2 photocatalyst," *Fine Chemicals*, vol. 38, pp. 5-6, 2021.

[62] X. B. Zhu, C. Jin, X. S. Li, J. L. Liu, and C. Y. Liu, "Performance kinetics of Au/TiO_2 photocatalytic oxidation of formaldehyde under LED visible light," *Journal of Chemical Industry*, vol. 68, no. SI, pp. 196–203, 2017.

[63] L. Y. Wang, *Effects of β radioactivity and precious metals on photocatalytic properties of Titanium dioxide*, East China University of Technology, Nanchang, 2018.

[64] Y. Wei, *Study on preparation, photocatalytic properties and formation mechanism of titanium dioxide*, Jilin University, Changchun, 2018.

[65] Z. Liu, B. Guo, L. Hong, and H. Jiang, "Physicochemical and photocatalytic characterizations of TiO_2/Pt nanocomposites," *Journal of Photochemistry & Photobiology A-Chemistry*, vol. 172, no. 1, pp. 81–88, 2005.

[66] F. Lin, D. E. Wang, Z. X. Jiang et al., "Photocatalytic oxidation of thiophene on BiVO4with dual co-catalysts Pt and RuO2under visible light irradiation using molecular oxygen as oxidant," *Energy & Environmental Science*, vol. 5, no. 4, pp. 6400–6406, 2012.

[67] D. S. Deng, Y. Yang, Y. Gong, Y. Li, X. Xu, and Y. Wang, "Palladium nanoparticles supported on mpg-C3N4 as active catalyst for semihydrogenation of phenylacetylene under mild conditions," *Green Chemistry*, vol. 15, no. 9, pp. 2525–2531, 2013.

[68] X. M. Zhao, L. X. Cao, R. J. Gao, G. Su, and W. Liu, "Preparation and photocatalytic properties of silver-deposited titanium dioxide nanostructures by ion exchange method," *Journal of Artificial Crystals*, vol. 43, no. 9, pp. 2171–2177, 2014.

[69] H. B. Huang, X. G. Ye, H. Huang, L. Zhang, and D. Y. C. Leung, "Mechanistic study on formaldehyde removal over Pd/TiO_2 catalysts: oxygen transfer and role of water vapor," *Chemical Engineering Journal*, vol. 230, pp. 73–79, 2013.

[70] S. M. A. Hossain, M. E. Ali, and S. B. Abd Hamid, "Synergizing TiO₂ surface to enhance photocatalysis: a green technology for clean and Safe Environment - A review," *Advanced Materials Research*, vol. 1109, pp. 300–303, 2015.

[71] H. Li, *The preparation of TiO_2 film and its photocatalytic degradation of organic pollutants*, Jinan University, Jinan, 2015.

[72] C. Y. Yang, W. L. Wang, W. P. Dong, and L. M. Wu, "et alPreparation and photocatalytic performance of novel TiO_2 nanoparticles modified by poly (2-aminobenzenesulfonic acid)," *Journal of Composite Materials*, vol. 33, no. 9, pp. 2132–2140, 2016.

[73] Y. K. Liu, *Analysis on the photocatalyst and catalytic oxidation mechanism of nano-titania modified by metal ions doped on activated carbon*, Shandong Jianzhu University, Jinan, 2018.

[74] N. G. Papk, "Perovskite solar cells: An emerging photovoltaic technology," *Materials Today*, vol. 18, no. 2, pp. 65–72, 2015.

[75] J. G. Yu, S. H. Wang, J. X. Low, and W. Xiao, "Enhanced photocatalytic performance of direct Z-scheme g-C_3N_4-TiO_2 photocatalysts for the decomposition of formaldehyde in air," *Journal of Physical Chemistry*, vol. 15, no. 39, pp. 16883–16890, 2013.

[76] Y. J. Li, T. P. Cao, C. L. Shao, and C. H. Wang, "Preparation and Photocatalytic Properties of γ-Bi_2O_3/TiO_2 Composite Fibers," *Inorganic Materials*, vol. 27, no. 7, pp. 687–692, 2012.

[77] Z. W. Mei, S. X. Ouyang, D. M. Tang, T. Kako, D. Golberg, and J. Ye, "An ion-exchange route for the synthesis of hierarchical In_2S_3/$ZnIn_2S_4$ bulk composite and its photocatalytic activity under visible-light irradiation," *Dalton Transactions*, vol. 42, no. 8, pp. 2687–2690, 2013.

[78] D. L. Jiang, L. L. Chen, I. M. Xie, and M. Chen, "Ag2S/g-C3N4composite photocatalysts for efficient Pt-free hydrogen production. The co-catalyst function of Ag/Ag_2S formed by simultaneous photodeposition," *Dalton Transactions*, vol. 43, no. 12, pp. 4878–4885, 2014.

[79] D. R. Baker and P. V. Kamat, "Photosensitization of TiO2Nanostructures with Cds Quantum Dots: particulate versus tubular support architectures," *Advanced Functional Materials*, vol. 19, no. 5, pp. 805–811, 2009.

[80] P. Y. Zhang, G. Yu, and Z. P. Jiang, "Progress of semiconductor photocatalyst and its modification technology," *Progress in Environmental Science*, vol. 5, no. 3, pp. 1–10, 1997.

[81] J. J. Du, J. W. Zhao, X. M. Cheng, and K. S. Wang, "Preparation and photocatalytic performance of CdS/TiO_2 nanotube arrays," *Journal of Artificial Crystals*, vol. 45, no. 2, pp. 535–539, 2016.

[82] S. Tieng, A. Kanaev, and K. Chhor, "New homogeneously doped Fe(III)-TiO_2 photocatalyst for gaseous pollutant degradation," *Applied Catalyis A-General*, vol. 399, no. 1-2, pp. 191–197, 2011.

[83] H. F. Li, *Study on the treatment of indoor formaldehyde by TiO_2 photocatalytic technology*, Henan University of Technology, Zhengzhou, 2018.

[84] A. Kubacka, G. Colón, and M. Fernández-García, "Cationic (V, Mo, Nb, W) doping of TiO_2-anatase: A real alternative for visible light-driven photocatalysts," *Catalysis Today*, vol. 143, no. 3-4, pp. 286–292, 2009.

[85] Frindell, M. H. Bartl, M. R. Robinson, G. C. Bazan, A. Popitsch, and G. D. Stucky, "Visible and near-IR luminescence via energy transfer in rare earth doped mesoporous titania thin films with nanocrystalline walls," *Journal of Solid State Chemistry*, vol. 172, no. 1, pp. 81–88, 2003.

[86] X. Z. Li and F. B. Li, "Study of Au/Au3+-TiO2Photocatalysts toward visible Photooxidation for water and wastewater treatment," *Environmental Science & Technology*, vol. 35, no. 11, pp. 2381–2387, 2001.

[87] A. Y. Choi and C. H. Han, "Comparison of doping limits among sonochemically prepared metal-doped TiO_2 nanopowders in view of physicochemical properties," *Research on Chemical Intermediates*, vol. 39, no. 4, pp. 1563–1569, 2013.

[88] C. J. Hao, J. Li, Z. L. Zhang et al., "Enhancement of photocatalytic properties of TiO_2 nanoparticles doped with CeO_2 and supported on SiO_2 for phenol degradation," *Applied Surface Science*, vol. 331, pp. 17–26, 2015.

[89] Q. Q. Chen, H. Q. Xie, W. Zhou, J. F. Chen, and H. Huang, "Visible photocatalytic degradation of phenol by cerium doped nano-titanium dioxide," *Chemical Progress*, vol. 31, no. 5, pp. 1043–1046, 2012.

[90] X. J. Huang, *Preparation and doping modification of TiO_2 photocatalyst*, Hunan University, Changsha, 2015.

[91] Y. K. Liu, *Analysis on the photocatalyst and catalytic oxidation mechanism of nano titania modified by metal ions doped on activated carbon*, Shandong Jianzhu University, Jinan, 2018.

[92] W. L. Lin, "Improvement of photodegradation of titanium dioxide by metal doping," *Shandong Chemical Industry*, vol. 45, no. 7, pp. 10–12, 2016.

[93] M. Y. Li, *Study on the mechanism and properties of black titanium dioxide for enhancing visible light absorption and photocatalytic efficiency*, Lanzhou University, Lanzhou, 2013.

[94] L. Zeng, *Study on preparation and mechanism of nano-TiO_2 photocatalyst for strong degradation of VOC*, Huazhong University of Science and Technology, Wuhan, 2015.

[95] M. Zhou, J. Yu, and B. Cheng, "Effects of Fe-doping on the photocatalytic activity of mesoporous TiO_2 powders prepared by an ultrasonic method," *Journal of Hazardous Materials*, vol. 137, no. 3, pp. 1838–1847, 2006.

[96] X. H. Wang, J. G. Li, H. Kamiyama, Y. Moriyoshi, and T. Ishigaki, "Wavelength-sensitive photocatalytic degradation of methyl orange in aqueous suspension over iron(III)-doped TiO2Nanopowders under UV and visible light irradiation," *Journal of Physical Chemistry B*, vol. 110, no. 13, pp. 6804–6809, 2006.

[97] K. T. Ranjit, I. Willner, S. H. Bossmann, and A. M. Braun, "Lanthanide Oxide Doped Titanium Dioxide Photocatalysts: Effective Photocatalysts for the Enhanced Degradation of Salicylic Acid and _t_ -Cinnamic Acid," *Journal of Catalysis*, vol. 204, no. 2, pp. 305–313, 2001.

[98] T. Y. Ma, J. L. Cao, G. S. Shao, X. J. Zhang, and Z. Y. Yuan, "Hierarchically structured squama-like cerium-doped titania: synthesis, photoactivity, and catalytic CO oxidation," *Journal of Physical Chemistry C*, vol. 113, no. 38, pp. 16658–16667, 2009.

[99] L. Zeng, *Study on preparation and mechanism of nano-TiO_2 photocatalyst for strong degradation of VOC*, vol. 16, Huazhong University of Science and Technology, Wuhan, 2015.

[100] L. S. Wu, *Study on preparation and catalytic degradation of formaldehyde of matt catalyst/activated carbon fiber composites*, Sichuan Agricultural University, Yaan, 2016.

[101] M. Khan, J. Li, W. B. Cao, and A. Ullah, "Advancement in the photocatalytic properties of TiO_2 by vanadium and yttrium codoping: Effect of impurity concentration on the photocatalytic activity," *Separation and Purification Technology*, vol. 130, pp. 15–18, 2014.

[102] X. Wang, K. Zhang, X. Guo, G. Shen, and J. Xiang, "Synthesis and characterization of N-doped TiO2loaded onto activated carbon fiber with enhanced visible-light photocatalytic activity," *New Journal of Chemistry*, vol. 38, no. 12, pp. 6139–6146, 2014.

[103] X. Cheng, X. Yu, Z. Xing, and J. Wan, "Enhanced Photocatalytic Activity of Nitrogen Doped TiO2 Anatase Nano-Particle under Simulated Sunlight Irradiation," *Energy Procedia*, vol. 16, pp. 598–605, 2012.

[104] X. H. Li, *Preparation and characterization of doped supported TiO_2 and application of formaldehyde treatment*, Chongqing Technology and Business University, Chongqing, 2009.

[105] W. X. Liu, P. Jiang, W. N. Shao, J. Zhang, and W. B. Cao, "A novel approach for the synthesis of visible-light-active nanocrystalline N-doped TiO_2 photocatalytic hydrosol," *Solid State Sciences*, vol. 33, pp. 45–48, 2014.

[106] J. Wang, D. N. Tafen, Lewis et al., "Origin of photocatalytic activity of nitrogen-doped TiO2 nanobelts," *Journal of the American Chemical Society*, vol. 131, no. 34, pp. 12290–12297, 2009.

[107] R. G. Palgrave, D. J. Payne, and R. G. Egdell, "Nitrogen diffusion in doped TiO_2 (110)single crystals: a combined XPS and SIMS study," *Journal of Materials Chemistry*, vol. 19, no. 44, pp. 8418–8425, 2009.

[108] G. A. Tompsett, G. A. Bowmaker, R. P. Cooney, J. B. Metson, K. A. Rodgers, and J. M. Seakins, "The Raman spectrum of

brookite, TiO_2 (Pbca,Z=8)," *Journal of Raman Spectroscopy*, vol. 26, no. 1, pp. 57–62, 1995.

[109] Z. Zhang, J. Long, X. Xie et al., "Controlling the synergistic effect of oxygen vacancies and N dopants to enhance photocatalytic activity of N-doped TiO_2 by H_2 reduction," *Applied Catalysis A-General*, vol. 425-426, pp. 117–124, 2012.

[110] L. G. Devi and R. Kavitha, "A review on non metal ion doped titania for the photocatalytic degradation of organic pollutants under UV/solar light: Role of photogenerated charge carrier dynamics in enhancing the activity," *Applied Catalysis B Environmental*, vol. 140-141, no. 8, pp. 559–587, 2013.

[111] X. S. Wu, X. H. Tang, and B. Zhang, "Research progress on non-metallic doping mechanism of TiO_2 photocatalyst," *Technology & Development of Chemical Industry*, vol. 38, no. 5, pp. 33–35, 2009.

[112] J. Auvinen and L. Wirtanen, "The influence of photocatalytic interior paints on indoor air quality," *Atmospheric Environment*, vol. 42, no. 18, pp. 4101–4112, 2008.

[113] W. Y. Huang, L. J. Shao, Y. Jiang, X. J. Zhang, and H. M. Wang, "Preparation of photocatalyst/activated carbon/electro spun nanofiber composite membrane and its formaldehyde removal performance," *Journal of Public Health and Preventive Medicine*, vol. 29, no. 5, pp. 3–5, 2018.

[114] L. S. Wu, *Study on preparation and catalytic degradation of formaldehyde of matt catalyst/activated carbon fiber composites*, Sichuan Agricultural University, Yaan, 2016.

[115] H. F. Sun, G. D. Zhang, and G. Y. Zheng, "Photocatalytic degradation of formaldehyde by TiO_2 supported on activated carbon," *Journal of Anhui University of Technology*, vol. 24, no. 1, p. 4, 2007.

[116] C. Yu-Juan, H. Zhong-Hua, W. Xiao-Jing, Z. Guo-Hua, L. Ya-Fei, and L. Wei, "Influence of Pore Size and Surface Area of Activated Carbon on the Performance of TiO2/AC Photocatalyst," *Acta Physico-Chimica Sinica*, vol. 24, no. 9, pp. 1589–1596, 2008.

[117] X. C. Lu, J. C. Jiang, K. Sun, and D. D. Cui, "Effect of specific surface area and pore size of activated carbon on photocatalytic activity of TiO_2/ AC," *Chemistry and Industry of Forest Products*, vol. 30, no. 6, pp. 29–34, 2010.

[118] Q. Q. Luo, K. J. He, and K. J. Wang, "Preparation and photocatalytic performance of nano-sized TiO_2 supported by activated carbon," *Journal of University of Science and Technology Liaoning*, vol. 37, no. 5, p. 2, 2014.

[119] S. Wang, *Preparation and Photocatalytic Performance of Activated Carbon Supported Titanium Dioxide Catalyst*, Nanjing University of Aeronautics and Astronautics, Nanjing, 2012.

[120] B. Xing, C. L. Shi, C. X. Zhang et al., "Preparation of TiO_2/activated carbon composites for photocatalytic degradation of RhB under UV light irradiation," *Journal of Nanomaterials*, vol. 2016, 10 pages, 2016.

[121] X. J. Ma and D. N. Li, "Degradation of formaldehyde by nano TiO_2 supported by wood activated carbon fiber," *Journal of Tianjin University of Science and Technology*, vol. 29, no. 2, pp. 25–29, 2014.

[122] X. H. Li, X. X. Zheng, Z. Y. Yin, K. S. Hou, and X. Rui, "Study on photocatalytic degradation of formaldehyde wastewater by nano TiO_2 supported on activated carbon," *Chemical Research and Application*, vol. 21, no. 4, pp. 2-3, 2009.

[123] X. D. Hu and H. Deng, "Preparation and photocatalytic activity of TiO_2 supported by activated carbon," *Carbon*, vol. 31, pp. 2-3, 2012.

Hindawi
Adsorption Science & Technology
Volume 2021, Article ID 3131309, 8 pages
https://doi.org/10.1155/2021/3131309

Research Article

Effect of Ce Addition on Adsorption and Oxidation of NO over MnO_x/Al_2O_3

Chunhui Mou,[1] **Hui Li**,[2] **Ning Dong**,[2] **Shien Hui**,[2] **and Denghui Wang**[2]

[1]*School of Electronic and Information Engineering, Xi'an Jiaotong University, Xi'an 710049, China*
[2]*School of Energy and Power Engineering, Xi'an Jiaotong University, Xi'an 710049, China*

Correspondence should be addressed to Denghui Wang; denghuiwang@163.com

Received 31 May 2021; Revised 21 August 2021; Accepted 26 August 2021; Published 8 September 2021

Academic Editor: Stefano Salvestrini

The MnO_x/Al_2O_3 catalysts with different Ce content doping were prepared by an ultrasonic impregnation method, and the catalytic activity for NO oxidation removal was tested in a fixed-bed quartz tube furnace. Simultaneously, the catalysts were characterized by X-ray diffraction (XRD), X-ray photoelectron spectroscopy (XPS), full-automatic physical-chemical adsorption instrument, and field emission scanning electron microscope (FESEM) to analyze the effect of Ce addition on the adsorption capacity and catalytic activity. Experimental results validated that the activity of the MnO_x/Al_2O_3 catalyst was greatly promoted with Ce addition. According to the characterization results, it could be concluded that Ce doping led to significant changes in the crystalline phase on the catalyst surface, which increased the relative content of surface lattice oxygen and promoted the catalytic oxidation of NO. By observing the physical properties of the surface and analyzing the surface elements of the catalyst, it could be inferred that a manganese-cerium solid solution was formed on the surface of $Mn_{0.4}Ce_{0.05}/Al$. Moreover, Ce addition increased the catalyst pore size, which enhanced the adsorption and contact of NO and O_2 with the active sites on the catalyst surface, and reduced the resistance of the reactants during internal diffusion. All these variations assigned to $Mn_{0.4}Ce_{0.05}/Al$ were favorable for the catalytic oxidation of NO.

1. Introduction

The combustion of massive fossil fuels brings about the harmful emission of nitrogen oxides (NO_x). The problem has attracted great attention in recent decades, for the close relationship between NO_x and many serious environmental issues, including acid rain, city photochemical smog, and tropospheric ozone depletion [1–4]. To reduce the poisonous NO_x emissions, many techniques have been researched and applied to thermal power plants and diesel engines. Reductive denitration technology has been extensively researched, including selective catalytic reduction (SCR) and selective noncatalytic reduction (SNCR). Due to its high efficiency, SCR has always been regarded as an effective method to remove fixed emission sources such as power plants [5–8]. In the common SCR process, injected NH_3 reduces noxious NO_x to harmless N_2 with the aid of efficient catalysts. The typical reactions are as follows [9, 10].

$$\text{Standard SCR}: 4NH_3 + 4NO + O_2 \longrightarrow 4N_2 + 6H_2O \quad (1)$$

$$\text{Fast SCR}: 2NH_3 + NO + NO_2 \longrightarrow 2N_2 + 3H_2O \quad (2)$$

NH_3-SCR has also exposed many problems in a wide range of industrial applications, such as high investment and operating costs, NH_3 escape, N_2O generation, and catalyst deactivation [11, 12]. The greenhouse effect of N_2O is up to 300 times that of carbon dioxide. The almost inevitable escape of NH_3 is particularly worrying. It not only increases the operation cost but also easily results in serious air preheater blocking. Therefore, how to remove NO_x from coal-burning exhaust gas with low cost, pollution-free, and high

efficiency has become a research focus. Recently, NO catalytic oxidation removal is drawing much attention for its getting rid of NH_3 during NO_x removal [13–15]. Although over 90% of NO_x formed in fuel combustion is insoluble NO, its oxidation product NO_2 is rather soluble. Therefore, with the participation of catalysts, it is feasible to use the remaining O_2 in the flue gas to oxidize NO to NO_2, which is then captured by alkali liquor in a wet flue gas desulfurization plant [11, 16, 17].

Although many noble metal catalysts have shown good performance in NO catalytic oxidation, the high cost limits their wide application in coal-fired power plants [18–20]. Transition metal oxides have been proven with excellent performance compared to noble metal catalysts, with a wide range of sources, low prices, simple preparation processes, and good thermal stability. Therefore, they have received extensive and in-depth research in recent years [21–23]. Wu et al. prepared a series of MnO_x/TiO_2 composite nanoxides by deposition-precipitation method, and the sample with the Mn/Ti ratio of 0.3 showed a superior activity for NO oxidation, reaching 89% at 250°C [24]. Mn-based catalysts impregnated on TiO_2 with different crystalline phases were studied by An et al. for the oxidation of NO to NO_2, and 10% MnO_x/TiO_2 exhibited the highest efficiency 83% at 300°C [22]. The NO oxidation on Cu_2O with molecular oxygen, dissociated oxygen, and lattice oxygen was studied by Sun et al. using periodic density functional theory, and the Eley-Rideal mechanism was favored to explain the catalytic effect of Cu_2O on NO oxidation [25].

Active Al_2O_3 has the characteristics of large adsorption capacity, large specific surface area, good thermal stability, nontoxicity, and noncorrosiveness. Therefore, it is regarded as an excellent catalyst support material and has received extensive attention in the field of catalysis. Wang et al. [26] used a sol-gel method to prepare a series of Ce-based catalysts, selecting Co, Mn, Fe, Cr, and Ni as the doping metal elements. At a reaction temperature of 230°C, the order of NO catalytic activity is Co > Mn > Cr > Ni > Fe.

Although much work has been carried out on NO catalytic oxidation over transition metal oxides, there are some deficiencies along with these studies [21–25]. Firstly, only oxidation efficiency but not removal efficiency was focused on during the experiments. Secondly, the temperature window of the researched catalysts was relatively narrow, not suitable for large-scale practical application. In this investigation, we prepared a series of MnO_x/Al_2O_3 and Ce-doped MnO_x-CeO_y/Al_2O_3 catalysts and investigated the oxidation denitration performance of these catalysts. The effect of Ce doping on the catalyst physicochemical properties was discussed, and microcharacterization analysis was carried out to explore the key points affecting efficiency.

2. Experimental

2.1. Catalyst Preparation. All tested samples in the study were prepared via an ultrasonic impregnation method. Chemicals used here were of analytical grade. Firstly, 0.04 mol (10.04 g) $Mn(NO_3)_2{\cdot}4H_2O$ was dissolved in 20 mL deionized water. Afterwards, with continuous magnetic stirring, 0.1 mol (10.20 g) Al_2O_3 was added into the solution (particle size = 20 nm; specific surface area ≥ 160 m^2/g). Then, the mixture experienced an ultrasonic oscillation lasting for 0.5 h to help to uniformly mix. After standing at room temperature overnight, the suspension was dried in an oven at 105°C for 12 h. The obtained solid product was calcined at 600°C for 5 h and then crushed and sieved to 60-80 mesh. Because the molar ratio of added Mn and Al was 0.4 in the sample, it was denoted as $Mn_{0.4}/Al$.

For samples with different Ce addition, a specific amount (0.005 mol, 0.01 mol, and 0.02 mol, respectively) of $Ce(NO_3)_3{\cdot}6H_2O$ was dissolved in deionized water with $Mn(NO_3)_2{\cdot}4H_2O$ together in the first preparation step. Other preparation procedures were the same as mentioned above. The finally prepared samples were denoted as $Mn_{0.4}Ce_{0.05}/Al$, $Mn_{0.4}Ce_{0.1}/Al$, and $Mn_{0.4}Ce_{0.2}/Al$, respectively.

2.2. Catalytic Activity Test. The catalyst activity test system is shown in Figure 1. The catalytic activity test was carried out in a fixed-bed quartz tube furnace. 0.5 g sample was fixed on the bottom of the quartz glass tube by quartz wool. The total gas flow rate was fixed to 1 L/min (STP), with 600 ppm NO, 8 vol% O_2, and balanced N_2. The exhaust gas after the reaction at a certain temperature was introduced into a 0.5 mol/L sodium hydroxide aqueous solution for absorption, after which the outlet gas composition was examined online by a Fourier transform infrared spectroscopy gas analyzer (Gasmet DX4000, Finland).

The NO removal efficiency was calculated according to the following equation:

$$\text{NO removal efficiency (\%)} = \left(1 - \frac{[NO]_{out} + [NO_2]_{out}}{[NO]_{in}}\right) \times 100. \tag{3}$$

2.3. Catalyst Characterization. N_2 adsorption-desorption measurement was performed on a full-automatic physical-chemical adsorption instrument (Micromeritics ASAP2020, USA) to determine the textural properties of samples. The specific surface area was acquired by the Brunauer-Emmett-Teller (BET) method, while the total pore volume and mean pore diameter were obtained according to the Barrett-Joyner-Halenda (BJH) method. The micromorphologies of samples were monitored by a field emission scanning electron microscope (FESEM, GeminiSEM 500, Germany). An X-ray diffraction (XRD) meter (Xpert pro, Netherlands) was adopted to identify the crystal phases of samples. The scanning angular velocity was 7°/min, and the scanning angle range was 20°-80°. An X-ray photoelectron spectroscopy (XPS, AXIS ULtrabld, UK) was employed to analyze the catalyst surface atomic concentrations, using C1s at 284.8 eV as the calibration.

3. Results and Discussion

3.1. Catalytic Activity. 600 ppm NO, 8 vol% O_2, and balanced N_2 were introduced into the reactor to explore the performance of catalysts with different contents of active component Ce (Figure 2). As the reaction temperature increased

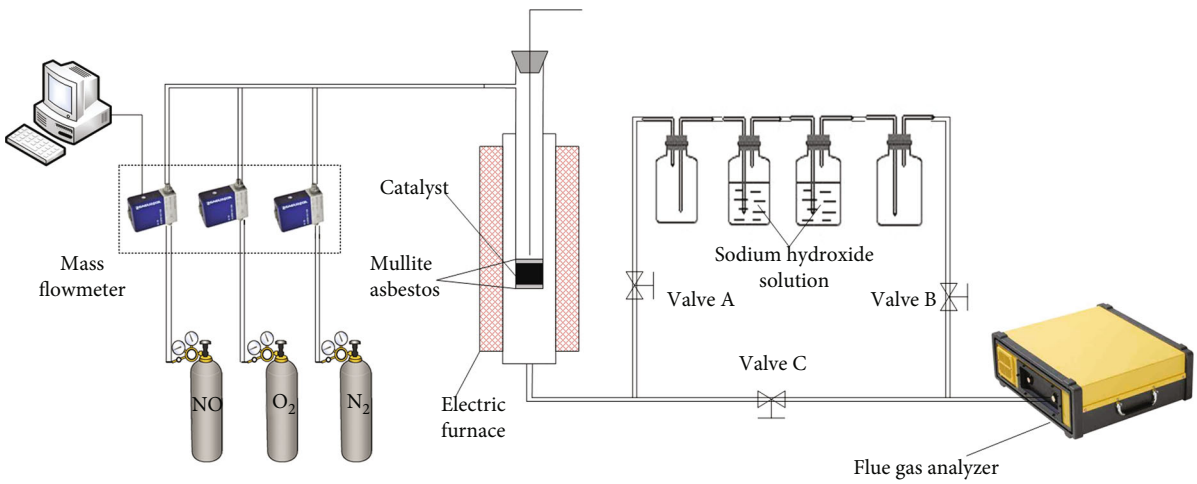

Figure 1: Schematic diagram of the experimental setup.

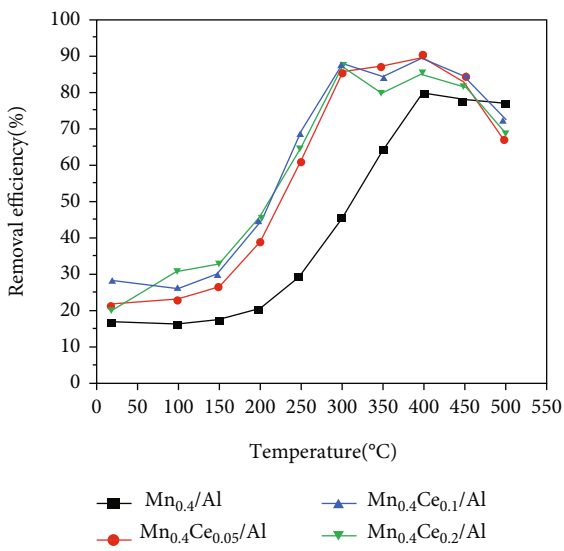

Figure 2: Removal efficiency of catalysts with different Ce contents.

from 20°C to 500°C, the NO removal efficiency was peaked at 400°C for all samples. The oxidation of NO to NO_2 is exothermic, and the reaction is limited by the thermodynamic equilibrium: the temperature rises, and the equilibrium shifts to the left. Therefore, the temperature increased, the NO oxidation rate decreased, and the denitration efficiency decreased. It was apparent that the removal efficiency of the Ce-doped $Mn_{0.4}/Al$ catalyst was higher than that of the Ce-free $Mn_{0.4}/Al$ catalyst, indicating the promotion effect of Ce addition on NO oxidation removal. In addition, the temperature window of $Mn_{0.4}Ce_x/Al$ catalyst is wider than that of $Mn_{0.4}/Al$. The denitration efficiency of $Mn_{0.4}Ce_x/Al$ at 300-450°C can be above 80%.

For the $Mn_{0.4}/Al$ catalyst without Ce addition, the denitration efficiency increased gradually with the reaction temperature in 20-400°C, but it started to decrease slightly as the reaction temperature increased from 400°C to 500°C. The highest efficiency reached 79.5% at 400°C. When the molar ratio of Mn, Ce, and Al was 0.4 : 0.05 : 1, the efficiency reached the highest peak of 89.5%. When the molar ratio of Mn, Ce, and Al was 0.4 : 0.1 : 1, the efficiency peak reached 89.1%, similar to $Mn_{0.4}Ce_{0.05}/Al$. For $Mn_{0.4}Ce_{0.2}/Al$, the highest efficiency was 85.2%, a little lower than $Mn_{0.4}Ce_{0.05}/Al$ and $Mn_{0.4}Ce_{0.1}/Al$. Doping with Ce improves the activity of the Mn/Al catalyst significantly. The temperature window moves to the left, indicating that the low-temperature activity of the catalyst is enhanced. Free Ce has excellent oxygen storage capacity, and a small amount of Ce doping increases the active sites on the catalyst surface, thereby increasing the NO removal rate. But excessive doping may aggravate the accumulation of surface crystals, cover some active centers, or block the pores, resulting in a decrease in the catalytic activity of the catalyst [27, 28]. In the subsequent surface analysis, it was found that after Ce doping, the specific surface area was significantly reduced. The active ingredient is not as much as possible and should be lower than the surface dispersion threshold. Otherwise, Ce agglomerates and stacks on the surface, so $Mn_{0.4}Ce_{0.05}/Al$ with better activity is selected as the main research object in the follow-up.

3.2. XRD. The XRD patterns of $Mn_{0.4}/Al$ and $Mn_{0.4}Ce_{0.05}/Al$ expressing the crystal phases on the catalyst surface are depicted in Figure 3. MnO_x and CeO_x are the main research objects, so the Al_2O_3 carrier is not shown in Figure 3. There were only diffraction peaks corresponding to Mn_2O_3 in the XRD patterns of $Mn_{0.4}/Al$, indicating the well-crystallized Mn_2O_3 for $Mn_{0.4}/Al$ catalysts. As for $Mn_{0.4}Ce_{0.05}/Al$, the diffraction peaks at 28.8°, 41.2°, and 67.2° were attributed to MnO_2, while the diffraction peaks at 28.9°, 36.5°, and 57.8° were ascribed to Mn_3O_4.

In the XRD patterns of $Mn_{0.4}Ce_{0.05}/Al$, the diffraction peaks of MnO_2 and Mn_3O_4 were very weak, and no diffraction peaks of Mn_2O_3 existed, which revealed that the addition of Ce had a great influence on the crystal structure of $Mn_{0.4}/Al$ catalyst. It is worth noting that we also did not detect the crystalline phase of Ce in the XRD pattern, which indicated that Ce was evenly dispersed on the surface of the catalyst, or Ce enters the lattice of manganese. We speculate

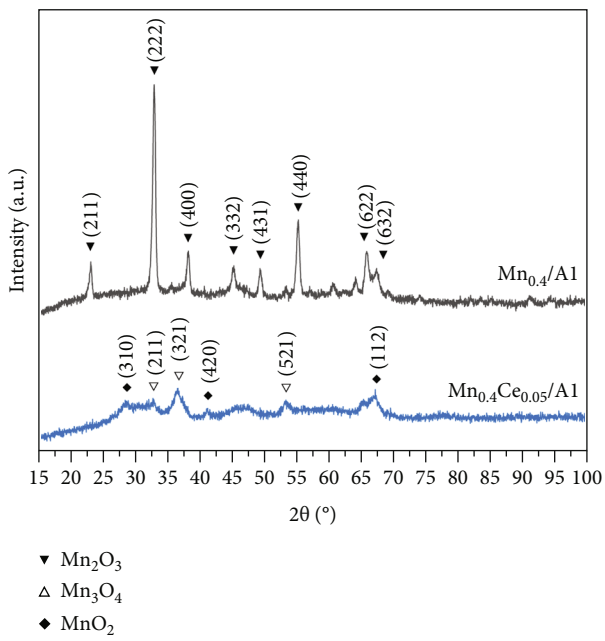

Figure 3: XRD patterns of $Mn_{0.4}$/Al and $Mn_{0.4}Ce_{0.05}$/Al.

that Ce atoms may enter the lattice of Mn_2O_3, resulting in the disappearance of a large amount of Mn_2O_3 crystal structure on the catalyst surface and resulting in the increase of the crystal structure of MnO_2 and Mn_3O_4 on the catalyst surface.

After adding active component Ce to $Mn_{0.4}$/Al catalyst, manganese and cerium interacted in a solid solution manner, and manganese ions entered the cerium oxide lattice to increase the oxygen storage capacity of the cerium oxide and the oxygen migration activity of the surface oxide [29]. This interaction was related to the electron transfer between manganese and cerium and the gain and loss of oxygen, and it also influenced the crystal structure of the catalyst and the valence state of manganese and cerium compounds. Therefore, related characterization analysis was carried out.

3.3. XPS. The XPS spectra for Mn 2p of $Mn_{0.4}$/Al and $Mn_{0.4}Ce_{0.05}$/Al are separately drawn in Figure 4(a) and Figure 4(b). Mn2p peaks for Mn oxides have many multiplet-split components, and the binding energy of Mn^{4+} is greater than Mn^{3+} [30]. In Figure 4(a), the binding energy peaks of 641.0 eV and 652.5 eV represent Mn^{3+}; the binding energy peaks at 642.8 eV and 653.4 eV represent Mn^{4+}. The relative size of the energy spectrum peak area represents the relative content of different manganese oxides on the catalyst surface. The $Mn^{4+}/(Mn^{3+} + Mn^{4+})$ ratio and the $Mn^{3+}/(Mn^{3+} + Mn^{4+})$ ratio were 46.1% and 53.9%, respectively.

On $Mn_{0.4}Ce_{0.05}$/Al, the binding energy peaks of 641.3 eV and 652.8 eV represent Mn^{3+}; the binding energy peaks at 642.8 eV and 654.2 eV represent Mn^{4+} in Figure 4(b). Compared with Mn0.4Ce0.05/Al, the energy level was shifted upward. The $Mn^{4+}/(Mn^{3+} + Mn^{4+})$ ratio and the $Mn^{3+}/(Mn^{3+} + Mn^{4+})$ ratio were 31.0% and 69.0%, respectively. The

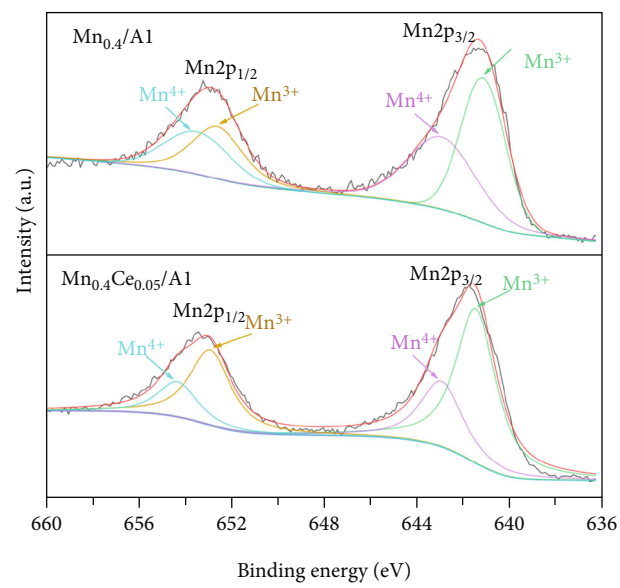

Figure 4: XPS spectra for Mn 2p of (a) $Mn_{0.4}$/Al and (b) $Mn_{0.4}Ce_{0.05}$/Al.

results indicated that partial Mn^{4+} converted to Mn^{3+} as a result of the addition of cerium. The increase of Mn^{3+} and the decrease of Mn^{4+} favored the catalyst oxidation activity, which was consistent with the results of Atribak et al. [31]. They also confirmed that the activity of Mn^{4+} for NO oxidation was lower than that of Mn^{3+}.

Figure 5 shows the XPS spectra for O 1s of $Mn_{0.4}$/Al (Figure 5(a)) and $Mn_{0.4}Ce_{0.05}$/Al (Figure 5(b)). There were two kinds of oxygen in catalysts, i.e., surface absorbed oxygen (denoted as O_α) and lattice oxygen (denoted as O_β). In

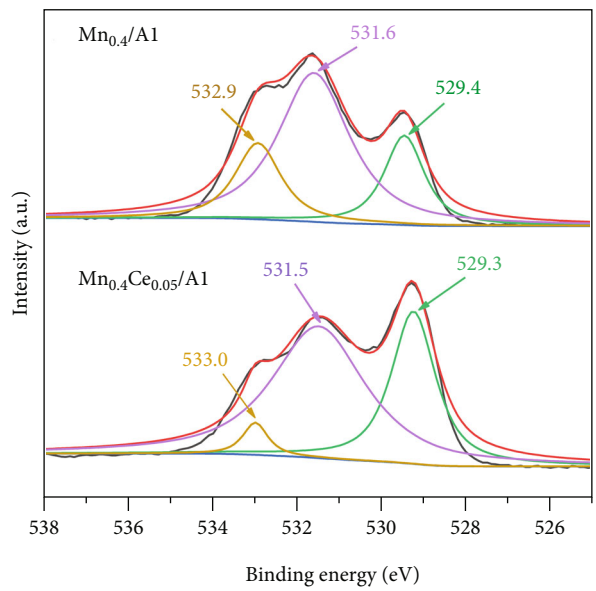

Figure 5: XPS spectra for O 1s of (a) the $Mn_{0.4}$/Al catalyst and (b) the $Mn_{0.4}Ce_{0.05}$/Al catalyst.

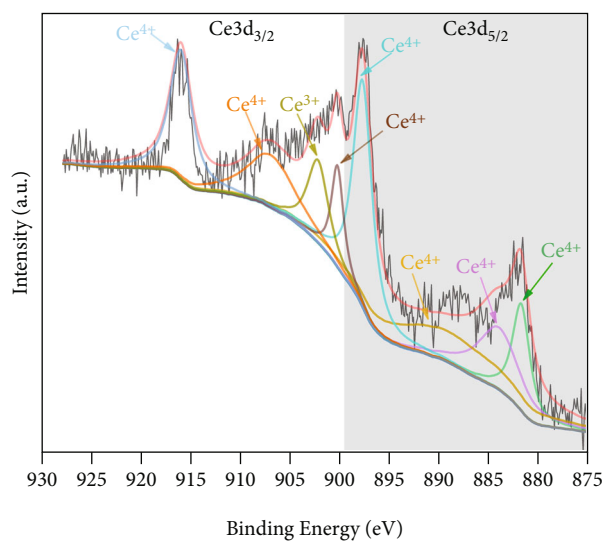

Figure 6: XPS spectra for Ce 3d of the $Mn_{0.4}Ce_{0.05}$/Al catalyst.

Table 1: Results of the XPS results of $Mn_{0.4}$/Al and $Mn_{0.4}Ce_{0.05}$/Al.

Sample	$Mn^{4+}/(Mn^{3+}+Mn^{4+})$	$Mn^{3+}/(Mn^{3+}+Mn^{4+})$	O_α/O	O_β/O
$Mn_{0.4}$/Al	46.1%	53.9%	79.6%	20.4%
$Mn_{0.4}Ce_{0.05}$/Al	31.0%	69.0%	65.7%	34.3%

Figure 5(a), peaks at 532.9 and 531.6 eV were attributed to O_α, while the peak at 529.4 eV corresponded to O_β. And in Figure 5(b), peaks at 533.0 and 531.5 eV were attributed to O_α, while the peak at 529.3 eV corresponded to O_β. Although the binding energy for each peak showed few differences in Figure 5(a) and Figure 5(b), the intensity varied greatly, especially the relative intensity of O_α and O_β. The proportion of O_β to $(O_\alpha + O_\beta)$ in Figure 5(a) was as low as 20.4%, whereas the proportion in Figure 5(b) increased to 34.3%.

Table 2: Physical properties of catalysts.

Sample	BET surface area (m^2/g)	BJH pore volume (cm^3/g)	Average pore diameter (nm)
$Mn_{0.4}$/Al	86.61	0.143	23.17
$Mn_{0.4}Ce_{0.05}$/Al	69.44	0.139	28.69

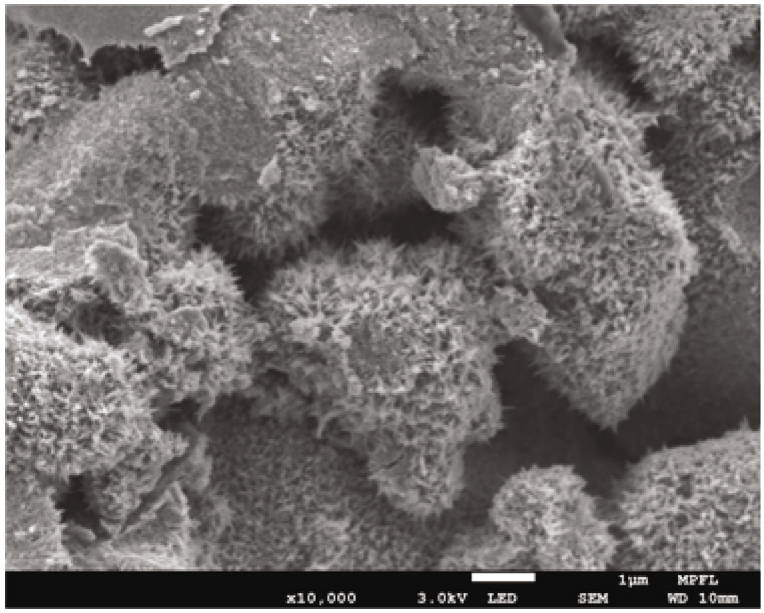

(a)

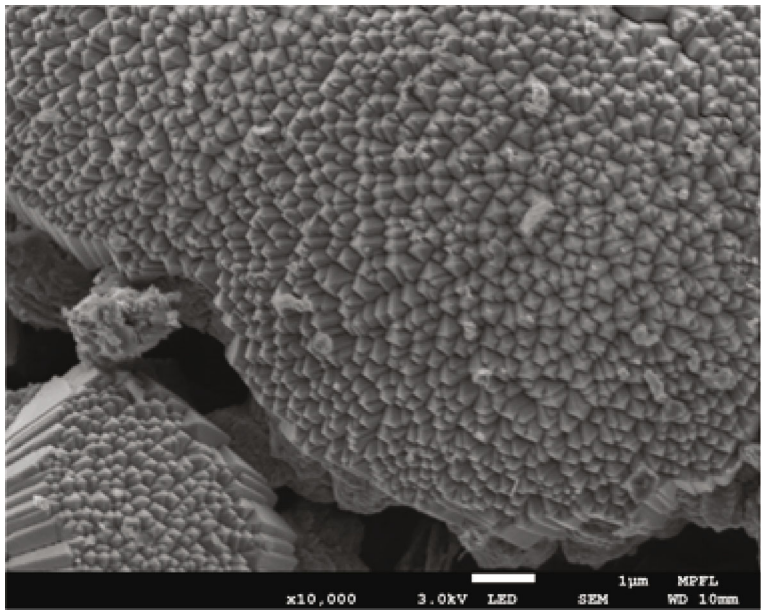

(b)

Figure 7: FESEM images of (a) $Mn_{0.4}$/Al and (b) $Mn_{0.4}Ce_{0.05}$/Al.

Lattice oxygen played an important role in NO oxidation. After adsorption on the catalyst surface, NO was first oxidized by the active lattice oxygen to form nitrite or nitrate on the surface of the catalyst [32]. The higher proportion of O_β signified the more lattice oxygen in catalysts, so $Mn_{0.4}Ce_{0.05}$/Al exhibited better catalytic oxidation activity than $Mn_{0.4}$/Al. Xiang et al. [33] built a model of manganese oxide loaded on alumina and analyzed the adsorption of NO and O_2 on the Mn/Al surface by density functional theory. Calculations have found that O_2 is not easy to stably adsorb on the Mn/Al surface, so the surface lattice oxygen O_β is more likely to participate in the oxidation of NO by the MvK mechanism. This was consistent with our experimental conclusions that the $Mn_{0.4}Ce_{0.05}$/Al catalyst with higher lattice oxygen content had a stronger ability to oxidize NO.

Figure 6 shows the XPS spectra for Ce 3d of $Mn_{0.4}Ce_{0.05}$/Al. The Ce 3d spectrum consists of two series of spin-orbit lines $Ce3d_{3/2}$ and $Ce3d_{5/2}$ [34]. There were eight distinct characteristic peaks, of which the peaks at 881.8 eV, 889.2 eV, 897.7 eV, 902.3 eV, 907.0 eV, and 916.0 eV correspond to Ce^{4+} [26, 35], and the peaks at 902.2 eV and 884.0 eV correspond to Ce^{3+} [36, 37]. It indicated that Ce in $Mn_{0.4}Ce_{0.05}$/Al had two forms of Ce^{4+} and Ce^{3+} after calcination at high temperature. The Ce^{4+}/(Ce^{3+}

$+ Ce^{4+}$) ratio and the $Ce^{3+}/(Ce^{3+} + Ce^{4+})$ ratio were 20.56% and 79.44%, respectively.

Ce had strong oxygen storage capacity and stores and releases oxygen through the transformation of Ce^{3+} and Ce^{4+}, which was consistent with the higher lattice oxygen content on the surface of $Mn_{0.4}Ce_{0.05}/Al$. It can be seen from Figure 1 that Ce doping improved the low-temperature activity of the catalyst, which was consistent with the study of other scholars [38, 39]. In addition, the doping of Ce element led to a reduction in the amount of O atoms combined with Mn, which in turn converted Mn^{4+} to Mn^{3+} with better activity.

The results of the XPS characteristics of $Mn_{0.4}/Al$ and $Mn_{0.4}Ce_{0.05}/Al$ are listed in Table 1. According to the analysis above, the increase of Mn^{3+} and lattice oxygen was important for the effective improvement of catalyst activity.

The physical properties of $Mn_{0.4}/Al$ and $Mn_{0.4}Ce_{0.05}/Al$ are listed in Table 2, mainly including the BET surface area, the BJH pore volume, and the BJH average pore diameter. From Table 2, it could be found that the surface area and the pore volume of the $Mn_{0.4}Ce_{0.05}/Al$ catalyst were lower than those of the $Mn_{0.4}/Al$ catalyst. On the contrary, the pore diameter of the $Mn_{0.4}Ce_{0.05}/Al$ catalyst was higher.

According to the XRD analysis results, cerium ions entered the manganese oxide lattice, resulting in an increase in the weight per unit volume of the pore structure and resulting in the decrease in the specific surface area and pore volume of the catalyst [40]. And it could be found in Table 1 that the O_α of $Mn_{0.4}Ce_{0.05}/Al$ catalyst was less than that of $Mn_{0.4}/Al$. The decrease of O_α was probably because of the decrease of the catalyst pore volume. Larger pore size will enhance the contact of NO and O_2 with the active sites on the catalyst surface and reduce the resistance of the reactants during internal diffusion, so $Mn_{0.4}Ce_{0.05}/Al$ exhibits stronger NO removal performance.

3.4. FESEM. The FESEM images with magnification times (×10000) of $Mn_{0.4}/Al$ and $Mn_{0.4}Ce_{0.05}/Al$ are shown in Figure 7. As shown in Figure 7(a), the $Mn_{0.4}/Al$ surface was evenly distributed with fine particles. According to the above XRD analysis results, they were likely to be Mn_2O_3 particles. As shown in Figure 7(b), there were many needle-like substances on the $Mn_{0.4}Ce_{0.05}/Al$ surface. The surface of $Mn_{0.4}Ce_{0.05}/Al$ was rougher, which was conducive to generating more active sites and also conducive to the adsorption of reactants, which strengthens the catalytic oxidation of NO on the surface.

4. Conclusions

The NO oxidation removal activity of $Mn_{0.4}/Al$ catalysts with different Ce contents ($Mn_{0.4}/Al$, $Mn_{0.4}Ce_{0.05}/Al$, $Mn_{0.4}Ce_{0.1}/Al$, and $Mn_{0.4}Ce_{0.2}/Al$) was studied experimentally. The results showed that the activity of $Mn_{0.4}/Al$ catalysts was effectively promoted with Ce addition, and the $Mn_{0.4}Ce_{0.05}/Al$ performed the best.

Simultaneously, the physical-chemical properties and microstructures of $Mn_{0.4}/Al$ and $Mn_{0.4}Ce_{0.05}/Al$ were compared and analyzed by various characterization methods, which was helpful to reveal the mechanism of catalytic oxidation of NO by Mn-based catalysts and the effect of Ce addition. The characterization results showed that (1) the entry of cerium ions into the manganese oxide lattice led to the change of crystal structure of the catalyst surface and the decrease of specific surface area and pore volume; (2) the decrease of Mn^{4+} and the increase of Mn^{3+} on the catalyst surface were beneficial to the NO oxidation; (3) Ce doping increased the lattice oxygen content on the surface of the $Mn_{0.4}Ce_{0.05}/Al$, which was favorable for NO oxidation.

Data Availability

All data, models, and code generated or used during the study appear in the submitted article.

Conflicts of Interest

The authors declared no potential conflicts of interest with respect to the research, authorship, and/or publication of this article.

Acknowledgments

The present work was supported by the National Natural Science Foundation of China (51906193).

References

[1] C. Zhou, Y. Wang, Q. Jin, Q. Chen, and Y. Zhou, "Mechanism analysis on the pulverized coal combustion flame stability and NO_x emission in a swirl burner with deep air staging," *Journal of the Energy Institute*, vol. 92, no. 2, pp. 298–310, 2019.

[2] X. Jin and Y. Zhou, "Numerical analysis on microscopic characteristics of pulverized coal moderate and intense low-oxygen dilution combustion," *Energy & Fuels*, vol. 29, no. 5, pp. 3456–3466, 2015.

[3] S. Li, Y. Ge, and X. Wei, "Modeling NO and SO_2 oxidation by H_2O_2 in coal-fired flue gas," *Journal of Environmental Engineering*, vol. 144, no. 11, p. 04018113, 2018.

[4] S. Li, Y. Ge, and X. Wei, "Experiment on NO_x reduction by advanced reburning in cement precalciner," *Fuel*, vol. 224, pp. 235–240, 2018.

[5] G. Madia, M. Koebel, M. Elsener, and A. Wokaun, "The effect of an oxidation precatalyst on the NO_x reduction by ammonia SCR," *Industrial & Engineering Chemistry Research*, vol. 41, pp. 3512–3517, 2002.

[6] G. Madia, M. Elsener, M. Koebel, F. Raimondi, and A. Wokaun, "Thermal stability of vanadia tungsta-titania catalysts in the SCR process," *Applied Catalysis B: Environmental*, vol. 39, pp. 181–190, 2002.

[7] P. Glarborg, J. A. Miller, B. Ruscic, and S. J. Klippenstein, "Modeling nitrogen chemistry in combustion," *Progress in Energy and Combustion Science*, vol. 67, pp. 31–68, 2018.

[8] Y. Song, H. Hashemi, J. M. Christensen, C. Zou, P. Marshall, and P. Glarborg, "Ammonia oxidation at high pressure and intermediate temperatures," *Fuel*, vol. 181, pp. 358–365, 2016.

[9] M. H. Kim and S. W. Park, "Selective reduction of NO by NH_3 over Fe-zeolite-promoted V_2O_5-WO_3/TiO_2-based catalysts: great suppression of N_2O formation and origin of NO removal

activity loss," *Catalysis Communications*, vol. 86, pp. 82–85, 2016.

[10] M. H. Kim and H. S. Lee, "Effect of Fe-zeolite on formation of N_2O in selective reduction of NO by NH_3 over V_2O_5–WO_3/TiO_2 catalyst," *Research on Chemical Intermediates*, vol. 42, no. 1, pp. 171–184, 2015.

[11] W. Wang, R. Guo, W. Pan, and G. Hu, "Low temperature catalytic oxidation of NO over different-shaped CeO_2," *Journal of Rare Earths*, vol. 36, pp. 588–593, 2018.

[12] Z. Zhang, J. D. Atkinson, B. Jiang, M. J. Rood, and Z. Yan, "Nitric oxide oxidation catalyzed by microporous activated carbon fiber cloth: an updated reaction mechanism," *Applied Catalysis B: Environmental*, vol. 148-149, pp. 573–581, 2014.

[13] H. Wang, H. Chen, Y. Wang, and Y.-K. Lyu, "Performance and mechanism comparison of manganese oxides at different valence states for catalytic oxidation of NO," *Chemical Engineering Journal*, vol. 361, pp. 1161–1172, 2019.

[14] S. Cui, R. Hao, and D. Fu, "Integrated method of non-thermal plasma combined with catalytical oxidation for simultaneous removal of SO_2 and NO," *Fuel*, vol. 246, pp. 365–374, 2019.

[15] H. Yuan, J. Chen, H. Wang, and P. Hu, "Activity trend for low-concentration NO oxidation at room temperature on rutile-type metal oxides," *ACS Catalysis*, vol. 8, pp. 10864–10870, 2018.

[16] H. Yuan, J. Chen, Y. Guo, H. Wang, and P. Hu, "Insight into the superior catalytic activity of MnO_2 for low-content NO oxidation at room temperature," *The Journal of Physical Chemistry C*, vol. 122, pp. 25365–25373, 2018.

[17] X. Yao, J. Liu, and W. Wang, "Influence of B-site transition metal on NO oxidation over $LaBO_3$ (B=Mn, Fe and Co) perovskite catalysts," *AIP Advances*, vol. 8, p. 115222, 2018.

[18] S. Thampy, Y. Zheng, S. Dillon et al., "Superior catalytic performance of Mn-mullite over Mn-perovskite for NO oxidation," *Catalysis Today*, vol. 310, pp. 195–201, 2018.

[19] Y. Song and L. C. Grabow, "Activity trends for catalytic CO and NO co-oxidation at low temperature diesel emission conditions," *Industrial & Engineering Chemistry Research*, vol. 57, pp. 12715–12725, 2018.

[20] C. Shi, H. Chang, C. Wang et al., "Improved activity and H_2O resistance of Cu-modified MnO2Catalysts for NO oxidation," *Industrial & Engineering Chemistry Research*, vol. 57, no. 3, pp. 920–926, 2018.

[21] H. Chen, Y. Wang, and Y.-K. Lyu, "High catalytic activity of Mn-based catalyst in NO oxidation at low temperature and over a wide temperature span," *Molecular Catalysis*, vol. 454, pp. 21–29, 2018.

[22] Z. An, Y. Zhuo, C. Xu, and C. Chen, "Influence of the TiO_2 crystalline phase of MnO_x/TiO_2 catalysts for NO oxidation," *Chinese Journal of Catalysis*, vol. 35, no. 1, pp. 120–126, 2014.

[23] P. S. Metkar, V. Balakotaiah, and M. P. Harold, "Experimental and kinetic modeling study of NO oxidation: comparison of Fe and Cu-zeolite catalysts," *Catalysis Today*, vol. 184, pp. 115–128, 2012.

[24] Z. Wu, N. Tang, L. Xiao, Y. Liu, and H. Wang, "$MnO(_x)$/-$TiO(_2)$ composite nanoxides synthesized by deposition-precipitation method as a superior catalyst for NO oxidation," *Journal of Colloid and Interface Science*, vol. 352, no. 1, pp. 143–148, 2010.

[25] B.-Z. Sun, X.-L. Xu, W.-K. Chen, and L.-H. Dong, "Theoretical insights into the reaction mechanisms of NO oxidation catalyzed by Cu_2O(1 1 1)," *Applied Surface Science*, vol. 316, pp. 416–423, 2014.

[26] Z. Wang, F. Lin, S. Jiang et al., "Ceria substrate-oxide composites as catalyst for highly efficient catalytic oxidation of NO by O_2," *Fuel*, vol. 166, pp. 352–360, 2016.

[27] B.-L. Wang, J. Zhang, and H.-X. Zhong, "Effect of Ce doping content on catalytic performance of supported Co/ZrO_2 catalysts for combustion of methane," *Modern Chemical Industry*, vol. 40, no. 12, pp. 151–155, 2020.

[28] X.-H. Li, S.-L. Zhang, Y. Jia, X. Liu, and Q. Zhong, "Selective catalytic oxidation of NO with O_2 over Ce- doped MnO $_{x}$ /TiO_2 catalysts," *Journal of Natural Gas Chemistry*, vol. 21, no. 1, pp. 17–24, 2012.

[29] J. Zhou, L. Yu, M. Sun et al., "MnO_2 nanosheet-assisted hydrothermal synthesis of β-MnO_2 branchy structures," *Materials Letters*, vol. 79, pp. 288–291, 2012.

[30] L. Qiu, J.-J. Meng, and D.-D. Pang, "Reaction and characterization of Co and Ce doped Mn/TiO_2 catalysts for low-temperature SCR of NO with NH_3," *Catalysis Letters*, vol. 145, no. 7, pp. 1500–1509, 2015.

[31] I. Atribak, A. Bueno-López, A. García-García, P. Navarro, D. Frías, and M. Montes, "Catalytic activity for soot combustion of birnessite and cryptomelane," *Applied Catalysis B: Environmental*, vol. 93, no. 3-4, pp. 267–273, 2010.

[32] Z. Wu, R. Jin, Y. Liu, and H. Wang, "Ceria modified MnO_x/-TiO_2 as a superior catalyst for NO reduction with NH_3 at low-temperature," *Catalysis Communications*, vol. 9, no. 13, pp. 2217–2220, 2008.

[33] J. Xiang, L.-L. Wang, F. Cao et al., "Adsorption properties of NO and NH_3 over MnO_x based catalyst supported on γ-Al_2O_3," *Chemical Engineering Journal*, vol. 302, pp. 570–576, 2016.

[34] M. Lykaki, E. Pachatouridou, S. A. C. Carabineiro et al., "Ceria nanoparticles shape effects on the structural defects and surface chemistry: implications in CO oxidation by Cu/CeO_2 catalysts," *Applied Catalysis B: Environmental*, vol. 230, pp. 18–28, 2018.

[35] Y. Cui and W.-L. Dai, "Support morphology and crystal plane effect of Cu/CeO2nanomaterial on the physicochemical and catalytic properties for carbonate hydrogenation," *Catalysis Science & Technology*, vol. 6, no. 21, pp. 7752–7762, 2016.

[36] X.-L. Guo and R.-X. Zhou, "A new insight into the morphology effect of ceria on CuO/CeO_2 catalysts for CO selective oxidation in hydrogen-rich gas," *Catalysis Science & Technology*, vol. 6, pp. 3862–3871, 2016.

[37] C. Wang, Q.-P. Cheng, X.-L. Wang et al., "Enhanced catalytic performance for CO preferential oxidation over CuO catalysts supported on highly defective CeO_2 nanocrystals," *Applied Surface Science*, vol. 422, no. 15, pp. 932–943, 2017.

[38] L. Jiang, Q. Liu, G. Ran et al., "V_2O_5-modified Mn-Ce/AC catalyst with high SO_2 tolerance for low-temperature NH_3-SCR of NO," *Chemical Engineering Journal*, vol. 370, pp. 810–821, 2019.

[39] K. Li, X. Tang, H. Yi, P. Ning, D. Kang, and C. Wang, "Low-temperature catalytic oxidation of NO over Mn-Co-Ce-Ox catalyst," *Chemical Engineering Journal*, vol. 192, pp. 99–104, 2012.

[40] H.-X. Jiang, J. Zhao, and D.-Y. Jiang, "Hollow MnO_x-CeO_2 nanospheres prepared by a green route: a novel low-temperature NH3-SCR catalyst," *Catalysis Letters*, vol. 114, no. 2, article S0169433217316616, pp. 325–332, 2014.